Studies on a plastic scintillator detector for activity measurement of tritiated water

Zur Erlangung des akademischen Grades eines

DOKTOR DER NATURWISSENSCHAFTEN

von der Fakultät für Physik der

Karlsruher Institut für Technologie (KIT)

genehmigte

DISSERTATION

Von

Zoltán Köllő

aus Budapest

Tag der mündlichen Prüfung: 17.07.2015

Referent: Prof. Dr. Guido Drexlin

Korreferent: Prof. Dr. Bernhard Holzapfel

DOI: 10.5445/IR/1000049424

In memory of my mother.

Contents

List of Tables

List of Figures

1 Introduction

Fusion of light elements is a promising energy source for the future, as a fusion power plant virtually would not emit greenhouse gases, and could fulfill the energy need of humanity for millions of years [1]. However, the continuous electrical energy production by means of fusion is still in the experimental phase. The International Thermonuclear Experimental Reactor (ITER) is going to be the biggest fusion reactor in the world. It is under construction in Cadarache, France, with the aim of proving the concept of sustained fusion.

Stars in the Universe burn hydrogen by means of the so-called proton-proton cycle [2], in which ^{4}He is produced. This process requires a temperature above 10^7 K, and a pressure of approximately 10^{11} bar. The latter pressure value is not technically realistic, therefore another reaction is necessary for fusion on Earth. The fusion reactions of deuterium (D) and/or tritium (T) (listed in Table 1.1) require much less pressure (however much higher temperature, on the order of several hundred million degrees), therefore these are the most relevant for fusion energy production [1]. Among these, the D-T reaction has the highest energy gain, therefore it is planned to use a 50:50 D-T mixture as fuel in future fusion power plants. Such a power plant would have a tokamak-type reactor (see Fig. 1.1), which is a torus-shaped vessel with a magnetic field inside. The magnetic field confines the hot ionized gas (plasma), and keeps it away from the vessel walls by means of the Lorenz force. This magnetic field has to be so strong, that it only can be achieved with superconducting magnets, which necessitates a cryogenic vessel around the electromagnet system.

The gases in the torus are continuously pumped away through the divertor part of the reactor vessel. The fusion machine requires a gas handling system that fuels the reactor and treats the exhaust gases because most of the injected fuel is pumped out without fusion reaction, therefore it has to be cleaned and re-injected. Since tritium is radioactive (see Section 2.1), this fuel cycle has to be a closed system. Closed tritium handling systems have been in operation for many years. One of them is at the Tritium Laboratory Karlsruhe (TLK), which is also a model for the fuel cycle of fusion reactors

Table 1.1: **Fusion reactions of hydrogen isotopes.** Data is obtained from Ref. [3].

Reaction	Products	Energy gain (MeV)
D + T →	^{4}He + n	17.6
T + T →	^{4}He + 2n	11.3
D + D →	T + H	3.98
D + D →	^{3}He + n	3.25

[4]. The closed tritium cycle of TLK is represented in Fig. 1.2. The "experiments" part in the figure is the reactor vessel in a fusion reactor.

In the closed tritium loop, among other impurities, tritiated water is produced. The tritium in this water has to be extracted by a dedicated facility, such as the TRENTA facility in TLK [22] (Fig. 1.3). TRENTA[1] uses the Liquid Phase Catalytic Exchange (LPCE) process (for details see Ref. [22]) to enrich tritium in water. The resulting tritiated water later will be electrolyzed, and tritium will be extracted by means of a cryogenic distillation column, under development in TLK (see also the right side of Fig. 1.2). For process monitoring purposes it is needed to know how much tritium is in the processed water, which is done mostly by offline methods, also involving handling of tritiated water by the operating personnel. Since tritiated water is highly toxic, it would be advantageous to have an online and inline monitor, which eliminates the need of sample taking and also speeds up the measurement process.

In this thesis the investigation of a plastic scintillator-based tritium detector is presented. The main goal was to test the concept for higher concentrations as before (up to several GBq/ℓ concentration) and investigate possible enhancements of the scintillator geometry, besides understanding the detection process. For these purposes an experimental setup consisting of standard industrial parts was designed, constructed and calibrated for HTO. Several sample chamber geometries were tested (e.g. more scintillator plates above each other, varying sample volume, etc.), and the configurations were compared in terms of sensitivity and detected pulse height spectrum. To understand the detection process in detail, a simulation was coded and compared with the experimentally obtained results.

The thesis is built up as follows: First, a brief chapter introduces tritiated water, concerning properties and processing in tritium handling facilities. The next chapter presents the scintillation counting method in detail, based on the available literature. This is followed by the discussion of the previous studies in the topic of tritiated water activity measurement, then the goals of this study are defined. Chapter 4 deals with the design considerations and the technical details of the experimental setup. The next chapter presents the optimization of the setup for measurement, then the calibration of for tritium is presented. The chapter also includes the analysis of the pulse height spectrum of tritiated water, and results of the measurements with varying sample amount and scintillator surface, all followed by discussion. Chapter 6 first presents the technical improvements done on the setup, then the results of additional measurement series and their discussion follow. In the last chapter, the simulation of the detection process is presented, together with discussion of the results. The experimentally obtained spectrum is compared with the simulation and the implications of the differences is discussed. This chapter is followed by a summary of the thesis, together with the conclusions drawn from the results.

[1] TRitium ENTzugsAnlage, meaning tritium extraction system

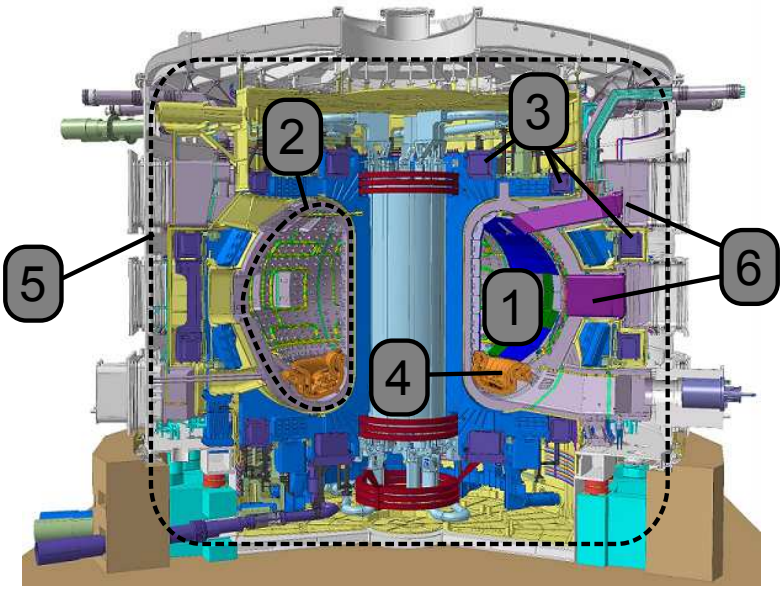

Figure 1.1: **The tokamak reactor of ITER.** 1: Reactor vessel, 2: Toroidal field coils, 3: Poloidal field coils, 4: Divertor, 5: Cryogenic vessel, 6: Vacuum vessel ports (for e.g. fueling, plasma investigation, etc.). The original picture is from Ref. [1], which have been annotated for this figure.

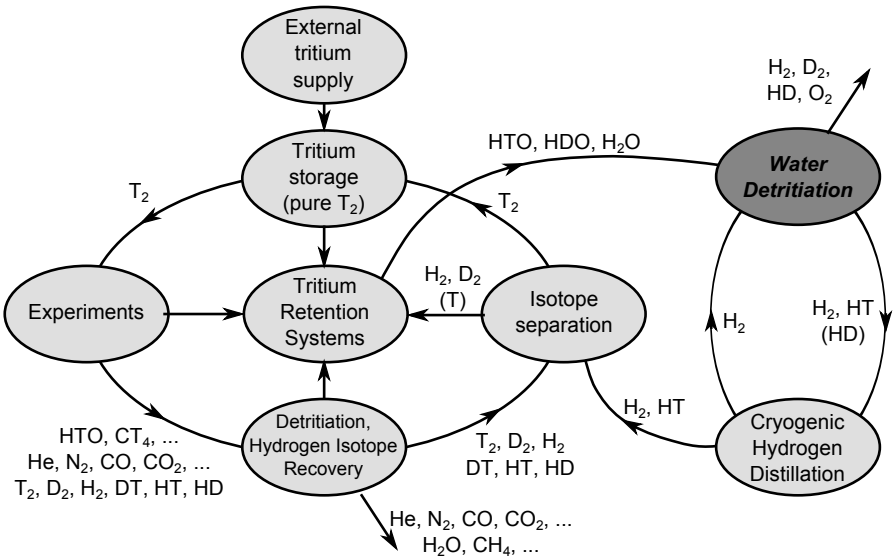

Figure 1.2: **The closed tritium cylcle of TLK.** The arrows represent the transport of gases/liquids via pipelines and/or transport vessels. The figure shows the same as Fig. 1 of Ref. [4]

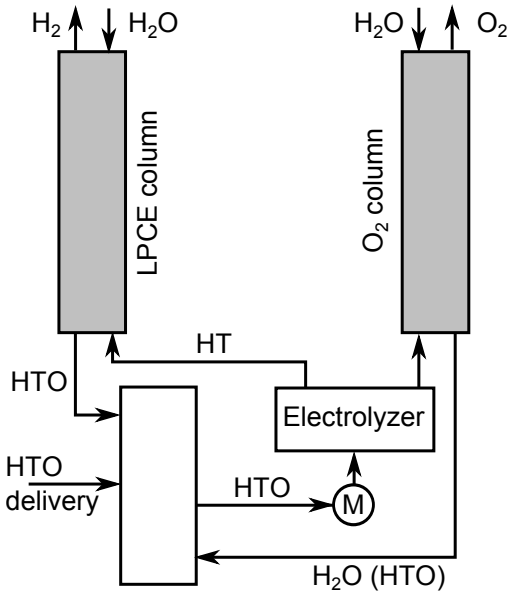

Figure 1.3: **Schematic structure of the TRENTA facility at TLK.** The LPCE (Liquid Phase Catalytic Exchange) column enriches tritium in the water, the O_2 column cleans the oxygen exiting the electrolyzer. The extraction of tritium will be done by means of a cryogenic distillation column, currently under development in TLK. The point to measure the tritium concentration is denoted with "M".

2 Tritiated water properties, processing, and activity measurement

In this chapter first the properties and processing of tritiated water are described briefly. After that, the methods of tritiated water activity measurement are described and discussed, serving as a motivation of the present work.

2.1 Properties of tritium and tritiated water

Tritium is the third isotope of hydrogen, with one proton and two neutrons in its nucleus. This nucleus is unstable and decays as follows [3]:

$$\mathrm{T} \rightarrow {}^{3}\mathrm{He} + \mathrm{e}^{-} + \overline{\nu}_{\mathrm{e}} \ , \tag{2.1}$$

with a half-life of approximately 12.3 years. The decay energy is distributed between the three resulting particles, therefore their energy spectrum is continuous. The ^{3}He nucleus carries a very small fraction of the energy due to the conservation of momentum and its large mass. The electron-antineutrino ($\overline{\nu}_e$) reacts very rarely with matter, therefore practically only the β-decay electron affects it surroundings. The energy spectrum of tritium β-decay electrons is continuous, and has an endpoint energy of approximately 18.6 keV, as it is illustrated in Fig. 2.1.

Tritium at normal temperature and pressure (273 K, 10^5 Pa) is a gas, forming two-atom molecules, and having the same chemical properties as hydrogen. Due to its chemical properties it can easily substitute hydrogen atoms in a water molecule, and form tritiated water (hereinafter also abbreviated as HTO[1]). The beta radiation of tritium can break up the water molecules (radiolysis), which then form radicals in the water. This results in a corrosivity higher than that of non-tritiated water [39], [40].

Chemically, tritiated water molecules behave similar to normal water, therefore they can also substitute normal water in the human body, which leads a high radiotoxicity of tritiated water [21]. Therefore, it has to be specially handled (see next section).

[1] Pure tritiated water (without hydrogen or deuterium in the water molecules) of course contains T_2O molecules, but this form is produced only in special experiments. Tritiated water in the concentration range of water detritiation facilities (some kBq/ℓ to several GBq/ℓ) contains some ppm tritium, and since the tritium atoms are evenly distributed among the water molecules in equilibrium, most tritiated molecules are HTO.

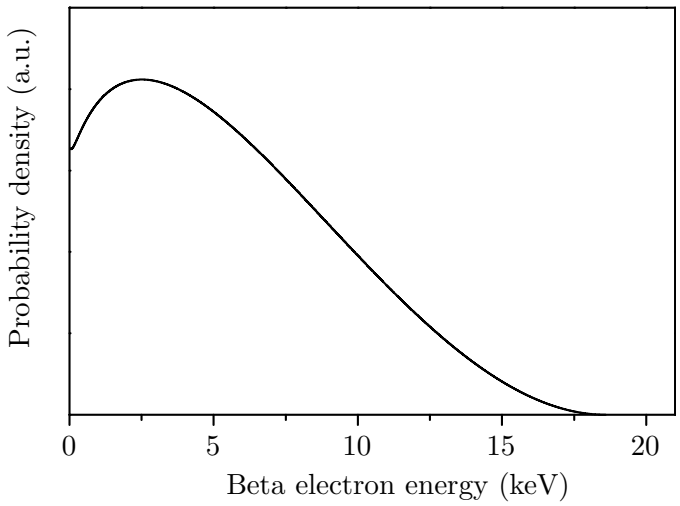

Figure 2.1: **Energy spectrum of the tritium β-decay electrons.**

2.2 Processing and measurement of tritiated water in a tritium facility

The source of tritiated water can be experiments with tritium, or the air cleaning system of the glove boxes of the laboratory. Most of tritiated water comes from the latter. This tritiated water can have a concentration from some kBq/ℓ to several MBq/ℓ. The tritium content of this water has to be extracted, not only because it is toxic, but because tritium is a valuable material. The fist step of this extraction process is the enrichment of the tritium in the water up to the range of several GBq/ℓ.

At the Tritium Laboratory Karlsruhe this is done by means of the Liquid Phase Catalytic Exchange (LPCE) process. Details on this process can be found in [22]. After enrichment, the tritium from the tritiated gas stream can be extracted by means of e.g. cryogenic distillation. During the LPCE process the tritium concentration has to be monitored. Traditionally this is done by taking samples of the water and performing offline measurements. Since it is dangerous to handle tritiated water with concentrations up to several GBq/ℓ, a realtime and inline monitor for tritiated water would be advantageous, but such systems are not commercially available.

Concerning the structure and materials of such a detector, due to the radiotoxicity of tritiated water, the processing of such water requires special procedures as described e.g. in the regulations for TLK [24], from which the most important ones are:

- a closed system with a low integral leak rate ($< 10^{-5}$ mbar$\cdot\ell$/s for He),
- maintenance done under a fume hood or in a glove box,
- metal parts are preferable for containment.

Therefore, it is advantageous to build a tritium monitor from standard industrial parts, with as simple structure as possible, then it is easier to assure low leak rate and main-

Table 2.1: **Comparison of methods available for tritium activity measurement.**

	Method			
	IC	LSC	Calorimetry	BIXS
Measured quantity	Ionization current	Scintillation light pulse count rate	Decay heat	Count rate of X-rays induced by decay particles
Detection limit	10-100 kBq	$\simeq$ Bq	$\simeq$ GBq	$\simeq$ MBq
Sample form	Gas, vapor	Liquid	Gas, liquid, solid	Gas, liquid, solid
Advantages	Simple	Standardized, reliable	Any sample form	Any sample form
Disadvantages	No liquid sample	Offline, radioactive and chemical waste	Long measurement time, detection limit	X-ray windows have to be thin

tainability. The requirements specific to the detector to be used later at the TRENTA facility in TLK, agreed during discussions with the TRENTA team, are [23]:

- an inline monitor, the water flows through the detector,
- measurements close to realtime: one measurement at least every 10 min,
- a detection limit <MBq/ℓ,
- range up to several GBq/ℓ.

The methods that can be used to measure tritiated water activity include ionization chambers (IC), liquid scintillation counting (LSC), calorimetry, and Beta Induced X-ray Spectrometry (BIXS). These methods are compared in Table 2.1.

An ionization chamber for tritium consists of a chamber filled with the gas to be measured, and two electrodes connected to a voltage source. A sensitive ammeter measures the ionization current produced by radiation in the fill gas (this current is on the order of pA), which is a function of the activity. A liquid sample has to be evaporated to be measured in an IC, which complicates the measurement. However, this method requires the simplest equipment, as far as the detector itself is concerned.

The LSC method is the standard method used for tritium measurement in water, it is the "workhorse" of many laboratories. The working principle is as follows: a sample of the water (some µl or ml, depending on the tritium concentration) is mixed with a scintillator fluid in a vial. The scintillator absorbs the tritium β-radiation via ionization, and converts it into visible light, which is then measured by means of a photodetector. It is a very reliable method, but on the other hand it produces organic radioactive waste, as the scintillator is not reusable. It is also complicated to fabricate an online LSC detector. Nonetheless some efforts have been made in this direction [20].

A calorimeter measures the heat produced by radiation [9]. The calorimetric method is adequate for all sample forms, but the detection limit is on the order of GBq, which is too high in this specific case, as the concentration of tritiated water can be lower than some MBq/ℓ. Besides, it requires measurement times on the order of hours to days [9] [10], therefore is not suitable for a realtime measurement.

A BIXS detector measures the bremsstrahlung produced by the tritium β-radiation. It is still under development for tritium measurement in water [11], [12]. Its detection limit is high compared the concentration range considered here [13], and the necessity of thin beryllium windows can cause safety issues.

Since the LSC method has the lowest detection limit (see Table 2.1), the scintillation counting method has larger potential than the other methods in terms of detection limit. To overcome the disadvantage of LSC, in particular that the scintillator is not reusable, a solid scintillator can be used. A plastic scintillator is a suitable choice, since it can be easily formed. Therefore, a detector using a plastic scintillator has been built and tested in the course of this work to investigate its potential as a tritium monitor.

3 The scintillation counting method for tritium activity measurement in water

In this chapter, as a theoretical foundation, the interaction of fast electrons and photons with matter is summarized. Then the detection process of a scintillator detector in general is discussed. After this, the main parts of a scintillator detector (scintillator, light detector and electronics) are described. Finally, the goals of the present work are outlined. The theoretical and technical principles described in this chapter are based on the reference books of Knoll [5], and Birks [6].

3.1 Interactions of fast electrons and photons with matter

In this thesis only particles in the energy range of the tritium β-decay electrons (0-18.6 keV) are considered, as these are the particles which play a role in detectors measuring tritium radiation.

Electrons in matter interact mainly with the orbital electrons, and sometimes with the nuclei, both due to the Coulomb force. In an electron-electron interaction the masses are equal, so the electrons can lose significant amount of energy in each collision. As a consequence of the frequent collisions, the trajectory of fast electrons is much more tortuous as, for example, that of the alpha particles. According to classical theory, bremsstrahlung can be emitted, due to the frequent accelerations.

The energy loss of particles in matter is characterized by the specific energy loss: $-dE/dx$, where dE is the energy change of the particle while traveling a path dx in the material. The energy loss of an electron is due to collisions and bremsstrahlung:

$$\frac{dE}{dx} = \left(\frac{dE}{dx}\right)_{co} + \left(\frac{dE}{dx}\right)_{br} . \tag{3.1}$$

The ratio of the two specific energy losses is approximately:

$$\frac{(dE/dx)_{br}}{(dE/dx)_{co}} \approx \frac{EZ}{7 \cdot 10^5} , \tag{3.2}$$

where E is the electron's energy (in keV) and Z is the atomic number of the absorbing material.

Due to the energy losses, an electron has a limited range in a given material before it loses all its energy. Typical values for electrons with the maximal tritium beta energy (18.6 keV) range from centimeters in gases to micrometers in liquid materials, and can be even smaller for solids [8].

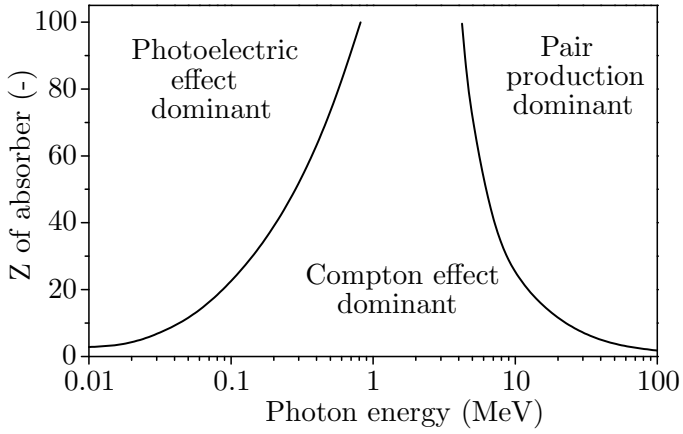

Figure 3.1: **The "map" of the dominant photon interaction.** The lines represent the energy-atomic number pairs, for which the neighboring effects have equal probability. Drawn after Fig. 2.20 of Ref. [5].

Photons have no charge, therefore they behave differently in materials. Their interaction with matter can take the form of photoelectric effect, Compton scattering, coherent scattering and pair production. The last one is only possible if the photon energy exceeds the energy equivalent to two electron masses (1.02 MeV), and therefore is not considered here. The dominating process changes for different photon energies and material atomic number (Z), which is illustrated in Fig. 3.1 for energies above 10 keV.

The photoelectric effect occurs when a photon interacts with an electron, thereby losing its total energy and liberating the given electron. This photoelectron receives the remaining energy:

$$E_e = E_\gamma - E_b \ , \tag{3.3}$$

where E_γ is the photon's energy, and E_b is the binding energy of the ejected electron. The probability of such an event (Pr(photoelectric effect)) depends on the density of available electrons, hence on the atomic number of the material, and on the energy of the photon. A rough approximation is:

$$\Pr(\text{photoelectric effect}) \approx const. \times \frac{Z^n}{E_\gamma^{3.5}} \ , \tag{3.4}$$

where n is a number between 4 and 5. Therefore the probability is higher for lower photon energies and for high-Z materials.

The Compton effect or Compton scattering is an inelastic collision between a photon and an orbital electron in which the incoming photon is deflected by the electron, but does not lose all its energy to it. The energy gain of the electron depends on the scattering angle, therefore the energies of the particles after scattering show continuous distributions. If the binding energy of the electron is negligible compared to the energy

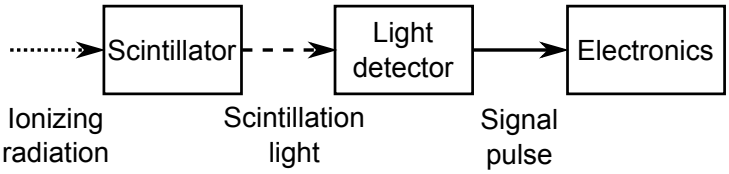

Figure 3.2: **The scintillation detection process.**

of the gamma photon, the energy gained by the electron due to the scattering is:

$$E_e = \frac{\frac{E_\gamma^2}{m_0 c^2}(1-\cos\theta)}{1+\frac{E_\gamma}{m_0 c^2}(1-\cos\theta)} \,, \tag{3.5}$$

where E_γ is the photon's energy before scattering, m_0 is the rest mass of the electron, c is the speed of light in vacuum, and θ is the angle of the photon's deflection. This means, that since θ can vary from 0 to π, the Compton electrons have a continuous energy distribution. The probability of Compton scattering is proportional to the atomic number of the material, and decreases with increasing photon energy. In the energy range of 0-18.6 keV Compton scattering is dominant over the photoelectric effect only in very light materials ($Z < 4$) (see Fig. 3.1).

Coherent scattering is a process where no energy is transferred between the photon and the other particle, but the photon is deflected from its original path. Therefore this process can influence the pathlength of the photon in a given material, which in turn can alter the transport of photons. This process is more pronounced for low photon energies under a few hundred keV, and for high-Z materials.

3.2 The detection process in a scintillation detector

A scintillator detector consists of three main parts: the scintillator, the light detector and the pulse-processing electronics (Fig. 3.2). The scintillator is a material which converts the energy of the incoming ionizing radiation to visible or UV light. When a particle hits the scintillator, one or more scintillation photons are produced. The number of produced photons carries information about the energy of the particle. The exact relationship depends on the properties of the particle (type, energy, momentum, see Section 3.3).

The production of scintillation photons is a statistical process. The number of scintillation photons for the same kind of event (with the same particle arriving to the same part of the scintillator, with the same particle energy, particle momentum, etc.) is different from event to event, and can be described with Poisson statistics [7]: the number of scintillation photons varies around a mean value (n) with standard deviation $\sqrt{n}$. Therefore, all statements about the number of scintillation photons from a scintillator refer to the mean number of photons.

A certain portion (in an optimal case nearly 100%) of the scintillation photons reach the light detector, which has to be sensitive enough to detect a small number of photons. The detector then produces a signal pulse, which has a height proportional to the number of photons hitting the detector. The signal pulse of the detector is processed by the electronics, and as a result a pulse height spectrum is produced (see Section 3.5). This spectrum corresponds to the energy spectrum of the detected particles.

3.3 Organic scintillators

In this work only organic scintillators are described, since the experiments were carried out with an organic plastic scintillator.

The scintillation process is based on the excitation of orbital electrons in matter by ionizing radiation. In the case of organic scintillators the material contains such organic molecules, like anthracene, which have a so called π-electron structure. The structure of the electron energy levels is illustrated in Fig. 3.3. After excitation, the excess energy above the S_{10} state is dissipated through non-radiative processes. This means, in practice, the passing of an energetic particle rapidly causes excitation of the molecules into the S_{10} state. The molecule can then be de-excited into one of the S_0 states, through the

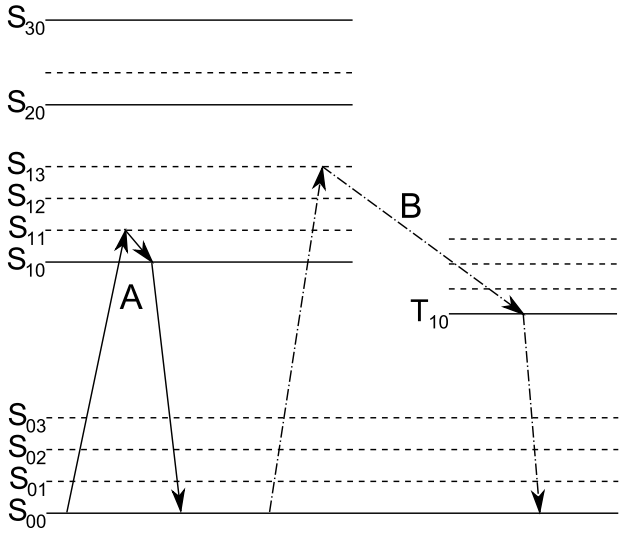

Figure 3.3: **Energy levels of an organic scintillator molecule, with two possible scintillation processes.** The levels S_{ij} show the i-th singlet state (spin 0) and the j-th vibrational state of the molecule. The levels T_{ij} correspond to triplet states (spin 1) in a similar manner. Process A: Excitation, non-radiative internal conversion, fluorescence. Process B: Excitation, intersystem crossing, phosphorescence (this figure displays the same as Figure 8.1 of [5]).

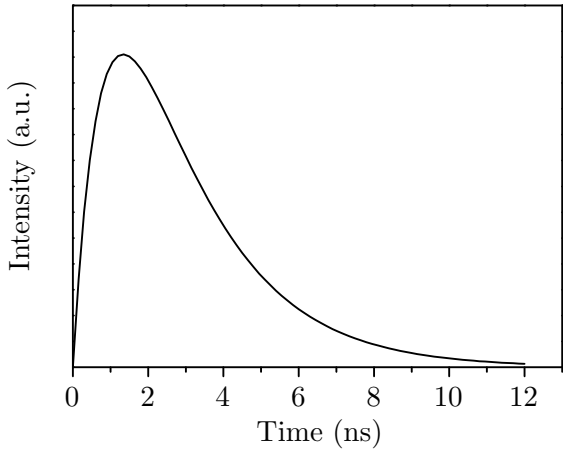

Figure 3.4: **Time dependence of scintillation pulse intensity** The graph shows Eq. 3.6 with parameters $\tau = 2.1$ ns, $\tau_1 = 0.9$ ns (properties of the BC-408 plastic scintillator from Saint-Gobain Ceramics and Plastics, Inc., [14]), $I_0 = 1$. $t = 0$ is the time when the ionizing particle passed.

emission of a scintillation photon. This process is called prompt fluorescence (process 'A' in Fig. 3.3), because usually it happens in the order of nanoseconds. If the energy is transferred to a triplet state (inter-system crossing, see process 'B' in Fig. 3.3), the release of the scintillation photon can be delayed due to the longer lifetime of the triplet states (the latter can be as much as 10^{-3} s). This process is called phosphorescence.

The population of the S_{10} levels in the molecules and their decay also has a characteristic time constant. Therefore, the intensity of the emitted scintillation light follows a function similar to the one in Fig.3.4. A model function for the scintillation light intensity I is a combination of two exponentials:

$$I = I_0 \left(e^{-t/\tau} - e^{-t/\tau_1} \right) \ , \tag{3.6}$$

where I_0 is a constant, t represents time, τ is the decay-, and τ_1 is the population time constant of the S_{10} levels.

The amount of emitted light from organic scintillators as a response to energetic particles is usually described by means of the fluorescence energy, L, emitted per unit path length: dL/dx. For many scintillators and high energy particles this is proportional to the specific energy loss of the particle:

$$\frac{dL}{dx} = S \cdot \frac{dE}{dx} \ , \tag{3.7}$$

which would imply a linear relationship between the energy loss of the particle and the intensity of the emitted light pulse. However, according to Birks [6], the incoming particle not only excites the molecules along its path, but also causes changes in the electronic structure of the molecules, e.g. by ionizing some of them. Let the ratio of

such "damaged" molecules to the "undamaged" ones be proportional to the specific energy loss: $B \cdot dE/dx$. The excitation energy of the molecules can be transferred from molecule to molecule in the material, and will be eventually either captured by a "damaged" molecule and lost (this is also called quenching), or be captured by an "undamaged" molecule and radiated as scintillation light. Let the probability of energy capture by a "damaged" molecule relative to an undamaged one be k, then the Birks equation [6] states:

$$\frac{dL}{dx} = \frac{S\frac{dE}{dx}}{1 + kB\frac{dE}{dx}} , \tag{3.8}$$

where S is the absolute scintillation efficiency (or yield), e.g. for anthracene $S = 0.038$ [6].

It is customary that in Eq. 3.8 the specific energy loss is normalized with the density of the material in which the particle is decelerated (ρ), and the resulting quantity is called the stopping power of the material:

$$\frac{dE}{dr} = \frac{1}{\rho}\frac{dE}{dx} \tag{3.9}$$

where $r = \rho \cdot x$. The scintillation yield can be expressed in photons per deposited energy (S_p). If additionally kB is expressed in units of g/(MeV·cm^2), then Eq. 3.8 becomes:

$$\frac{dL_p}{dr} = \frac{S_p\frac{dE}{dr}}{1 + kB\frac{dE}{dr}} , \tag{3.10}$$

where L_p means the number of emitted photons. In order to obtain the number of scintillation photons for an electron with initial energy E_0, Eq. 3.10 is transformed by dividing with $\frac{dE}{dr}$:

$$\frac{dL_p}{dE} = \frac{S_p}{1 + kB\frac{dE}{dr}} , \tag{3.11}$$

then integrating:

$$L_p = S_p \int_0^{E_0} \frac{1}{1 + kB\frac{dE}{dr}} \,\mathrm{d}E = S_p \cdot B(E_0) \tag{3.12}$$

The integral can be calculated if the kB constant of the scintillator and dE/dr as a function of energy is known. For a vinyl-toluene-based scintillator, like the BC-408 used in the experiments in this work, $kB = 9.21 \cdot 10^{-3}$ g/(MeV·cm^2) [6], [44]. The values of dE/dr can be obtained from the ESTAR database from NIST [42]. Unfortunately, the database contains data only down to 1 keV, whereas values down to zero energy are required for the integration. To overcome this, we consider the following: The stopping

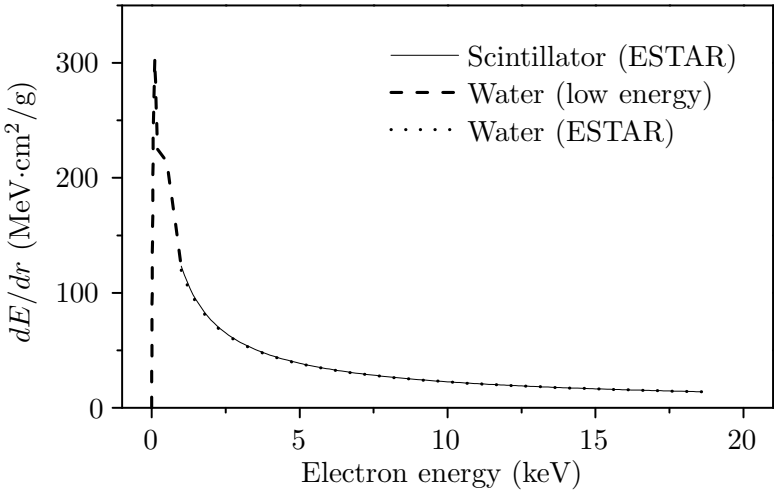

Figure 3.5: **Stopping power of the plastic scintillator and water for electrons.** The data is from the ESTAR database [42], and from [43] (for water at low energy). It can be seen, that the stopping powers of the two materials are almost identical over 1 keV.

power of water in the range 1-18.6 keV, as obtained from the ESTAR database, is very close to that of the scintillator, as shown in Fig. 3.5, due to the fact that they have similar densities and similar average ionization energies ($I_{sci} = 64.7$ eV, $I_w = 75$ eV, from [42]). Therefore it is plausible, that the stopping powers of water and plastic scintillators are at least similar for lower energies, too. The stopping power data of water is available also for lower energies, see Ref. [43]. As an approximation, the curve of $\frac{dE}{dr}$ for of the scintillator is extended using the measurement data from [43] (Fig. 3.5), with linear interpolation between the points.

By means of the extended curve, the function $B(E_0)$ in Eq. 3.12 is calculated by numerical integration for 150 different energies, and plotted against E_0 in Fig. 3.6. The graph shows how the process of quenching affects the light response of the scintillator: For energies under about 5-6 keV, where the stopping power (dE/dr) of the scintillator is higher (see also Fig. 3.5), the response curve becomes strongly non-linear.

Electrons in the tritium beta energy range cause mainly excitation and ionization in organic scintillators. For an electron with an energy of 5.7 keV (average energy of tritium betas) in a low-Z material (e.g. carbon, $Z = 6$, which is in the molecules of organic scintillators), the collisional losses are $2 \cdot 10^5$ times higher than those due to bremsstrahlung according to Eq. 3.2. Therefore virtually all of the electron's energy is deposited in the scintillator, causing scintillation.

Energetic photons in the range of interest will interact with the organic scintillators via the photoelectric effect and Compton scattering. Since the organic materials contain mainly hydrogen and carbon (Z=1 and 6, respectively), the two effects are comparable (see Section 3.1). The electrons resulting from these interactions then undergo the above described scintillation producing process. In the case of the Compton effect, the energy

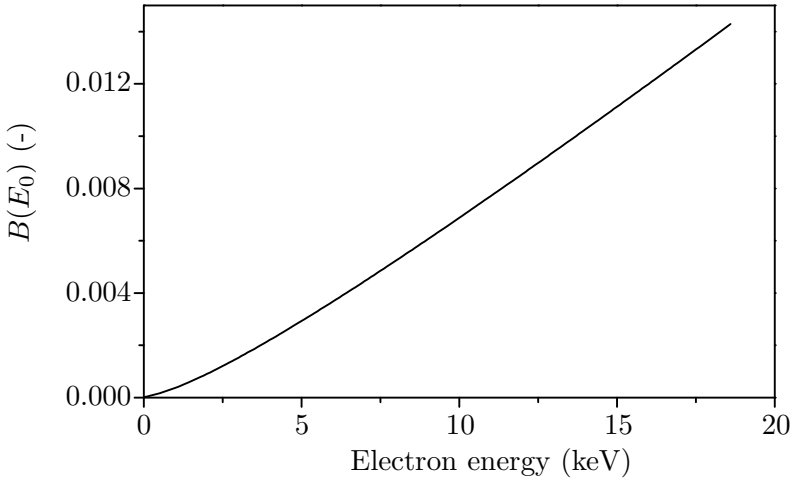

Figure 3.6: **The $B(E_0)$ function.** The values are calculated using $kB = 9.21 \cdot 10^{-3}$, and the $\frac{dE}{dr}$ values plotted in Fig. 3.5.

transferred to the scintillator electrons is continuous, therefore from one primary energy a wide distribution of scintillation light flashes with different intensities can be produced. The electrons from the photoelectric effect all have approximately the same energy if the binding energy of the electron is small compared to the photon energy.

The wavelength spectrum of emitted light from organic scintillators shows a relatively narrow distribution, as most of the photons are produced with the energy difference between the S_{00} and S_{10} states of the scintillator molecules. The emission spectrum of a scintillator is shown in Fig. 3.7.

Organic scintillators can be obtained in liquid or in solid form. The former is used in the LSC technique. Solid organic scintillators contain scintillator molecules dissolved in

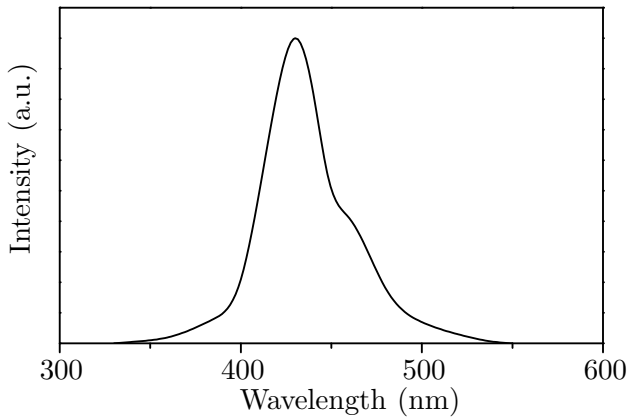

Figure 3.7: **Wavelength spectrum of the emitted light of a scintillator** The graph shows the emission spectrum of a BC-408 plastic scintillator [14].

a solvent, which is then polymerized (e.g. vinyl-toluene → polyvinyl-toluene). This way a plastic is obtained, which can be cast in various forms (rods, sheets, etc.).

3.4 Scintillation light detection

The scintillation light has to be detected by a sensitive detector. For this purpose the usual device is a photoelectron multiplier tube (PMT). Newer developments, such as the avalanche photodiode (APD) have better properties in some aspects, but a good PMT still has a lower dark count rate (10 to 1000 counts per second per cm^2 of photocathode area [7]), than e.g. an equivalent APD. The lower the expected count rate is in a detector, the lower the dark count rate (background) needs to be. The working principle of a PMT is based on two effects: photoelectric effect and secondary electron multiplication. The simplified structure of a PMT is shown in Fig. 3.8.

The PMT outer case is an evacuated glass envelope, which is equipped with the necessary electrical connections to the dynodes. The photocathode is a thin layer of solid material, deposited usually onto the inner surface of the PMT window. The dynodes and the anode are curved-sheet electrodes formed in such a way that they facilitate the collection and transport of secondary electrons (see later). The photocathode, the dynodes, and the anode (see Fig. 3.8) are connected to a high voltage supply by means of a voltage divider circuit, which supplies such an electric potential, that is increasing from the photocathode through the dynodes towards the anode.

During the photon detection process, first the photon has to reach the photocathode. The photon then undergoes the photoelectric effect, namely it first deposits its energy in the metal, thus generating an electron with excess energy. This photoelec-

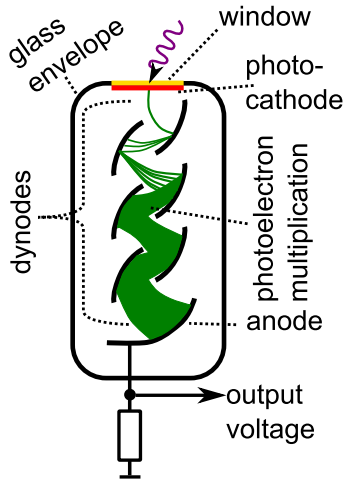

Figure 3.8: **Simplified structure and working principle of a PMT.** The auxiliary electronics (high voltage source, voltage divider, etc.) are not shown. The green lines/shaded areas show the trajectories of the electrons.

tron then migrates through the metal layer, and, if it has enough energy, escapes into the vacuum inside the tube. However, it can be absorbed in the metal with a certain probability; therefore the photocathode has an inherent efficiency, called the quantum efficiency (QE). This gives the probability that a photoelectron emerges from the inner photocathode, if one photon arrives at the outer surface:

$$QE = \frac{\text{number of photoelectrons emitted}}{\text{number of incident photons}} \ . \tag{3.13}$$

Usual maximum values of quantum efficiency are measured to lie between 20 and 30 percent, but the actual value is strongly wavelength-dependent. For long wavelengths (in the infrared region) the photon energy can be insufficient to cause the photoelectric effect, therefore towards long wavelengths the quantum efficiency tends towards zero.

Another characteristic of a PMT is its cathode sensitivity. Under the term sensitivity in this work we mean the *absolute spectral sensitivity*, which gives how much current the cathode gives if 1 W of light with wavelength λ falls onto it[1]. The sensitivity (S_λ) is measured in mA/W, it is strongly dependent on λ as it is in Fig. 4.6 in Chapter 4. The quantum efficiency can be calculated from the sensitivity (Eq. (2.3) from [7]):

$$QE = 1.24 \cdot \frac{S_\lambda}{\lambda} \ , \tag{3.14}$$

where λ is in nm. In addition, for the shortest wavelengths the transmission of the window limits the sensitivity.

Since the number of direct photoelectrons is very small, a multiplication of the electrons prior to detection is required, to enable them to be detected with sufficient signal-to-noise ratio. The voltage distribution on the dynodes causes the electrons to be accelerated from dynode to dynode and to be collected by the anode. As the electrons hit the dynodes, several secondary electrons are emitted. The ratio of the number of incoming and outgoing electrons at each dynode is called the multiplication factor:

$$g = \frac{\text{number of secondary electrons emitted}}{\text{number of incident electrons}} \ . \tag{3.15}$$

This ratio is a function of interdynode voltage and dynode material, typical values are about 3 to 10 for standard dynode materials, depending on the voltage between two dynodes (order of 100 V). If we assume the same multiplication factor for all stages, then the overall gain of an N-stage PMT is:

$$G = \eta g^N \ , \tag{3.16}$$

where η is the collection efficiency of the first dynode (percent of primary photoelectrons collected), which is above 80% in well designed tubes. Based on this, the overall gain of a ten-stage tube for a typical value $g = 5.5$ is on the order of 10^7. Since the multiplication

[1] for precise definition see Ref. [7], p. 2-2

factor depends on the voltage between the dynodes, the overall gain also depends strongly on the applied overall high voltage, HV. The overall gain is usually given as

$$G = K \cdot HV^{N\alpha} \ , \tag{3.17}$$

where K is a constant, depending on dynode material and the voltage distribution among dynodes, and α is a constant between 0.6 and 0.8 [7].

The electron multiplication is a statistical process, which can be roughly approximated as a Poisson process [7]. Therefore a single electron at a dynode induces on average g new electrons, with a standard deviation of $\sqrt{g}$. The relative variance of the number of electrons is then $1/g$. It can be proven from the properties of Poisson statistics, that for N stages the relative variance of the number of electrons at the anode is independent of the actual number:

$$\frac{1}{g} + \frac{1}{g^2} + \frac{1}{g^3} + ... + \frac{1}{g^N} \approx \frac{1}{g-1} \ . \tag{3.18}$$

The voltage between the photocathode and the first dynode is usually larger than between two dynodes to minimize statistical fluctuations, since here the number of electrons is the lowest. In this case the relative variance is still independent of the number of electrons.

The photocathode emits also electrons in complete darkness (i.e. no scintillation light), due to two factors: cosmic radiation and thermionic emission, the latter being dominant. This component contains mainly single electrons and it is strongly temperature-dependent. Therefore, cooling of the tube is often necessary, especially when weak scintillation signals are to be measured, in order to achieve a low and constant noise level.

If the PMT window is exposed to ambient light just before operation, the single electron noise is first very high due to the excitation of the electrons in the photocathode [7]. This noise increase sometimes takes several days to completely disappear. After switch-on, the gain of the PMT usually assumes a higher value as in continuous operation, and it also takes several hours or days to reach the "baseline" value (see also section 5.2.5).

In the optimal case, the scintillation light would reach the PMT directly, as in e.g. such scintillator detectors where the scintillator is mounted onto the PMT window. However, direct coupling is not always possible, and this causes light losses, which reduces the performance of the detector.

3.5 Detector pulse counting and analysis

In this section the so-called "pulse mode" operation of radiation detectors is considered, which is used in scintillation counting. A detector and the read-out electronics is schematically illustrated in Fig. 3.9.

The detector usually gives a current pulse similar to the one at step 1 in Fig. 3.9 (the pulse of a photoelectron multiplier tube is negative). This pulse contains a charge that is usually a function of the energy of the particle that induced it. If the energy information is important, the electronics "integrate" the pulse (Step 2). The electronic part that

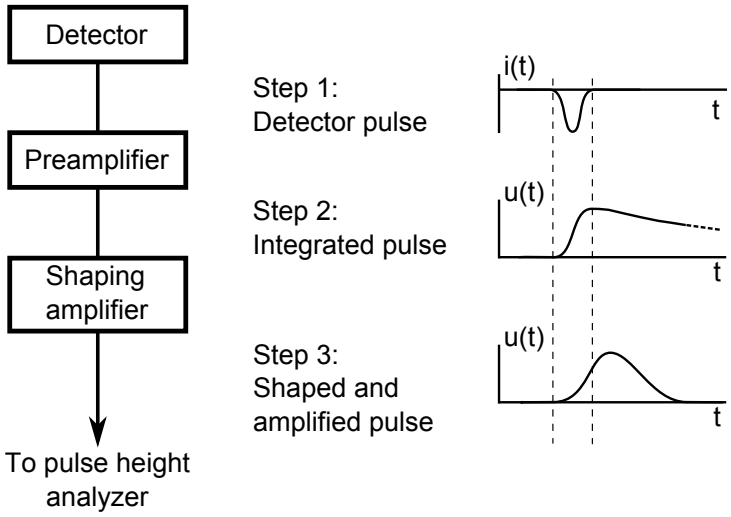

Figure 3.9: **Model of a detector in pulse mode operation with pulse shaping and amplifying electronics.** The pulse from the detector (negative in this case) is integrated in the preamplifier (and inverted if necessary), then shaped and amplified in the shaping amplifier. The pulses are not to scale, i(t) and u(t) means current and voltage versus time, respectively.

accomplishes this task is often called a preamplifier, however it does not amplify in the usual sense, but rather converts a current pulse into a voltage pulse. The height of the pulse is proportional to the charge in the detector pulse. It also decouples the detector from the rest of the electronics, so that the latter does not load the detector. The pulse provided by the preamplifier has a long "tail", because of its relatively big capacitance, necessary for the charge integration. The "tailing time" is usually on the order of 50 μs, determined by the time constant of the preamplifier $\tau_t = RC$, where R is the input resistance, and C is the input capacitance of the preamplifier.

The tailing of the pulse is unavoidable, but it can distort the result of the measurement, because of the so-called pulse pile-up effect. This means that in case of higher count rates the pulses can follow shortly one after the other such that they are sitting on each other's tails. Then the height of the pulses from the zero line does not reflect the original detector pulse charge anymore. To prevent this, the pulse is shaped to reduce the tailing (Step 3). This is done by differentiating, and then integrating the pulse several times. At the end the pulse shape is similar to a Gaussian peak, and has a much shorter tail.

The next step in signal processing is constructing the (differential) pulse height spectrum. This is done by measuring the amplitude of each pulse with appropriate electronics, and sorting them into predefined intervals (Fig. 3.10). Usually the signal is first digitalized (with an Analog-to-Digital Converter, ADC), then the sorting is done by a so-called MultiChannel Analyzer (MCA).

The pulse height spectrum then consists of bins which contain the number of pulses

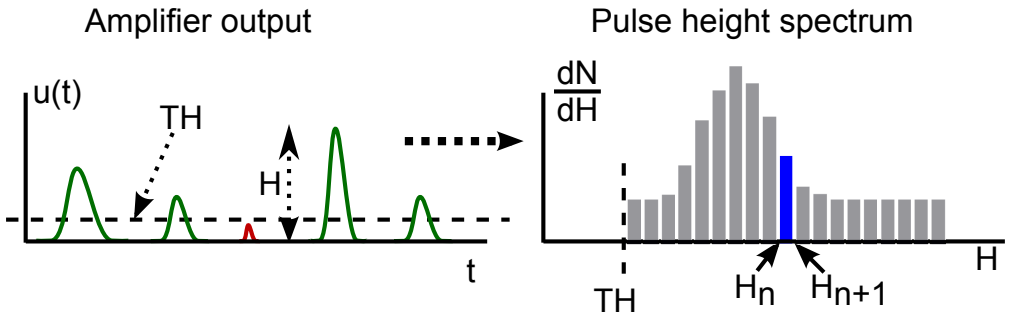

Figure 3.10: **The construction of a differential pulse height spectrum.** The pulses are discriminated against a preset level (threshold, TH), those smaller than TH are not measured (red pulse). The measured pulses are then ordered into "bins" and counted. The n^{th} bin (blue) then will contain the number of pulses (dN) with heights between H_n and H_{n+1} (in the interval of $dH = H_{n+1} - H_n$).

(dN) those heights were in the bin interval ($dH = H_{n+1} - H_n$). There is always a predefined lower limit for the pulse heights (threshold, TH in Fig. 3.10), which is necessary to exclude most of the electronics noise (e.g. the 50 Hz noise from the mains supply, etc.), since it is mostly constrained in amplitude.

Besides pile-up, another problem at high count rates is the deadtime of the detector. The detector has to return into its idle state after a pulse (the pulse has to return to the baseline, usually meaning zero signal current/voltage) and the electronics has to digitize, measure, and sort the pulse into the appropriate channel. The time needed for this is called deadtime. If the count rate is high, depending on the pulse shaping, several percent of the measurement time (also called realtime) is lost. This loss is unavoidable, and limits the measurable count rate. The "pure" time of pulse counting (i.e. realtime minus the deadtime) is called livetime.

One often-used noise reduction method in scintillation pulse counting (besides setting the threshold) is the coincidence technique: The scintillation counter contains two light detectors, which are both "watching" the scintillator, and connected to the electronics. Only those pulses which occur nearly simultaneously are counted by the electronics (within a time window of 1-10 ns). This way the noise is significantly reduced, because noise pulses are uncorrelated, while the real scintillation pulses from the same physical event happen nearly the same time, thus these are usually counted with full efficiency.

3.6 Previous studies and the goals of this study

There were several studies in the past, in which the possibility of a tritium-in-water monitor based on scintillators was investigated (Table 3.1). Here these studies are listed and discussed, with emphasis on the detection efficiency:

- Muramatsu et al. (1967) [16] used two PMTs in connection with coincidence

Table 3.1: **Comparison of various scintillator detectors for tritium measurement in water**

	Detection efficiency, η_{det} (cps/(Bq/ℓ))	Scintillator surface, F_{sci} (cm^2)	Specific efficiency, $\epsilon_{det} = \eta_{det}/F_{sci}$ (cps/(cm^2·Bq/ℓ))
Muramatsu et al. [16]	$3.85 \cdot 10^{-4}$	123	$3.13 \cdot 10^{-6}$
Moghissi et al. [17]	$4.5 \cdot 10^{-3}$	> 424.1	$< 1.06 \cdot 10^{-5}$
Osborne [18]	1.1	3000	$3.06 \cdot 10^{-6}$
Singh et al. [19]	3.2	3000	$1.08 \cdot 10^{-5}$
Hofstetter and Wilson [20]	order of 10^{-3}	some 100	order of 10^{-5} to 10^{-6}

electronics to eliminate thermal noise of the PMTs. The scintillator plate ("Pilot Scintillator B", produced by Pilot Chemicals, Inc.) was connected to a prism, which divided the scintillation light pulses for the two PMTs. The water sample was in direct contact with the scintillator. They reported a sensitivity range of $(2.6 - 5.1) \cdot 10^{-4}$ cps/(Bq/ℓ).

- Moghissi et al. (1969) [17] used a cell which contained 100 plastic rods coated with anthracene powder. The two PMTs they used were connected to the cell walls that the rods were connected to. The sensitivity was $4.5 \cdot 10^{-3}$ cps/(Bq/ℓ), approximately an order of magnitude higher than that of the previous work.
- Osborne (1969) [18] used thin NE 102 plastic scintillator plates (60 pieces, 5x5x0.0125 cm) stacked over each other also viewed by PMTs in coincidence mode. The sensitivity was even higher than the previous ones, 1.1 cps/(Bq/ℓ).
- Singh et al. (1985) [19] tested a tritium detector for detecting heavy water leaks in a nuclear reactor by means of detecting traces of tritium. The detector sensitivity was around 3.2 cps/(Bq/ℓ), using a scintillator sponge made of NE 102 scintillator.
- Hofstetter and Wilson (1991) [20] investigated several types of sample chambers with Yt silicate and BC-400 plastic scintillator beads of various sizes, and also scintillator fibers. The detection efficiency they found was in the 10^{-3} cps/(Bq/ℓ) range.

The detection limits of the various detectors were all in the kBq/ℓ range, but the detection efficiencies scatter over a wide range of four orders of magnitude. For a better comparison of the various detectors it is useful to calculate the detection efficiency per unit scintillator surface, shown in Table 3.1. One can clearly see that the specific efficiencies are all on the scale of 10^{-6} to 10^{-5}. This means that the converting efficiency

of decay energy into light, besides the scintillator quality, depends mainly on the scintillator surface, and not on the volume of tritiated water. The explanation for this is the short pathlength of beta particles in water (some micrometer, [8]).

The values of Moghissi et al. are higher probably because they used anthracene powder, which has the highest efficiency among organic scintillators. The detector of Singh et al. was very compact, which probably facilitated scintillation light propagation. A definitive explanation for the differences cannot be given without detailed calculations/simulations.

In conclusion, building of an organic solid scintillation detector for tritium detection seems promising. In a tritium laboratory, however, the concentration of tritiated water is much higher, than the tested concentration in the mentioned studies. Referring to the requirements in Section 2.2, the detector has to be tested with tritiated water with up to several GBq/ℓ concentration, which is one main difference to previous studies, because the effect of such a tritiated water on the scintillator is not known yet. Another significant difference is the consequence of the fact, that maintenance of a system which "sees" high levels of tritium is much more complicated, because it has to be done in a fume hood or glove box. Therefore it is advantageous if the detector is designed to be the simplest possible to ease maintenance. In our case this includes omitting the light coupling element between the sample chamber and the PMT, and using only one PMT for light detection. These can negatively affect the performance of the detector, by decreasing the signal and increasing background noise [5]. The test of the concept itself (i.e. tritium detection with organic scintillator) does not require a flow-through sample chamber, which is another simplification. Considering the above, the main goals of this study were (taking into account the requirements in Section 2.2):

- Build and test a detector, to see if its sensitivity and detection limit is adequate for a tritium facility.
- Investigate the effect of the detector geometry on the above properties to see if improvement is possible.
- Develop and test simulation code for the simulation of the detector behavior, to understand the detection process.
- Give a proposal for an improved design, based on these investigations.

These points are discussed in the following chapters.

4 The experimental setup

In this chapter the structure of the experimental setup is described in detail, and the technical specifications of the various components are given.

4.1 Overview of the setup

Considering the requirements listed in Section 2.2, the setup must feature an outer shell made of metal. One of the easiest ways to construct the outer shell is out of CF components[1], since these are robust, guarantee the required leak tightness, and glass windows built into CF flanges are available (separation of tritiated water from the PMT, but allowing the scintillation light to go through), while larger diameter CF parts can accommodate a PMT. In our case, the used PMT has an outer diameter of 51 mm, which meant that the simpler KF system could not be used (the largest available KF flange size is 50 mm diameter). The sealing rings used in the setup were made of Viton, because copper could have been corroded by the water.
The setup consists of two main parts: the sample chamber and the light detector (PMT), as shown in Fig. 4.1. The main component of the sample chamber is a glass cup, where the tritiated water is placed, together with the scintillator. This way the cup can be taken out to exchange the tritiated water or the scintillator plate(s). A more detailed description of these components is given in Section 4.2.

The outer shell components were manufactured at the VACOM Vakuum Komponenten & Messtechnik GmbH, Jena, Germany. The PMT housing (lower part in the photo in Fig. 4.1) is made of DN63 CF parts. The underside of the setup is closed with a DN63 CF blind flange, equipped with an SHV (high voltage) and a BNC (signal) feedthrough. The legs of the setup were made of aluminum profiles and aluminum plate.

4.2 Description of the components

4.2.1 Plastic scintillator material

The scintillator material of choice is BC-408 plastic scintillator from Saint-Gobain [14]. The edge of a scintillator plate made of this material is shown in Fig. 4.2. The properties of the BC-408 material are given in Table 4.1. Its density is close to water, however the refractive index is much greater than that of water (≈1.33) and also that of air (≈1),

[1] CF = ConFlat flange, a standardized vacuum flange system with copper or rubber sealing after the ISO 3669 norm

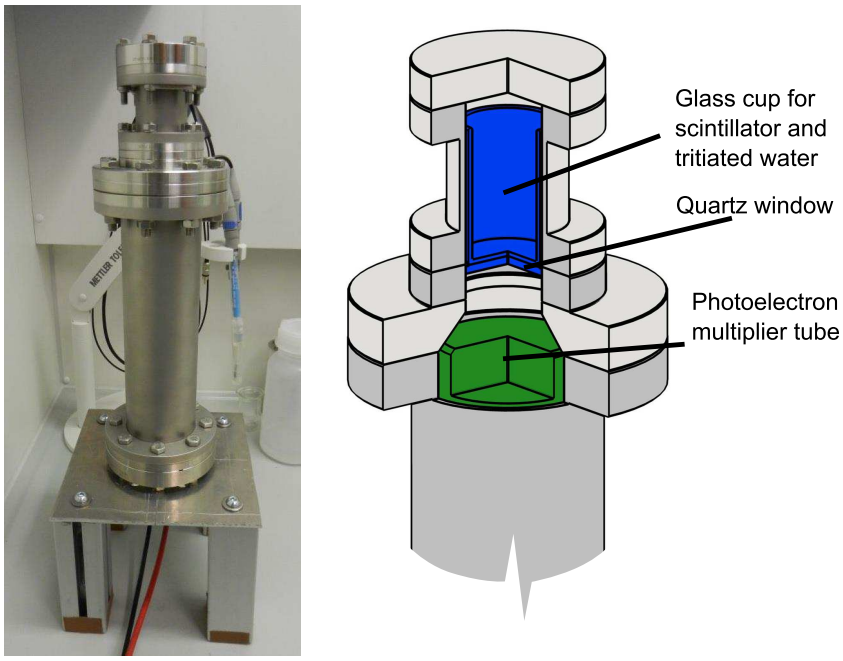

Figure 4.1: **The experimental setup.** Left: the setup in the fume hood in TLK. Right: three-quarter section view of the top part of the setup. The water, scintillator and the aluminum cup are omitted for clarity.

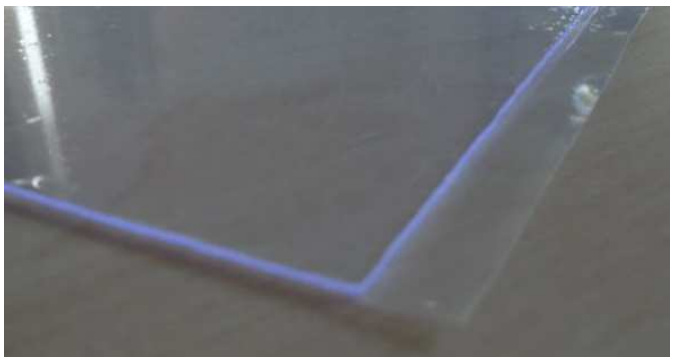

Figure 4.2: **The edge of a BC-408 scintillator plate.** The plate is covered with protective plastic foil. The edge emits scintillation light due to excitation by sunlight.

Table 4.1: **Properties of the BC-408 scintillator material.** Data taken from [14].

Property	Description/value
Base material	Polyvinyl-toluene
Density	1.032 g/cm^3
Refractive index	1.58
Light output	64% of Anthracene
Rise time	0.9 ns
Decay time	2.1 ns
Bulk light attenuation length	380 cm

therefore total internal reflection is possible on the surface of the scintillator, when it is in water or in air. The light output of BC-408 is given as 64% of that of Anthracene, meaning a scintillation yield $S_p = 9600$ photons/MeV. The emission spectrum of the scintillator was already shown in Fig. 3.7.

4.2.2 Sample chamber

The outer shell of the sample chamber is built up from a DN40 CF tube, 60 mm long, it is closed with a DN40 CF blind flange on one side. The other end is a glass window built into a DN40 CF flange (VACOM article nr. VPZ40QS-MB). The glass of the window is fused silica [26], its thickness is 3 mm, the transparent part of the window has a diameter of 32 mm. The inner parts of the sample chamber are displayed in Fig. 4.3. The glass cup is made of borosilicate 3.3 glass [27], with an outer diameter of 36 mm, height of 51 mm and a wall thickness of 2 mm. The transmission curve of the glass is shown in Fig. 4.4, together with the emission spectrum of the BC-408 scintillator. The glass shows near to maximum transparency to the light of the scintillator. The scintillator is a 0.5 mm thick circular plate with a diameter of 29 mm. It is cut from a scintillator plate made of BC-408. The scintillator holder is a 1-mm-diameter stainless steel wire, bent into the required shape. Its purpose is to keep the scintillator plate away from the bottom of the glass, so that the tritiated water can surround the scintillator completely. Also, the scintillator holder makes it easier to take out the scintillator. The aluminum cylinder is put around the glass cup to act as a reflector. It is manufactured in such a way that it tightly fits onto the glass cup from the outside (there is a minimal air gap, of the order of 0.1 mm, between the glass and the cylinder). The inner surfaces of the cylinder are polished to provide good light reflection (>80% reflectivity).

4.2.3 Photomultiplier

The photomultiplier in use was the XP-2262 from Photonis [30]. The device is shown in Fig. 4.5, its properties are listed in Table 4.2. The sensitivity of the PMT is close to its maximum in the wavelength-region of the scintillator light of BC-408, as it can be seen in Fig. 4.6. Using Eq. 3.14, and the data in Fig. 4.6 the maximal quantum efficiency of the PMT is 28% at 400 nm.

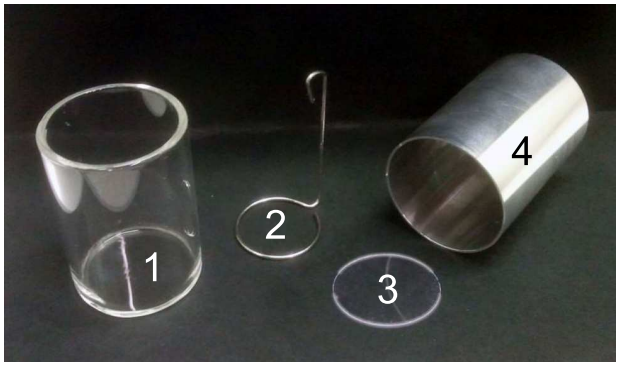

Figure 4.3: **Inner parts of the sample chamber.** 1: Glass cup, 2: Scintillator holder, 3: Scintillator, 4: Aluminum cylinder

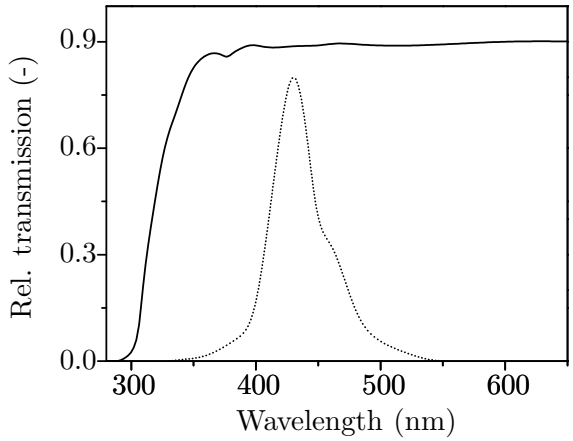

Figure 4.4: **Transmission of borosilicate glass.** This is the material of the glass cup used in the setup. The graph shows the bulk transmission of 8-mm-thick plane glass with a thick line. Additionally, the emission spectrum of the BC-408 scintillator material is drawn with a dotted line. The data of the glass is taken from [27], the scintillator spectrum is the same data as in Fig. 3.7.

Figure 4.5: **The XP-2262 PMT.** The voltage divider circuit board is visible on the right side, connected to the PMT.

Table 4.2: **Properties of the XP-2262 photomultiplier.** Data is taken from [30].

Property	Description/value
Window material	Lime glass
Window refr. index at 420 nm	1.54
Photocathode	Bi-alkali
Spectral range	290-650 nm
Maximum sensitivity at	420 nm
Supply voltage (typical)	1800 V
Gain at 1800 V	$3 \cdot 10^7$
Dark count	1000 cps

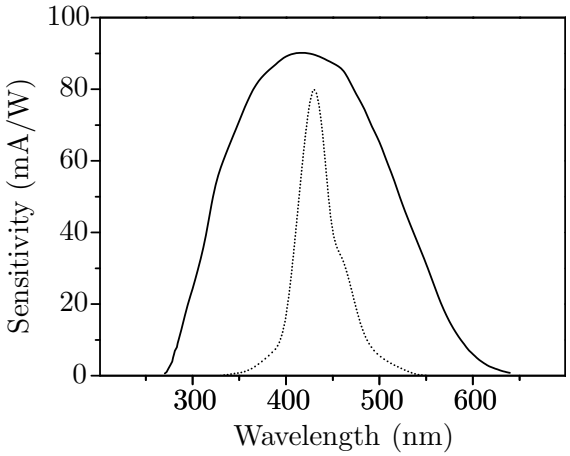

Figure 4.6: **Sensitivity curve of the XP-2262 PMT.** The dotted curve shows the relative emission spectrum of the BC-408 scintillator material. Sensitivity data is taken from [30], the scintillator data is the same as in Fig. 3.7.

Table 4.3: **Properties of the Ortec 556 high voltage supply.** Data is taken from [29].

Property	Description/value
Operating temperature	0-50℃
Output voltage	10-3000 V
Output current	0-10 mA
Output polarity	Selectable + or -
Voltage instability (inherent)	≤0.0025%
Instability due to temperature	≤ ±50 ppm/℃
Long-term drift (inherent)	<0.01%/hour, <0.03%/24-hours
Error in re-setting the voltage	<0.1%

4.2.4 Electronics

The high voltage supply and the main amplifier of the setup were built into an Ortec 4006 Minibin and Power Supply unit [28], as can be seen in Fig. 4.7. The preamplifier and the Analog-to-Digital Converter/MultiChannel Analyzer (ADC/MCA) were separate units. The high voltage supply is type 556 from Ortec, its specification is listed in Table 4.3. An Ortec 113 scintillation preamplifier was used, the data of this device is given in Table 4.4. The main amplifier was an Ortec 575A (for properties see Table 4.5). As ADC/MCA unit an Easy-MCA-8k from Ortec was used, which was controlled by means of the MAESTRO-32 program. The properties of the Easy-MCA-8k are given in Table 4.6. At the end of a measurement, the obtained spectrum (number of collected events for each channel), the realtime, and other information can be saved in a file. For calculating count rates the livetime can be used.

As outlined above, when exposed to ambient light, it takes several hours or days for a PMT to reach steady state operation. Therefore, a series of measurements have to be performed in order to be able to see when the PMT reached equilibrium conditions (details see in Section 5.2). For this purpose the MAESTRO-32 program was used in batch mode: A script was written, which then can be executed by the program, and contains all necessary steps to start and stop measurements one after the other. It also saves the data of each measurement automatically.

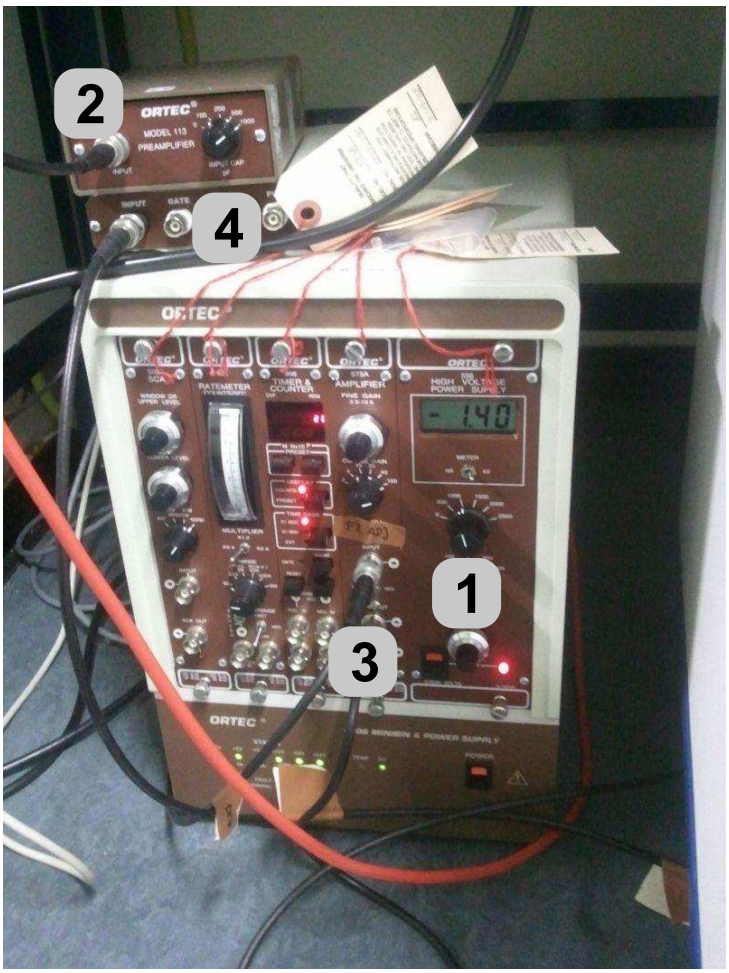

Figure 4.7: **The electronic components of the setup.** 1: High voltage supply, 2: Preamplifier, 3: Shaping amplifier, 4: Analog-to-digital converter and multichannel analyzer

Table 4.4: **Properties of the Ortec 113 Scintillation Preamplifier.** Data is taken from [31].

Property	Description/value
Type	Charge sensitive preamplifier
Input capacity	0 - 1000 pF, switch selectable
Rise time	<60 ns
Integral nonlinearity	≤0.02%
Output decay time	50 μsec

Table 4.5: **Properties of the Ortec 575A Amplifier.** Data is taken from [32].

Property	Description/value
Integral nonlinearity	$<\pm$0.05% for 1.5 μs shaping time
Noise	<7 μV
Operating temperature	0-50°C
Gain	5-1250
Output pulse shape	Semi-Gaussian, mono- or bipolar
Peaking time	0.5, 1.5 or 3 μs, selectable via jumpers

Table 4.6: **Properties of the Ortec Easy-MCA-8k.** Data is taken from [33]. Signal input properties are for semi Gaussian peaks.

Property	Description/value
ADC type	Successive approximation
Max resolution	8192 channels
Dead time per event	2 μs
Required input	Mono- or bipolar analog pulses, max 12 V
Accepted time constants	0.25 μs to 30 μs
Interface	High speed USB 2.0 (480 Mbps)

5 Measurements for characterization of the experimental setup

This chapter is dedicated to the first half of the experimental work with the setup described in the previous chapter. First, the settings of the electronics are discussed, then the optimized count rate calculation and the stabilization of the detector temperature are introduced. Next, the calibration procedure is discussed in detail, followed by several measurements with altered detector geometry.

5.1 Overview of the measurements

First, before the measurements had begun, the following parameters had to be set:

- Input capacity of the preamplifier, which regulates how the charge of the PMT pulses is collected
- Amplification of the main amplifier, the maximum of which determines the minimum measurable signal
- Peaking time of the main amplifier, which determines the photon collection time
- Threshold of the MCA, to exclude electronics noise
- Value of high voltage for the PMT, to set the amplification or gain of the PMT itself

Second, in order to have reliable measurements, the background has to be stable. If it is unstable, a change in the count rate due to some change in the sample cannot be distinguished from a change in the background count rate. However, as mentioned in Section 3.4, the emission of thermionic electrons from the photocathode is extremely temperature dependent. In case of only one PMT (no coincidence mode possible), the temperature of the tube has to be as stable as possible, otherwise the temperature changes can influence the background. Therefore in our case a cooling device was applied, see Section 5.2.4.

After applying the above settings, measurements were performed with tritiated water samples of various concentrations. The goal of these measurements was to investigate the sensitivity, detection limit, and linearity of the system, and also to see if memory effects occur. The count rate is expected to change linearly with the concentration if all other conditions are the same (electronics settings, PMT supply voltage, ambient temperature, measurement time, sample amount). This is because doubling the concentration doubles

the activity that surrounds the scintillator, causing twice the number of scintillation events.

The next investigation was about the effect of sample amount, that is, the level of water above the scintillator. Since, as mentioned before, the path-length of tritium β-electrons in water is on the order of micrometers, it was expected that more sample does not affect the amount of β-electrons reaching the scintillator. However, the beta radiation causes bremsstrahlung in the water, which can be measured with the appropriate apparatus [11], [13]. The bremsstrahlung photons can reach the scintillator and interact with it, this contributes to the signal of the detector. On the other hand, the probability of bremsstrahlung in low-Z materials is rather low (Eq. 3.2), and this can restrict the effect of sample amount. The amount of water also changes the optical properties of the setup, which can affect the number of photons reaching the PMT, and can have an effect on the sensitivity.

Another question is how the signal changes if the scintillator has a bigger surface in contact with water. Increasing this surface increases the number of scintillation events, but altering the scintillator arrangement alters the optical properties of the system. Therefore the signal increase might not be proportional to the surface increase.

5.2 Optimization of the setup

5.2.1 Setting the measurement parameters

For the first measurements, the PMT was supplied with 1450 V, to be able to provide test signals to the electronics. The signal went through the preamplifier and main amplifier, into a digital oscilloscope.

The input capacitance of the preamplifier was set to be 1000 pF (the maximum possible). At lower values of the capacitance, the signal peaks at the preamplifier output had an overshoot, which lasted some hundred microseconds. The origin of this phenomenon remained unclear. The peramplifier was checked using the standard procedure described in [31], and found to be working properly. It was observed that the overshoot was bigger if the peak was bigger, and could disturb the measurement by shifting the baseline of the signal, that is why the maximum capacity setting was chosen.

The amplification of the main amplifier was set to maximum (1250x) in order to have the biggest possible signal peaks at the output, even for single electron events. The pole zero cancellation of the amplifier was set such that the signal peaks had no undershoot.

The peaking time of the amplifier was set to be the longest possible, 3 μs. This value was chosen because this assures the detection of the maximum amount of photons in an event, even if they are "late" because of multiple reflections in the setup.

The threshold of the multichannel analyzer (MCA) was intended to be the lowest possible, in order to be able to register even the single photon events, but exclude electronic noise. To achieve this, the noise spectrum of the electronics alone was measured. The high voltage was switched off and the output of the main amplifier was connected to the MCA, then the spectrum was measured for 10 minutes. The result is shown in Fig. 5.1. As it can be seen the noise of the electronics extends to about channel 50. The count

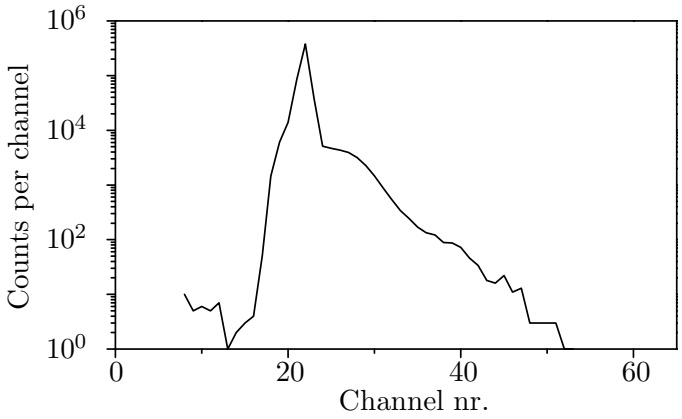

Figure 5.1: **Noise spectrum of the electronics without high voltage.** The scale of counts is logarithmic. The channels above 65 are not shown, because no counts were registered in those channels.

rate was so high that the deadtime of the detector was over 50%. To be on the safe side, the threshold was set to channel 60. This way only the unavoidable background from the PMT was processed by the MCA, and the deadtime resulting from electronics noise could be kept to the minimum.

The spectrum acquisition time was set to 10 minutes, and was not changed afterward, because this is the specified maximum measurement time (see Section 2.2), providing the maximum amount of counts, thus minimum possible statistical error [5]. The MAESTRO-32 program calculates the deadtime and the livetime of the measurement. The count rates (CR) mentioned in this work were calculated using the livetime:

$$CR = \frac{C}{T_{live}} \tag{5.1}$$

where C is the counts during the measurement, and T_{live} is the livetime.

5.2.2 First measurement series

The first measurements were performed at PMT supply voltages 1400, 1450 and 1500 V. The intention behind the relative low operation voltage was to exclude the single electron peak for background reduction. The main goal of the measurements was to prove if the concept was working, and if possible find an optimum operating voltage. These measurements are described in detail in [35].

Five measurements were performed at each voltage, using five different tritiated water mixtures with different tritium concentrations. The obtained data for 1500 V PMT supply voltage is plotted in Fig. 5.2. As it is apparent from the graph, the response of the detector is not linear as it would be expected. Similar results were obtained at the other supply voltages. Moreover, the results were not reproducible: the measured count rates in the different measurements differed several times the uncertainty margins.

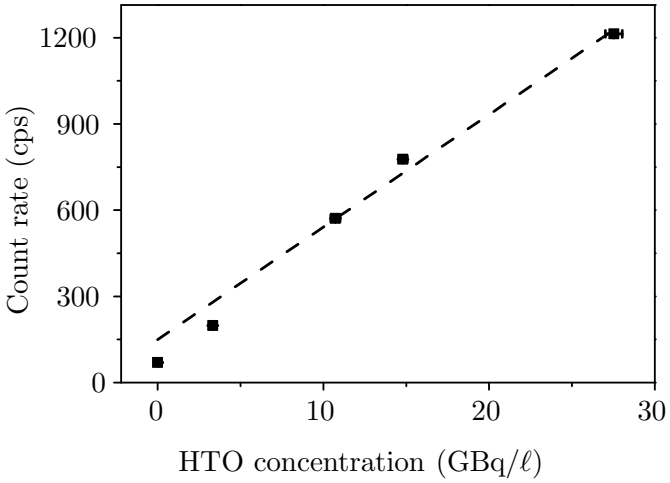

Figure 5.2: **Calibration curve from one of the first measurement series.** Electronical settings as in Section 5.2.1, supply voltage 1500 V. The data points are drawn with the error bars, but these are comparable in size to the data points.

Possible explanations of the above results include gain drift of the PMT because of the on-off switching between measurements and background change due to temperature changes (the air temperature of TLK is regulated, however not exactly constant).

5.2.3 Optimization of the high voltage and the count rate calculation

To have reproducible measurements, the high voltage had to be optimized, so that the single electron peak (SEP, mentioned in Section 3.4) becomes visible in the spectrum, since it is a reliable fixed point to which the rest of the spectrum can be compared to. To find the single electron peak, the high voltage was set to various levels from 1700 V to 2000 V in 50 V steps, and the resulting background spectrum was measured for 10 minutes at each voltage. Fig. 5.3 shows the background spectrum at some voltages. As is apparent, above 1700 V a peak shows up, which slides to the right and broadens as the voltage is increased. This peak seems to be the single electron peak. To be sure that really the SEP was found, the peak position of this peak was determined at various voltages (1750 to 2000 V) the following way: The approximate peak position (APP, channel number at the maximum value) of the peak was estimated from the graph of the spectrum. Then the data corresponding to the channel interval $[APP{\cdot}0.7\ ,\ APP{\cdot}1.3]$ was cut from each spectrum, and the following Gaussian curve was fitted onto it:

$$C = A \cdot exp\left[-\frac{1}{2}\left(\frac{CH - PP}{\sigma}\right)^2\right] , \tag{5.2}$$

where C is the count at a particular channel, A is a constant, proportional to the area under the Gaussian curve, σ is the standard deviation of the curve, CH is the channel

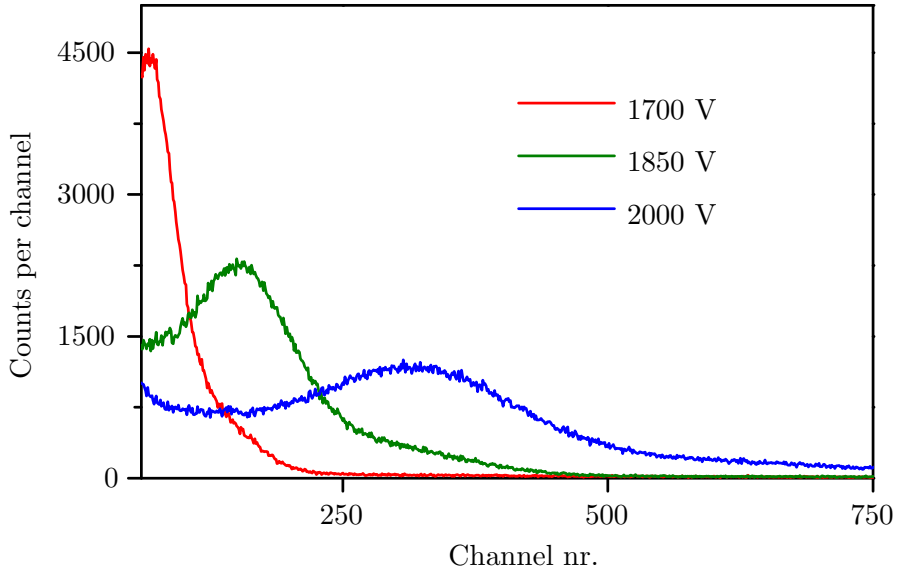

Figure 5.3: **Background spectra of the XP-2262 PMT at various high voltages.** The spectra hereafter are shown above the threshold.

number, and PP is the center of the curve, hereafter called the peak position.

The peak position was plotted against the PMT voltage (Fig. 5.4). According to Eq. 3.17, the gain of a PMT is a power function of the applied high voltage. Therefore, assuming a linear amplification of the pulses, the position of a peak in the spectrum is also a power function of the high voltage, with the same exponent. To find this exponent, the points in Fig. 5.4 were fitted with the following function in Origin:

$$PP = a \cdot HV^b \ , \tag{5.3}$$

where HV is the high voltage, a and b are the fit constants. The fit gave a value of $a = 9.45 \pm 0.05$, which is close to the value given in the datasheet of the PMT (typical value: 9, [30]). Taking into account that in complete darkness the PMT produces mainly single-electron pulses due to thermionic emission (Section 3.4), it is reasonable to identify the peak in the background spectrum as the single electron peak. The center of the Gaussian belonging to the SEP is hereafter called the single electron peak position, abbreviated SEPP.

There is no *exact* value of the high voltage that would be appropriate for the measurements. The main aspect is to have the SEP clearly visible, since it is a reference point in the spectrum. This is achieved at 1850 V, while most of the lower amplitude noise is excluded. Therefore, 1850 V was chosen as the operating voltage.

During the experiments presented in this chapter, if the sample chamber was opened for e.g. sample change, the PMT had to be switched off, because ambient light to a working PMT can be fatal [7]. After switch-on the gain drifted, as mentioned in Section 3.4. This, and any other gain drift was compensated the following way: the center of the SEP was found by fitting a Gaussian as described before in this section. The half of

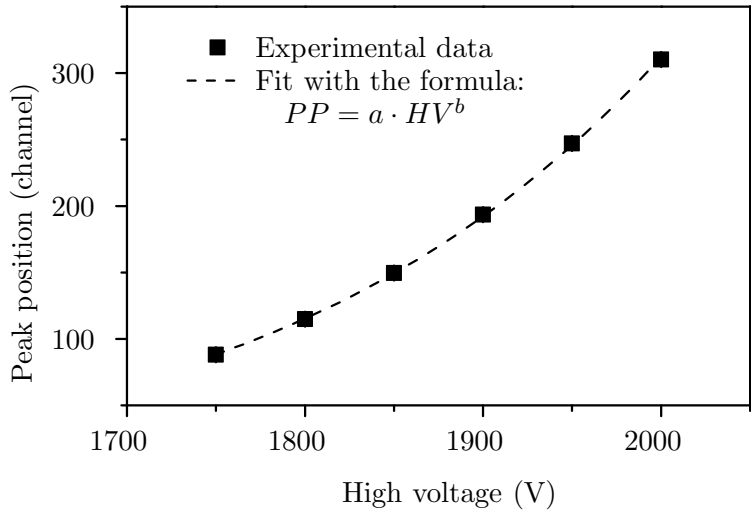

Figure 5.4: **Position of the peak in the background spectrum, measured at different high voltages.**

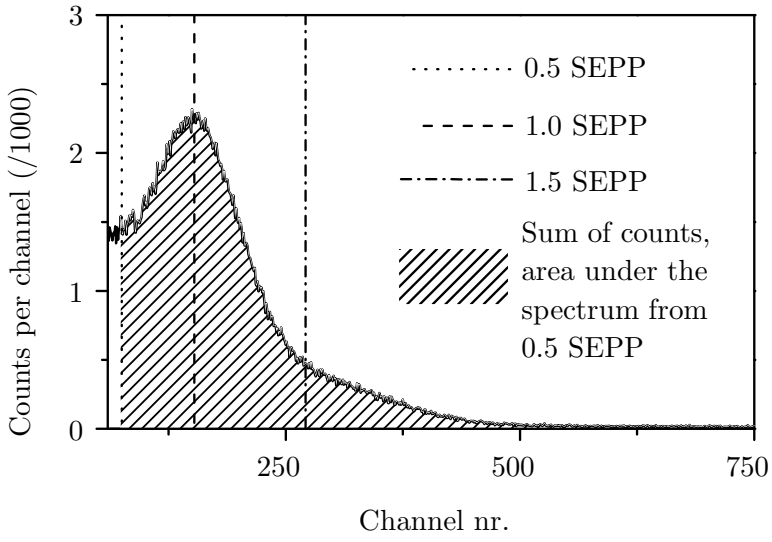

Figure 5.5: **Illustration of the spectrum summing.** For e.g. 0.5·SEPP, the counts were summed in the channels from the channel nearest to 0.5·SEPP (which is usually not an integer), up to the maximum channel. This is basically the area under that part of the spectrum (shaded area).

this value was taken as the beginning point to sum up the counts in the spectrum. As a graphical explanation, see Fig. 5.5. This way always the same portion of the spectrum was summed, regardless of the actual gain. Later, the summing range was constrained due to switch-on effects, see Section 5.2.5.

5.2.4 Stabilization of the detector temperature

The temperature of the PMT strongly influences the thermionic electron emission of the photocathode. The emission follows the Richardson law [7]:

$$J = AT^2 exp(-W_{th}/kT) \tag{5.4}$$

where J is the current density of electrons, A is a constant, W_{th} is the thermionic work function, T is the absolute temperature, and k is the Boltzmann constant.

To observe the aforementioned influence, the temperature of the PMT housing was monitored by means of a National Instruments USB-TC01 temperature sensor unit, which also recorded the measured values. The measuring head of the sensor unit is shown in Fig. 5.6. The resolution of the temperature sensor is 0.1°C.

The background signal of the PMT was measured in 10 minute intervals for one week, along with the temperature of the PMT housing, see Fig. 5.7. The count rate directly follows the temperature, which is not surprising, taking into account that without cooling the temperature of the PMT is mainly determined by its surroundings.

To overcome this instability of the background, a cooling device was constructed, using a commercially available cooling machine. The data of this machine is in Table 5.1.

The machine is shown in Fig. 5.8 a. By means of the front panel, a temperature can be set with 0.1°C precision. A plastic tube can be connected to the device, in which the coolant is circulated. After switch-on the machine starts to circulate the coolant, and regulates the temperature of it by means of a PID controller [37]. The plastic tube is twisted tightly around the outside of the setup (Fig. 5.8 b), except the legs of the setup, and the upper part of the sample chamber (to allow the opening of the sample chamber). Figure 5.9 shows the effect of the cooling on the background count rate of the PMT: as the cooling is switched on, the temperature and the count rate drop significantly. As the temperature is stabilized, the count rate is much more stable than before: from the data in Fig. 5.9, the standard deviation calculated from the first and last 50 measurements are 5.8 and 1.7 cps, respectively. As can be seen in Fig. 5.9, the cooling temperature was chosen to be 15°C. The reason is that at too low temperatures condensation starts, which is better to be avoided because of the high voltage.

It should be noted here that after the aforementioned experiments, an attempt to optically couple the PMT to the glass window resulted in higher (2-3 times the previous) and unstable (constantly drifitng) background, which did not settle also after removing the optical coupling element. The reason probably was insufficient insulation, which can easily cause unstable background [7]. The tube was exchanged with another PMT of the same type. This tube had even a better gain, which meant that the SEPP was at a higher channel number (see Fig. 5.10) at 1850 V supply voltage.

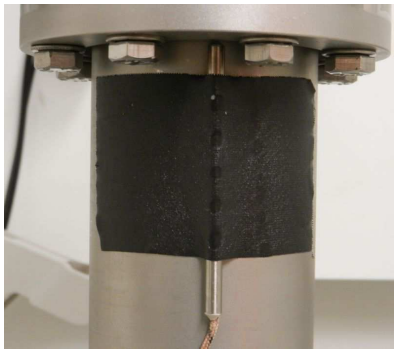

Figure 5.6: **The temperature sensor on the side of the PMT housing.**

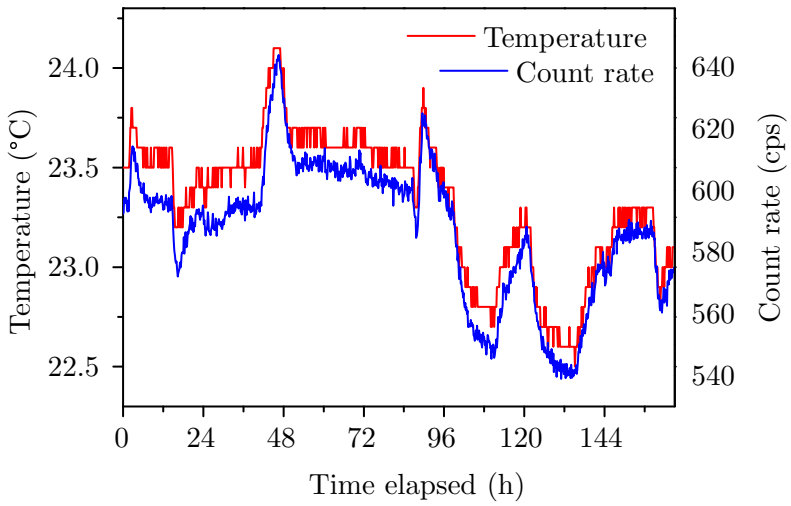

Figure 5.7: **The temperature of the PMT housing and the background count rate during one week.** The temperature was measured by means of the temperature sensor in Fig. 5.6

Table 5.1: **Properties of the "Oasis Three" cooling machine.** Data is from [36].

Property	Description/value
Cooling method	Peltier effect
Cooling power	300 W
Temperature stability	0.05°C
Cooling liquid	Distilled water/water-glycol mixture

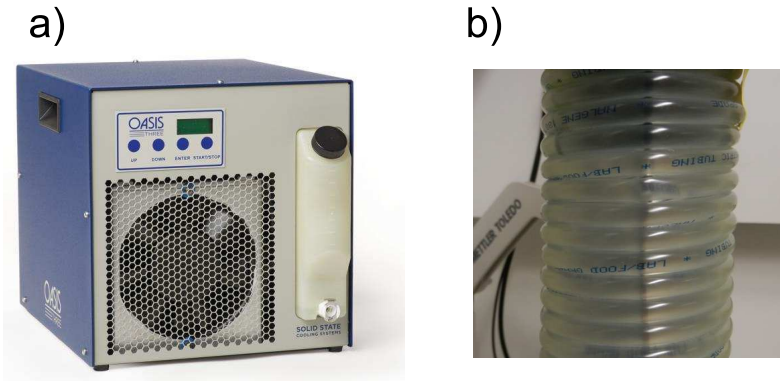

Figure 5.8: **The cooling machine (a) and the cooler tube around the PMT housing (b).** The temperature sensor (Fig. 5.6) is dimly visible under the tube.

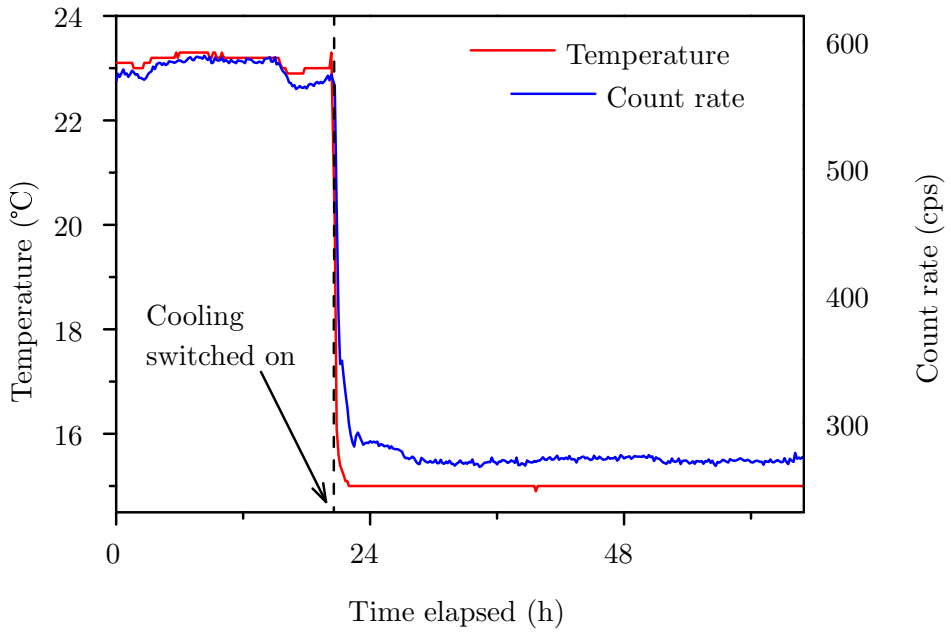

Figure 5.9: **The effect of cooling.** As the cooling machine is switched on, the background count rate drops significantly.

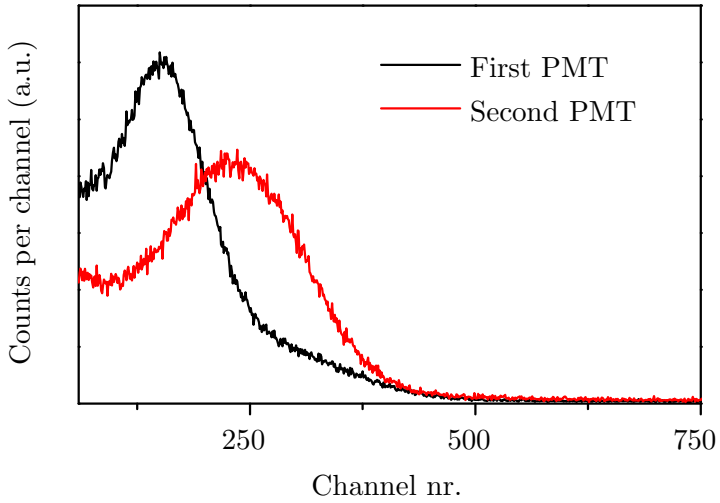

Figure 5.10: **Comparison of the background spectra of the first and second PMT.** Both spectra were measured with the same electronic settings as in Section 5.2.1, and at a supply voltage of 1850 V

5.2.5 Investigation of switch-on effects

This measurement aimed to investigate and eliminate the effects of the switch-on of the PMT. For this purpose the PMT was operated for several days to achieve a stable count rate, then the supply voltage was switched off overnight (see Fig. 5.11).

The next day, the sample chamber was opened for approximately one minute, then

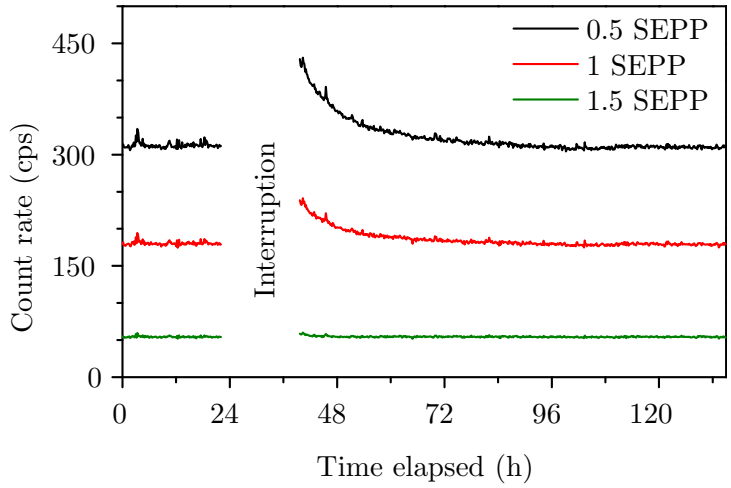

Figure 5.11: **Count rates before and after the interruption of the high voltage.** The various curves show count rates calculated from the sum of counts from three intervals: beginning at the channel at 0.5, 1 and 1.5 times the SEPP, respectively, and ending at the maximum channel (8191).

closed, and the supply voltage was restored. As is apparent from Fig. 5.11, the count rate, measured from $0.5 \cdot SEPP$, was much higher than before, and settled only several days after the interruption. This is the phenomenon already mentioned in Section 3.4.

Hereafter, only the spectrum part from the channel corresponding to $1.5 \cdot SEPP$ was summed to calculate the count rate (see also Fig. 5.5). This way, as it is apparent from Fig. 5.11, most of the switch-on effect is eliminated, since most of the SEP is excluded from the count rate calculation.

The count rates before and after the interruption, were the same: from 10 measurements at the beginning and end of the measurement in Fig. 5.5, the count rates were 53.9 ± 0.4 cps and 53.7 ± 0.5 cps, respectively, which means they match within error.

5.3 Calibration and investigation of reproducibility

5.3.1 Description of the measurement procedure

During the measurements in this chapter, if not mentioned otherwise, the water amount in the glass cup was always 3 ml.

The general measurement procedure was the following:

- The previous measurement ran until the signal was stable. This took less than 24 hours (see Fig. 5.12), depending on how much ambient light the PMT was exposed to during the previous sample change.
- The PMT supply voltage was switched off.
- The sample chamber was opened and the glass cup was taken out.
- Samples were taken to measure the tritium concentration in the water. Sample volume was 0.5 ml for distilled water, and 3 μl for tritiated water.
- If tritiated water with another concentration was about to be measured:
  - A given amount (V_{out}, in the range 0.5 to 1 ml) of water was taken out from the glass cup.
  - V_{out} plus the amount of the previously taken samples of water was filled to the remaining water.
  - The filled water was either concentrated tritiated water (ca. 9.4 GBq/ℓ) or distilled water (to increase or decrease the concentration, respectively).
- If a background was about to be measured:
  - The tritiated water was simply taken out with a pipette.
  - The glass cup, the scintillator and the scintillator holder wire were flushed with distilled water and dried with a paper towel.
  - The cup was filled with 3 ml distilled water.

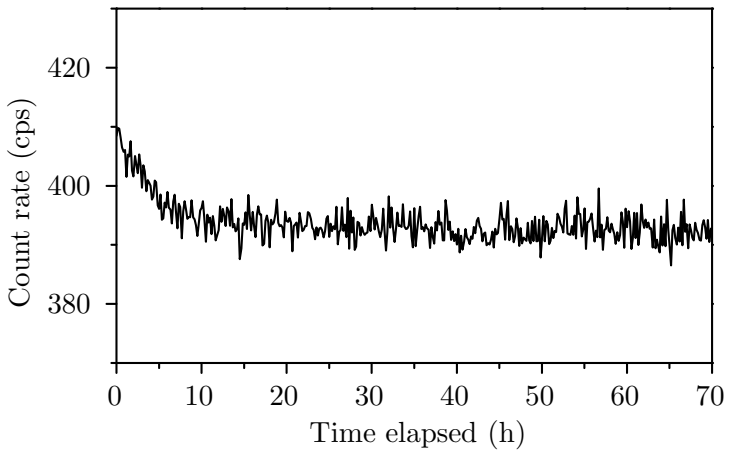

Figure 5.12: **Count date during a long HTO measurement.** The tritium concentration in the sample chamber was 9.03 ± 0.15 GBq/ℓ. The signal is considered to be stable from the 20^{th} hour.

  - The scintillator was put back on the holding wire, put into the glass cup, and pushed down into the water.

- The glass cup was put back into the sample chamber.
- The sample chamber was closed.
- The supply voltage of the PMT was restored.

The water samples were measured by means of a Perkin-Elmer Tri-Carb 2800TR type LSC machine. Measurement time was 1 minute, as quench indicator the "tSIE" value was used [38]. Distilled water without tritium was added to each sample, to keep the total sample volume 1 ml, since the machine was calibrated using standards containing 1 ml tritiated water.

The measurement result and the uncertainty, if not otherwise noted, were calculated following the procedure according to the "Evaluation of measurement data — Guide to the expression of uncertainty in measurement" [34], as follows:

- Several ($N \geq 3$) independent measurements of the same value were performed (e.g. several water samples were taken and measured, or the count rate was measured consecutively several times, etc.). The i-th measured value is denoted y_i.
- The average of the measured values was calculated, and taken as the estimate of the real value:

$$y = \frac{1}{N} \sum_{i=1}^{N} y_i \ , \tag{5.5}$$

- The standard uncertainty of the measurement is calculated as the standard deviation divided by $\sqrt{N}$:

$$u = \sqrt{\frac{1}{N(N-1)} \sum_{i=1}^{N} (y_i - y)^2} \tag{5.6}$$

- The expanded uncertainty was calculated with a coefficient k, for 90% confidence level, then the measurement result is given as:

$$Y = y \pm k \cdot u \tag{5.7}$$

  The value of k depends on the degrees of freedom, (ν, in case of the above procedure $\nu = N - 1$) and can be obtained from tables (e.g. from [34], Table G.2).

The measurement value given in the form of Eq. 5.7 represents the interval in which the real value of the measured value can be found with 90% probability. Hereafter, the term "significantly different values" is used in the meaning "the difference of the values is bigger than their expanded uncertainties together".

5.3.2 Experimental results

The background of the detector was first measured with empty sample chamber, and found to be 53.74 ± 0.48 cps. A new scintillator plate was put into the glass cup, and 3 ml of distilled water was added, to measure the background. In total, ten measurements were performed during the calibration series. The tritium concentration was first increased, then decreased, at the end increased again to see if the measurements were reproducible. The concentrations were not exactly repeated, but the obtained values were close to each other. The concentrations of the water during the various measurements are in Table 5.2.

The measurements denoted "DW" in Table 5.2 were performed with (in the beginning) practically tritium-free distilled water. In spite of this, substantial amount of tritium was measured in the water after opening the sample chamber. The used distilled water was separately measured with the LSC machine several times during the experiments, and found to have a concentration less than 1 kBq/ℓ, which is on the order of the detection limit of the LSC machine. Therefore the source of the contamination found in the "DW" measurements cannot be the distilled water (see also Section 5.3.3).

The count rates used for the calibration were calculated from the ten last count rate measurements, right before the switch-off of the PMT. The calibration line resulting from the measurements is shown in Fig. 5.13. The line in Fig. 5.13 shows a clear linear relationship between the tritium concentration and the count rate. The correlation coefficient of the measurement points is $R^2 = 0.9994$.
A linear fit, using X and Y errors for the fitting, gives the following equation:

$$CR = (47.67 \pm 0.72) \cdot c_A + (57.54 \pm 0.97) \ , \tag{5.8}$$

Table 5.2: **HTO concentrations and count rates during the calibration.** 3 samples were taken to measure each concentration (see text).

Measurement code	Activity concentration (c_A, GBq/ℓ)	Count rate (cps)
DW 1	$(8.35 \pm 0.06) \cdot 10^{-3}$	58.23 ± 0.516
TW 1	1.6 ± 0.1	131.93 ± 1.336
TW 2	4.2 ± 0.16	257.15 ± 1.222
TW 3	6.74 ± 0.07	379.31 ± 1.942
TW 4	4.6 ± 0.2	279.32 ± 1.244
TW 5	1.83 ± 0.04	144.79 ± 1.965
DW 2	$(1.23 \pm 0.03) \cdot 10^{-3}$	55.86 ± 1.270
TW 6	2.3 ± 0.2	196.38 ± 0.834
TW 7	4.8 ± 0.4	280.00 ± 0.978
DW 3	$(7.9 \pm 0.1) \cdot 10^{-3}$	57.95 ± 1.292

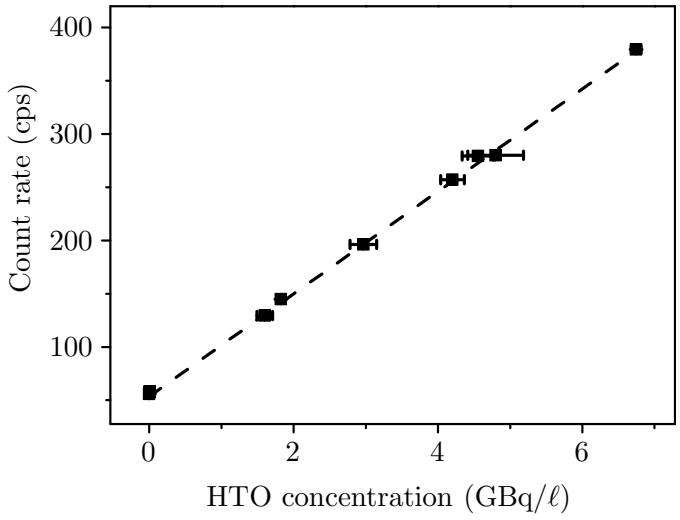

Figure 5.13: **Calibration line of the setup.** The data points are drawn with error bars, but these are in some cases comparable in size to the data points. The dashed line represents a linear fit, including X and Y errors (Eq. 5.8).

where CR is the measured count rate (cps), and c_A is the tritium concentration in GBq/ℓ. The uncertainties are the results of the fitting.

The count rates of the DW 1, DW 2, and DW 3 measurements are 58.23±0.52, 55.86±1.27, and 57.95±1.29 cps, respectively. The background values are all significantly bigger than the one measured with empty sample chamber, and the DW 2 measurement differs from the other two significantly.

To characterize the detector in terms of detecting real activity, the critical level and detection limit are calculated. The critical level of the count rate is defined as a count rate value for which the probability of a false positive measurement (declaring activity, without real activity present) is not larger than 5%. Assuming a Gaussian probability distribution of the measured count rate, with standard deviation σ_{BG} of the background (denoted BG), the critical level is (after [5], taking into account that in our measurements the background is not subtracted):

$$L_{crit} = BG + 1.645 \cdot \sigma_{BG} \ , \tag{5.9}$$

In our case one cannot speak about one background, since the measured background values differed from each other significantly. One solution is to use the background value obtained from the calibration equation, together with the one sigma error given by the fit, representing one standard deviation. With these values:

$$L_{crit} = 58.51 \text{ cps} \rightarrow c_{A,crit} = 0.020 \text{ GBq}/\ell.$$

Here $c_{A,crit}$ means the activity, which causes a count rate L_{crit} according to Eq. 5.8. An activity under this value produces a count rate which equals background with 95% probability.

The detection limit is defined as the activity which produces a count rate that is high enough that the probability of false negative readings (declaring no activity when activity is present) is less than 5%. This count rate is, according to [5]:

$$L_{det} = L_{crit} + 1.645\sigma_{CR} \tag{5.10}$$

where σ_{CR} is the standard deviation of the count rate at the detection limit. In our case, as a conservative assumption the biggest measured standard deviation of the DW measurements, 1.29 cps was used in place of σ_{CR}. This gives

$$L_{det} = 60.64 \text{ cps} \rightarrow c_{A,det} = 0.065 \text{ GBq}/\ell.$$

Another way to characterize the detection capabilities of the setup is to calculate the above values using the highest count rate from the DW measurements, its standard deviation, and again the highest measured standard deviation from the DW measurements as the measurement standard deviation. Then

$$L_{crit} = 59.08 \text{ cps} \rightarrow c_{A,crit} = 0.032 \text{ GBq}/\ell,$$

and

$$L_{det} = 61.21 \text{ cps} \rightarrow c_{A,det} = 0.077 \text{ GBq}/\ell.$$

The concentration values are again calculated with Eq. 5.8.

5.3.3 Discussion of the experimental results

The calibration has shown that the detection efficiency (slope in Eq. 5.8) of the setup is

$$\eta_{det} = 4.77 \cdot 10^{-8} \ \frac{\text{cps}}{\text{Bq}/\ell} \ ,$$

which is several orders of magnitude lower than those of the previous detectors mentioned in Section 3.6. The specific efficiency, given that the surface of the scintillator (F_{sci}) is 13.7 cm^2, turns out to be

$$\epsilon_{det} = 3.5 \cdot 10^{-9} \frac{\text{cps}}{\text{Bq}/\ell \cdot \text{cm}^2} \ ,$$

which is still orders of magnitude lower than the values obtained for the previous detectors.

Taking into account that the range of tritium β-electrons is on the order of micrometers, the geometry of the setup plays a minor role in determining the fraction of beta electrons reaching the scintillator. Therefore, the scintillation light collection of the setup is one possible reason for the lower efficiency. This explanation is plausible, since no light coupling was used in the present setup, and there are multiple glass-air border surfaces in the way of the scintillation light.

Another possible explanation is that the scintillator molecules on the surface of the scintillator got damaged by the radicals formed in water due to radiation [39]. Molecular damage can lead to a decrease in the scintillation yield and an increase of quenching [6]. These are also discussed in Chapter 7, in connection with the simulation of the detection process of the detector.

The close-to-one correlation coefficient and the closeness of the measurement points to the calibration line means that the measurements were reproducible. This implies that the non-reproducibility of the first measurements was mainly caused by the temperature influence on the background, and the changes of PMT gain.

As is mentioned, the used distilled water (DW measurements) was found to be contaminated, but this contamination was not present before the measurement with the setup. In the case of the DW 1 measurement, the source of contamination cannot be the scintillator, as prior to this measurement the scintillator was exchanged with a fresh one. The most probable source of contamination is therefore the glass cup.

The activity concentration of contaminated water was under the detection limit, but in spite of this, the measured count rates were significantly higher than the background measured with an empty sample chamber, even if we correct the count rates for the activity in the water with Eq. 5.8. One reason for this might be a memory effect, meaning that some tritiated water stays on the scintillator surface after rinsing with distilled water. However, the first background measured with distilled water was the highest of all, in spite of the fact that the scintillator was not used before. In Section 5.2.5 it was shown that after an interruption, the background count rate of the PMT itself returns to its original value. This means that it is less probable that the increase of the background of the PMT caused the higher count rates of the DW measurements, but it also cannot

be excluded, since a PMT is less stable if its supply voltage is switched on and off [7]. This topic will be discussed in more detail in Section 5.7.

5.4 Analysis of the pulse height spectrum

5.4.1 The fitting function

The fitting function for the pulse height spectrum of the PMT is constructed using the following model to describe the signal pulses:

1. The single electron events of the PMT produce a pulse height distribution which can be described with a Gaussian distribution.

2. The multiple electron events are many single electron events happening at the same time.

3. The multiplication processes of individual electrons do not disturb each other in a multiple electron event, each electron is multiplied as a single electron.

The first condition of the model is shown in Fig. 5.14, where a Gaussian curve is fitted onto the background spectrum of the PMT used in the experiments. The match of the Gaussian is satisfactory only above channel 160. Below this channel the spectrum is distorted by the unavoidable noise pulses [7], and the chi-square value of the fitted Gaussian was increasing if channels under 160 were included in the fit. Therefore, the fit is performed only from channel 160.

For the construction of the pulse height distribution of an n-electron pulse, the following is noted: if normalized to one, any pulse height distribution is a probability

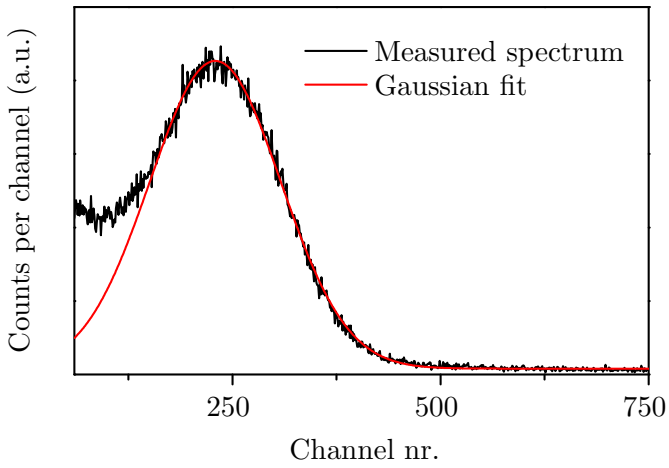

Figure 5.14: **Fitted Gaussian curve on the background spectrum of the PMT.** The fitting is restricted to the channel number region from 160 to 750 (see text).

distribution function (PDF) of the pulse heights, therefore the properties of PDFs are applicable (taken from [41]). Here we first use the property that the PDF of the sum of n random variables is the convolution of the individual PDFs. Then the convolution of n identical Gaussian distributions is another Gaussian distribution, with the mean

$$\mu_n = n \cdot \mu_1 \tag{5.11}$$

and standard deviation

$$\sigma_n = \sqrt{n} \cdot \sigma_1 \tag{5.12}$$

where μ_1 and σ_1 are the average and standard deviation of the original Gaussian distribution.

The pulse height distribution of an n-electron pulse is then a Gaussian distribution, because it is composed of independent single-electron pulses, the PDF of which is Gaussian.

Based on the above, the model function for the PMT pulse height distribution is the sum of Gaussian functions:

$$C(CH) = \sum_{n=1}^{M} \frac{C_n}{\sqrt{2\pi n} \cdot \sigma_{SEP}} \cdot exp\left[-\frac{1}{2}\left(\frac{CH - PP_n}{\sqrt{n} \cdot \sigma_{SEP}}\right)^2\right] , \tag{5.13}$$

where $C(CH)$ is the number of counts in the CH-th channel of the ADC, n means the number of photoelectrons in an event, C_n is the number of events with n photoelectrons, M is the maximum number of photoelectrons in an event, PP_n is the center of the n-th Gaussian (the peak position), and σ_{SEP} is the standard deviation of the single electron peak. An event with n photoelectrons is hereafter called an n electron event for simplicity. The function presented here, as it is shown in the next section, is a good approximation of the experimentally measured pulse height distribution of pulses above channel 160.

5.4.2 Analysis of the fitted spectra

The spectrum analysis required the PMT to be in steady state operation, so that the gain does not change and the single electron counts also settle to a stable value. As seen from Fig. 5.11, it is achieved after about two days. Therefore the background (with an empty sample chamber) and the spectrum of tritiated water (concentration: 5.86 ± 0.07 GBq/ℓ) was measured for more than two days. From the end of these measurement series (after more than two days of measurement), 100 measurements were selected, where the count rate (calculated from $0.5 \cdot SEPP$) was not drifting anymore, and the relative standard deviation of the SEPP was less than 0.5%. The SEPP and count rate values versus measurement time are plotted in Fig. 5.15. The spectra of each of the 100 measurements were summed for each channel, beginning at channel 160. The lower channels were omitted, because they contained also the noise mentioned in the previous section. The count rate for each channel were calculated with the total livetime of the measurements, to correct for deadtime. At the end, the counts were recalculated

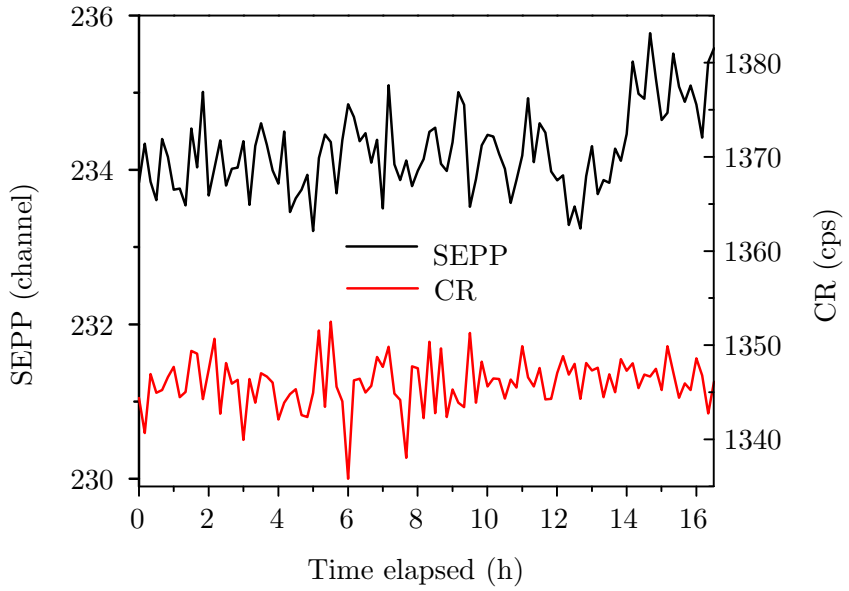

Figure 5.15: **Single electron peak position and count rate of a stable measurement.** The sample chamber contained tritiated water with a concentration of 5.86 ± 0.07 GBq/ℓ.

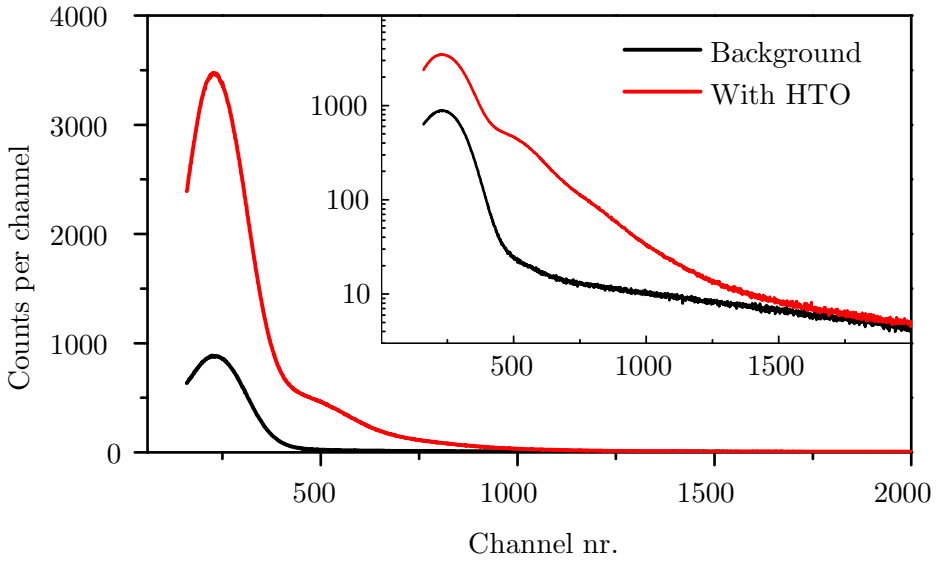

Figure 5.16: **Background, and spectrum with HTO.** The inset shows the same data in semi-logarithmic scale. Above channel 2000 the HTO spectrum is the same as the background.

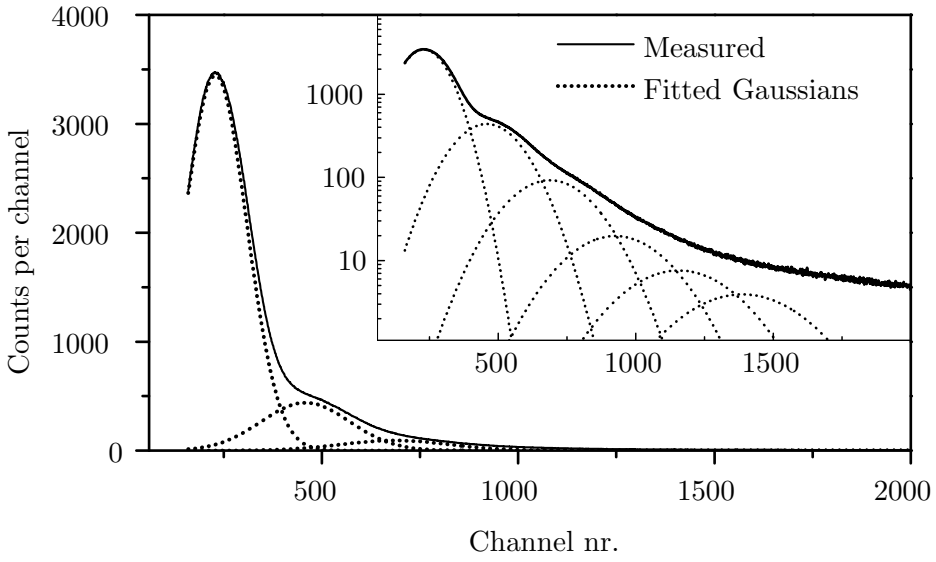

Figure 5.17: **The measured HTO spectrum and the first six fitted Gaussian curves.** The measured spectrum is the same as in Fig. 5.16.

for 10 minute measurement time (hence excluding deadtime) for each channel. The obtained spectra are presented in Fig. 5.16.

The spectrum obtained with tritiated water shows a difference only for channel numbers less than 1700. Since the goal was to determine the spectrum of the tritiated water, the data up to channel 2000 was used for fitting Eq. 5.13. The number of fitted Gaussians was $M = 9$, to cover, besides the actual peaks from tritiated water, the background part of the spectrum up to channel 2000. The fit was performed by using the statistical errors of the counts as weighing factors. The result of the fit for the data obtained with tritiated water is illustrated in Fig. 5.17. The fit resulted in a reduced chi-square value of 3.58 and 3.92, for the background and for the HTO measurement, respectively. The bigger-than-one reduced chi-square value means that the differences between the fitted and measured spectra are bigger than the statistical uncertainties. On the other hand, the adjusted R^2 values are 0.9995 and 0.9999 for the background and HTO measurements, respectively, where the close-to-one value indicates that the fitted function follows the experimental data closely.

The obtained counts (the areas of the Gaussians) for 1, 2, etc. electron events of the background were then subtracted from those of the tritiated water measurement, and the count rates were calculated:

$$CR(n) = \frac{S_{HTO}(n) - BG(n)}{t_m} \tag{5.14}$$

where $S_{HTO}(n)$ and $BG(n)$ are the number of counts of the n-electron events of the HTO and background measurements, respectively, and t_m is the measurement time (600 s in our case).

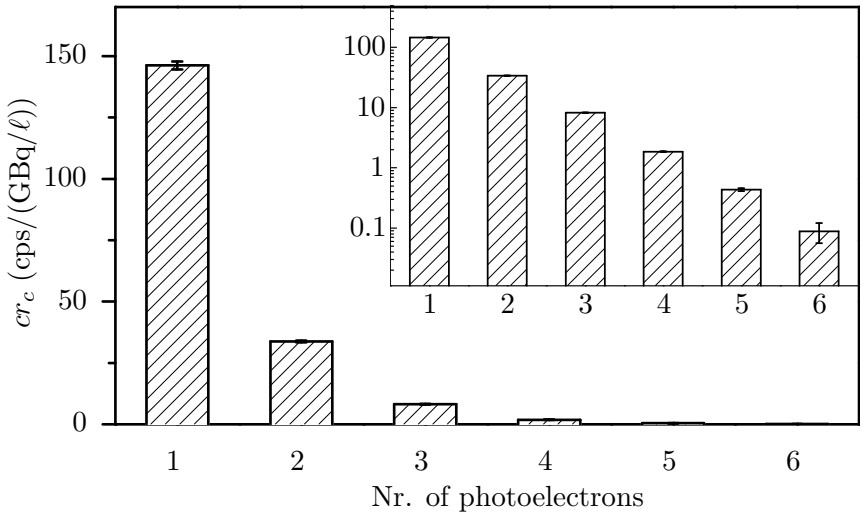

Figure 5.18: **Spectrum of the number of photoelectrons.** In the inset the same data with a semi-logarithmic scale.

The resulting electron number spectrum is shown in Fig. 5.18. For a better comparison of the various spectra with each other and the simulation (Chapter 7), the count rates of the 1, 2, etc. electron events were divided with the activity concentration in the detector:

$$cr_c(n) = \frac{CR(n)}{c_A} \tag{5.15}$$

where cr is the normalized count rate of the n-electron events, and c_A is the activity concentration in the sample chamber in GBq/ℓ. The majority of events (73.7%) are single electron events. The maximum number of electrons per event which are above background, is 6, but the relative uncertainty in the number of such events is 60.5% (at 90% confidence level, statistical uncertainties). Considering that the SEPP is "channel" 231.27 in the HTO spectrum, the seven-electron peak would be at "channel" 1618.9, where the tritium spectrum blends into the background. The number of events in the tritium spectrum with 7 or more electrons is therefore considered negligible compared to the rest of the spectrum.

Since the SEP dominates the spectrum, the spectrum summing used to eliminate the switch-on effects actually lowers sensitivity. If the whole spectrum could be used, the sensitivity would be

$$\eta_{det} = 1.91 \cdot 10^{-7} \ \frac{\text{cps}}{\text{Bq}/\ell} \ ,$$

yielding a specific sensitivity of

$$\epsilon_{det} = 1.39 \cdot 10^{-8} \ \frac{\text{cps}}{\text{Bq}/\ell \cdot \text{cm}^2} \ .$$

These value were calculated from the sum of the counts (for 10 minutes) in the spectrum plotted in Fig. 5.18. These "recalculated" sensitivity values are still orders of magnitude

lower than those of earlier works (see Section 3.6).

We would like to estimate the theoretical average number of photons from the scintillator, to compare them with the experimentally obtained spectrum. Eq. 3.12, together with the values of the $B(E_0)$ function can be used to calculate the theoretical number of photons. Based on $S_p = 9600$ photons/MeV (Section 4.2.1), for $E_0 = 5.7$ keV, which is the average β-electron energy of tritium, the average number of photons is 32. The maximum number of photons (on average) for a 18.6 keV electron would be 135. Taking into account the quantum efficiency of the PMT, which is 26.5% at 425 nm (wavelength of maximal emission of the scintillation light), the average number of photoelectrons in the aforementioned cases would be about 8.48 and 35.78, respectively.

In the experiment the average number of detected photons is 1.3 (weighted average, weighted with the relative frequency of the 1, 2, etc. electron events), and the maximum number of detected photons is 6. The source of this huge difference can be the energy loss of tritium β-electrons in the water, which is not taken into account here, in addition to the reasons mentioned in Section 5.3.3. A detailed discussion is only possible if the processes are simulated in detail, and this is presented in Chapter 7.

5.5 Investigation of the influence of sample volume

5.5.1 Description of the measurement procedure

In this measurement series only one tritiated water concentration was used, the first water volume was 3 ml. The procedure was as follows:

- The count rate and concentration were measured as described in Section 5.3.
- The water volume was increased, or in the second part of the series decreased, by adding/taking out some amount of the same tritiated water

The concentration measurements during the whole series did not show any difference within the experimental error. The concentration of the water was 5.86 ± 0.07 GBq/ℓ.

5.5.2 Experimental results

The measured count rates are plotted against the water volume in Fig. 5.19. The results show a slight dependence of the count rate on the water volume. However, the measurements with 6 and 12 ml water show significant deviation between the first (increasing amount) and the second (decreasing amount) measurement.

The measurements with 3 ml and 9 ml water were long enough, so that the count rates sufficiently stabilized (see Section 5.4.2) at the end that the spectra of these measurements could be compared. The photoelectron-number spectra of the measurements are calculated as in the previous chapter, and the count rates are plotted in Fig. 5.20. The graph shows that the number of single-electron events have increased, and the rest of the spectrum has decreased when the water amount was increased. The total count rate has also increased slightly, despite the same concentration of the water, from 1116 ± 1 cps

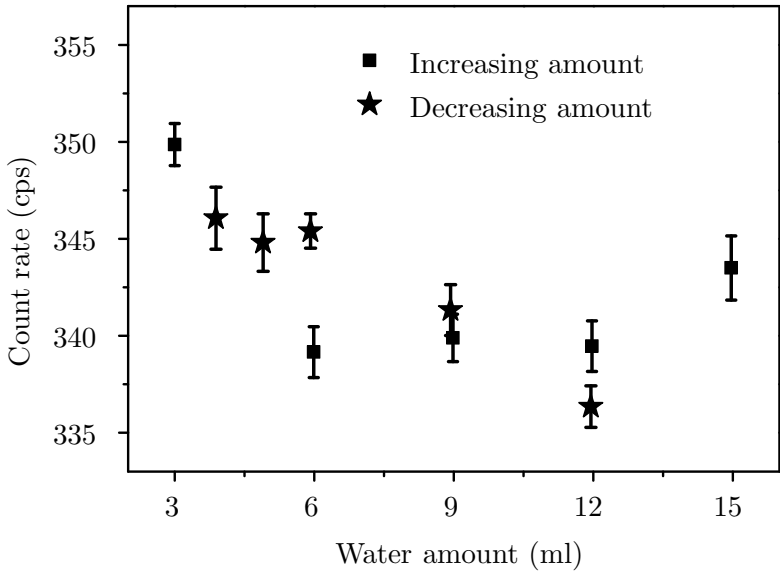

Figure 5.19: **Count rate versus the water amount in the sample chamber.** The tritium concentration was the same during the whole series: 5.86 ± 0.07 GBq/ℓ.

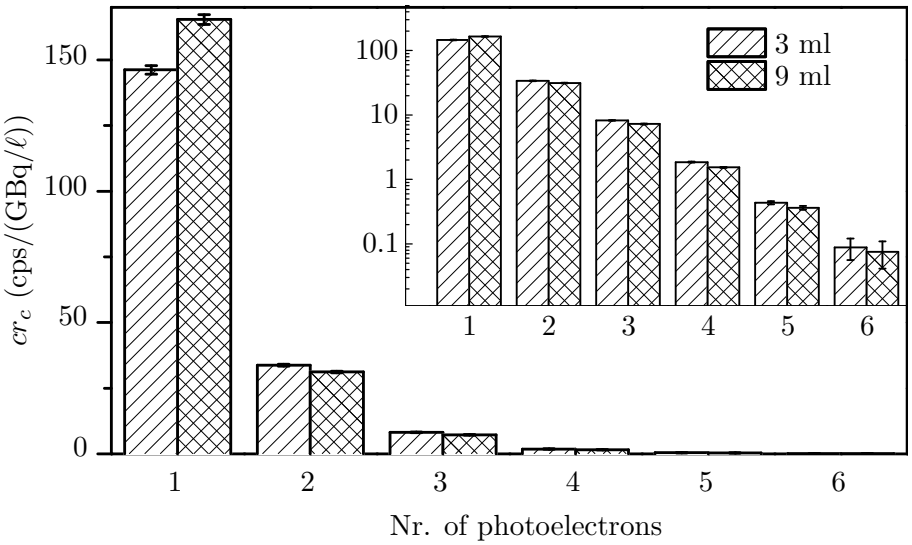

Figure 5.20: **Electron number spectra from two measurements with different water amounts in the sample chamber.** The water amount was the only difference between the two measurements.

to 1205 ± 1 cps. This means that the single-electron events increased more than the multiple-electron events decreased.

5.5.3 Discussion of the experimental results

As the spectrum analysis showed, the increase of sample volume caused the decrease of multiple-electron events, which is the reason of the negative effect observed in the count rate, since the count rate is calculated from that part of the spectrum, which consists mainly of multiple-electron events. This shift of the spectrum can be due to an optical effect: Those scintillation photons that are reflected back from the top of the water due to total internal reflexion have to travel a longer path until they reach the detector. During a longer path they are reflected more times on the aluminum cup walls, which increases the probability of absorption.

The increase of the single electron count rate suggests that the bremsstrahlung photons might have a slight influence on the spectrum, as mentioned in Section 5.1, because they have longer penetration depth than electrons. Indeed, the count rate of bremsstrahlung depends on the amount of water in a BIXS detector [11], [13]. The fact that only the single-electron events increased in the spectrum means that the bremsstrahlung deposits low amount of energy in the scintillator. The reasons for this can be:

- The photoelectric effect has a low probability in the scintillator because of the low atomic number (low density of electrons per cm^3), see Eq. 3.4.
- The maximum transferable energy to the electrons in the scintillator via Compton scattering is (from Eq. 3.5 for $\theta = \pi$) 1.26 keV for maximum β-electron energy, and 125.6 eV for average β-electron energy. This corresponds to 2.25 and 0.2 photons on average, respectively (calculated as in Section 5.4.2). The latter means that practically no optical photon is produced by such low energy electrons.

However, the above photon numbers are the maximum possible values and more than $^2/_3{}^{rd}$ of the photons are not detected due to the quantum efficiency of the PMT alone (not to mention losses in the detector cavity). This makes it unlikely that the bremsstrahlung photons had an influence on the spectrum. This topic is further discussed in Section 7.3.3.

5.6 Investigation of the influence of the number of scintillator plates

5.6.1 Description of the measurement procedure

The effect of the size of the surface of the scintillator was tested using a "scintillator tower" (Fig. 5.21). This was built up from five scintillator plates, 29 mm diameter each (same as the ones in the previous sections). The plates were held together with stainless steel wires bent into a U shape with a flat bottom. The distance between the plates was kept constant by means of 5x5x0.5 mm sized scintillator pieces. A thin plastic tube was used as a handle.

Figure 5.21: **The "scintillator tower".** The scintillator plates are the same size as the one used in the previous measurements, held together by stainless steel wires bent into a U shape with a flat bottom.

In order to avoid bubbles trapped between the scintillator plates, as the "tower" was lowered into the water in the cup, the latter had to be held about 45° to the vertical. This way the air between the plates could escape more easily. For the same reason, the water amount had to be enough so that the water level was 5 mm above the highest scintillator, otherwise the hydrostatic pressure of the water was not enough to push out the bubbles from in between the plates. This meant that a water volume of 6.9 to 12 ml, depending on the number of plates, was used.

The whole tower with five plates was measured first, then the plates were taken off one by one. The measurement procedure was as follows:

- The count rate and the concentration was measured as described in Section 5.3.
- The "scintillator tower" was taken out from the water, and the glass cup was emptied.
- One plate was taken off from the tower.
- The appropriate amount of water was added to the glass cup.
- The "tower" was lowered into the water and a new measurement was started.

The concentration of the water was 6.59 ± 0.06 GBq/ℓ, and it did not change during the measurement series.

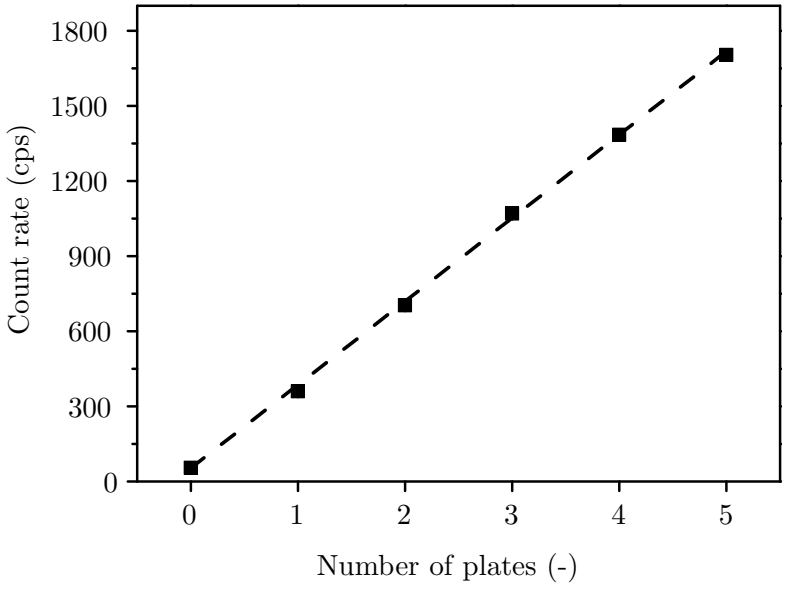

Figure 5.22: **Count rate versus the number of scintillator plates.**

5.6.2 Experimental results and discussion

The measured count rates versus the number of scintillator plates is shown in Fig. 5.22.

The graph shows a linear dependence. The line drawn in the graph shows a linear fit, with the equation:

$$CR = (333.10 \pm 0.20) \cdot N_{plates} + (53.09 \pm 0.30) \tag{5.16}$$

where N_{plates} is the number of plates in the sample chamber, CR is in cps. The fit is made considering Y errors only. The Y errors were the expanded uncertainties of the measured count rates. The relative uncertainties of the fitted slope and intercept are 0.06% and 0.57%, respectively, which means that a linear function satisfactorily describes the relationship between the number of plates and count rate.

The measurements with 1 and 3 scintillator plates were long enough for spectrum stabilization. The obtained spectra are in Fig. 5.23. The graph shows that the addition of two plates changed the relative spectrum, but only slightly. The relative occurrence of single, to quadruple electron events has increased, the rest of the spectrum did not change significantly. The linearity with respect to the number of plates means that the count rate is directly proportional to the surface of the scintillator, and the optical properties of the system did not change significantly due to the change in the number of scintillator plates. The reason for the improvement of the spectrum can be that the additional plates acted as partially reflecting surfaces because of the high refractive index of the scintillator material.

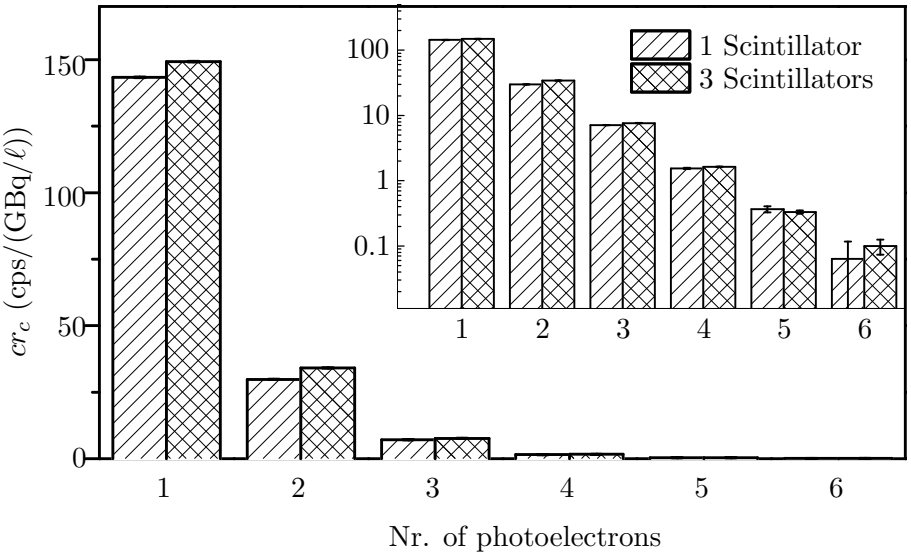

Figure 5.23: **Comparison of the electron number spectrum obtained with 1 and 3 scintillator plates.**

5.7 The effect of tritiated water on the aluminum cup and the scintillator

After the first measurement, the inner surface of the aluminum cup, which was originally polished, was covered with small grey dots (Fig. 5.24). This was probably oxidation of the aluminum surface by the water [23], which is common even in case of not tritiated water. The cup was not exchanged, since the same would have happened with another aluminum surface, and the coverage with aluminum oxide actually protects the surface of aluminum from further damage. The graying of the surface caused a decrease in reflectance of the cup, but the graying did not change significantly with time, as visually observed. Furthermore, the measurement with 9 ml water was repeated 8 days later, and the spectrum was determined. This spectrum, together with that of the first measurement are shown in Fig. 5.25. As is apparent, the two spectra are essentially the same (except the SEP), which suggests that the reflectance of the aluminum cup did not change enough to change the spectrum in 8 days.

After the experiments, the surface of the scintillator was examined and found to be cracked (Fig. 5.26). One reason for the cracking can be the oxidizing effect of the radicals in the water due to radiation, the other can be radiation itself [5]. The plastic scintillator is quite sensitive: The manufacturer advises to take off the protecting foil from the scintillator immediately before use [15], to avoid damaging the material. Unfortunately in our case the contact with the water is unavoidable. The damage to the surface could decrease the efficiency of the scintillator [5].

After the experiments described in this chapter, the scintillators were each flushed

Figure 5.24: **The oxidized inner surface of the aluminum cup.**

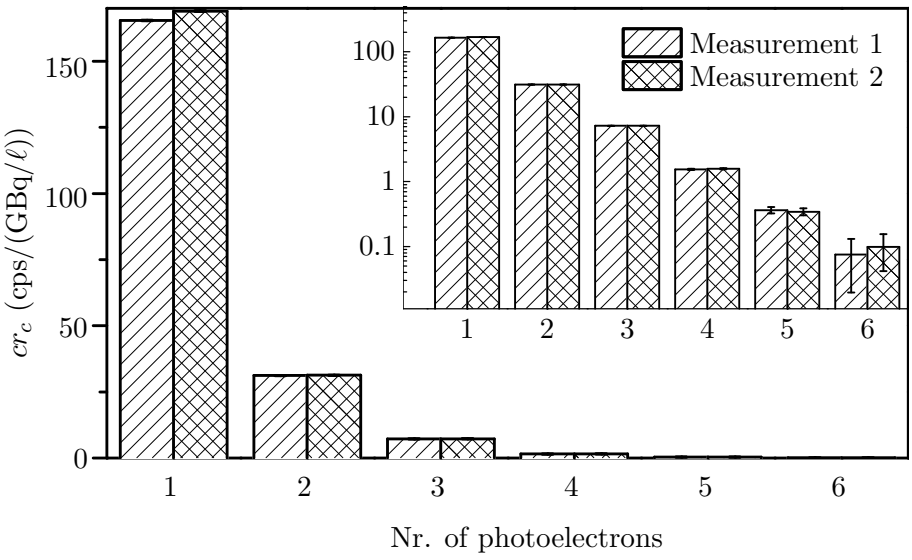

Figure 5.25: **Comparison of two measurements 8 days apart.** The conditions of the two measurements are otherwise identical: 9 ml of tritiated water, concentration 5.86 ± 0.07 GBq/ℓ.

Figure 5.26: **Typical surface cracking of the scintillator.**

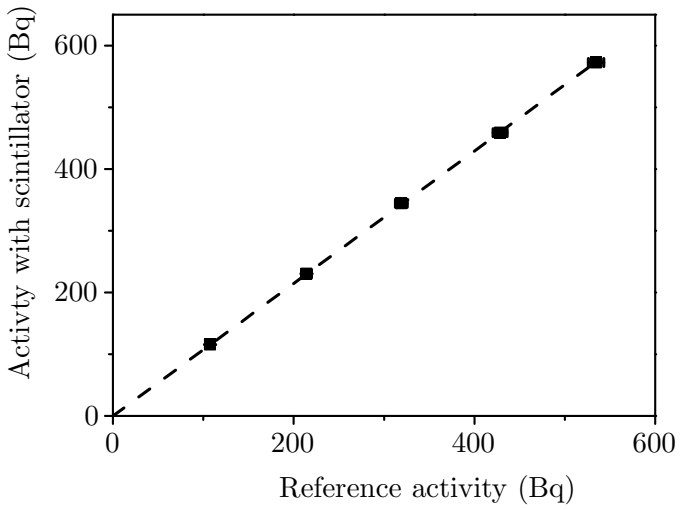

Figure 5.27: **Calibration of the LSC machine to measure the activity in the plastic scintillator.** The reference values are the measurement results without scintillator material, but the same amount of tritiated water in the LSC cocktail, as in the samples with scintillator dissolved in the cocktail. The dashed line shows the result of the fit with $y = m \cdot x$.

Table 5.3: **LSC measurements of the scintillators used in the setup.** The scintillator plates had the same size, and spent increasing amount of time in tritiated water.

Scintillator	Activity (Bq)
Scintillator tower 1	1.57 ± 0.04
Scintillator tower 2	2.10 ± 0.05
Scintillator tower 3	4.76 ± 0.09
Scintillator tower 4	6.41 ± 0.13
Scintillator tower 5	6.13 ± 0.04
Scintillator for calibration	8.15 ± 0.09

with distilled water 3 times, dried with paper, put into separate plastic bags and stored for further examination. At the end of all the experiments described in this work all the scintillators were cut up into pieces and dissolved in 15 ml of Instagel Plus scintillation cocktail, then their activity measured in the same LSC machine, which was used for the water samples. The same measurement settings were used, as for the water samples, measurement time was 20 minutes.

In order to see if the LSC machine measures the plastic scintillator samples differently from the usual samples, a comparison measurement was done: Two series of five LSC samples, with 1-5 μl of tritiated water added to 15 ml of Instagel Plus was measured. The concentration of the tritiated water was $1.07 \cdot 10^8$ Bq/ℓ. One series was the reference, and in the bottles of the other series 15x15x0.5 mm sized BC-408 scintillator plates were dissolved. The results are plotted in Fig. 5.27. A line with the equation $y = m \cdot x$ was fitted to the data, with the result $m = 1.073$. The fit was made without considering error bars. The correlation coefficient of the line was 0.99999. The activities of the scintillator plates were measured and corrected by means of m, then corrected for decay (because of delayed measurement), and are presented in Table 5.3.

The table shows that tritium (or tritiated water) was bonded on the surface (or in the bulk material) of the scintillators. The measured activity generally increased with time spent in the tritiated water, except for the last plate of the scintillator tower. This can be the result of the slow diffusion of tritium into the bulk of the scintillator.
The activity in the scintillators showed only a moderate value compared to the total activity present in the sample chamber during measurements (the latter is in the range of MBq). However, considering that the background of the detector is 53.74 ± 0.48 cps, the activity here can cause a count rate significant enough to be detected. This can partly explain the memory effect mentioned in Section 5.3.3.

5.8 Summary of the characterization

The experimental setup described in Chapter 4 was optimized and characterized. In the present configuration, to have reproducible measurements, the temperature of the PMT has to be stabilized to ±0.1°C, and the gain drift after switch-on has to be compensated.

Furthermore, to have a measurement result after one day, the single electron peak of the PMT has to be excluded from the spectrum summing.

The sensitivity of the detector is some orders of magnitude lower than detectors in previous works. This is most probably the consequence of the absence of a light coupling medium. The detection limit is consequently high compared to the target value set in Section 2.2.

The background count rate of the detector changed during the measurements, which points to a memory effect.

The spectrum analysis showed that the PMT detects mainly single-photoelectron events. This is in strong contrast with the number of photons which theoretically leave the scintillator. Besides the detection efficiency of the PMT and the energy loss of the β-electrons in the water, the reason for the aforementioned spectrum can be the poor light collection of the setup and the degradation of the scintillator in the tritiated water. This topic is further discussed in Chapter 7.

The amount of water in the sample chamber has an effect on the spectrum: The number of single electron events increase relative to the multiple-electron events, and the total count rate increases about 8%. This means that the number of single electron events is increasing more than the other events decrease. The shifting of the spectrum is probably due to the change in light collection of the setup. The source of the extra single electron events is unclear. Bremsstrahlung induced in the water is unlikely to cause significant count rate increase.

The increase of the number of the scintillator plates increases the count rate linearly. This is the consequence of the short range of tritium β-electrons. More scintillator plates shift the spectrum slightly towards multiple electron events, which can be the consequence of reflection of scintillation photons from the scintillator plates at the top of the "scintillator tower", which can improve light collection.

The tritiated water has damaged the reflecting aluminum cup and the scintillator. This could cause a decrease in light collection and scintillator efficiency. Additionally, a measurable amount (<10 Bq) of tritium was measured in the scintillator plates after using them in the experiments, which can can partly explain the memory effect.

In order to avoid the switch-on effects, and increase sensitivity, after these measurement series the setup was improved. The improvements and the results with the improved setup are presented in the next chapter.

6 Improvement and additional measurements with the experimental setup

This chapter describes the modifications made on the experimental setup in order to exclude the count rate and gain changes due to switching on the PMT. After these modifications the improved setup was tested in terms of background stability and sensitivity with a scintillator plate parallel to the PMT window (hereinafter referred to as parallel scintillator). The design of the sample chamber allowed the exchange of the sample chamber glass, and the testing of a scintillator arrangement, where the scintillator is perpendicular to the PMT window (hereinafter referred to as perpendicular scintillator).

6.1 Description of the new components

6.1.1 The new photomultiplier

As a new photomultiplier, the type 9813B, from Electron Tube Enterprises was chosen. This tube has 12 dynodes, which means a higher PMT gain, reducing the necessary external signal amplification. The main characteristics of this tube are included in Table 6.1.

The tube was operated with a voltage divider, which was designed for positive high voltage. The big advantage of positive high voltage is that the photocathode, together with the envelope of the PMT can be on ground potential, eliminating the possibility of

Table 6.1: **Properties of the 9813B photomultiplier.** Data is from [45].

Property	Description/value
Window material	Borosilicate
Refr. index	1.49
Photocathode	Bi-alkali
Spectral range	290-630 nm
Maximum sensitivity approx. at	350 nm
Quantum efficiency at 350 nm	30%
Typical supply voltage for nominal sens.	2100 V
Gain at nominal sensitivity	$7 \cdot 10^7$
Background noise (typ.)	300 cps

arching or leakage current between the PMT and the outer housing. The dark current of such a PMT also stabilizes more quickly after switch-on [7].

During the experiments described in this chapter, the PMT was operated with a supply voltage of 2050 V because, according to the test ticket of the tube, it reached nominal sensitivity at this value. Due to the high gain, a 100x amplification was enough, to see the single electron peak in the ADC (see Fig. 6.1). All other settings were the same as those used in Chapter 5.

6.1.2 The new sample chamber and the light-shutter valve

The purpose of the new sample chamber was the following:

- Eliminate the glass window between the sample chamber glass and the PMT for better light collection (fewer glass-air surface, less total internal reflexion).
- Make it possible to exchange the sample chamber glass without modifying other parts.
- Safer and easier handling of the sample chamber glass, by making the top part of the setup separable, with the sample chamber still closed.

The new sample chamber is custom made, but utilizes industrial standard KF flanges and KF O-rings for sealing the parts. It is shown in Fig. 6.2 a). The possibility to exchange the sample chamber glass allows the usage of a glass, in which the scintillator stays perpendicular to the PMT window. This other glass is shown in Fig. 6.2 b).

The PMT was intended to be used in continuous operation, which meant that for sample change and other procedures the PMT had to be protected from ambient light. For this purpose a sliding valve (type 5GVM-63CF-MV-S from VACOM) is built into the setup (Fig. 6.3 a)). The sliding valve consists of two CF-63 flanges, and a mechanism that slides a metal plate between the flanges when the valve is closed. The valve is built in such a way that the metal plate provides a light and vacuum tight seal between the two CF flanges.

The scintillator was the same material as the one used in the previous experiments. The scintillator plate for the sample chamber glass presented in Fig. 6.2 a) was circular, 38 mm in diameter, and 0.5 mm thick. The scintillator for the other sample chamber glass was a rectangular one, with sizes 9x59x0.5 mm.

As it turned out during the initial tests, the cooling (as shown in Fig. 6.3 b)) is only sufficient, if the sample chamber is covered with insulation foam from the top. Therefore a “cap” was made from insulating foam material. The rest of the setup is also covered with this foam, as is visible in Fig. 6.3 c). A new temperature sensor was mounted onto the KF-CF flange, and this was used instead of the one on the side of the setup used earlier (Fig. 6.3 b)). The reason for this was that the observed background changes (see Section 6.2) were not correlated with the temperature of the side of the setup.

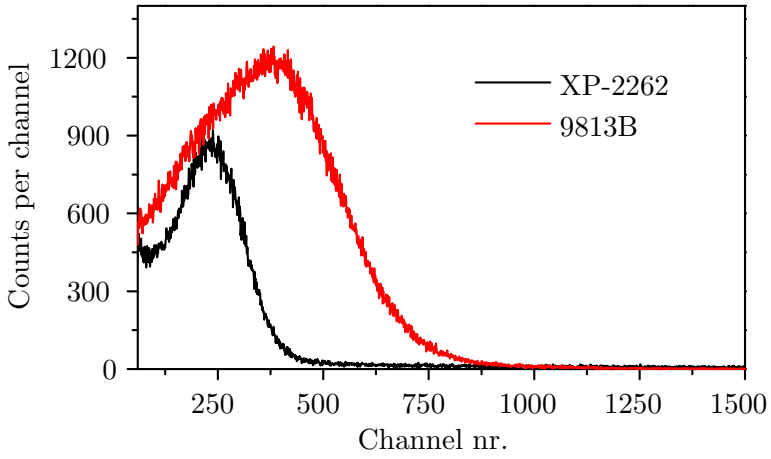

Figure 6.1: **Background spectra of the XP-2262 and the 9813B PMT-s.** The supply voltages are 1850 V and 2050 V, the amplifications are 1250x and 100x for the two PMT-s, respectively. Other settings were the same as in Chapter 5.

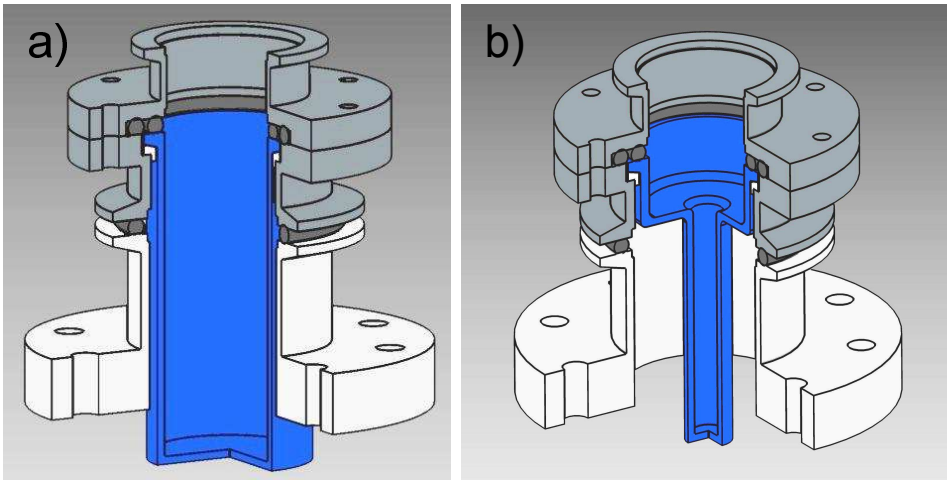

Figure 6.2: **Three-quarter-section views of the new sample chamber.** The dark gray part is separable from the bottom part, together with the blue colored glass part. The light gray part (KF-CF flange) serves as the connection to the rest of the setup. a) with glass part for parallel scintillator; b) with glass part for perpendicular scintillator.

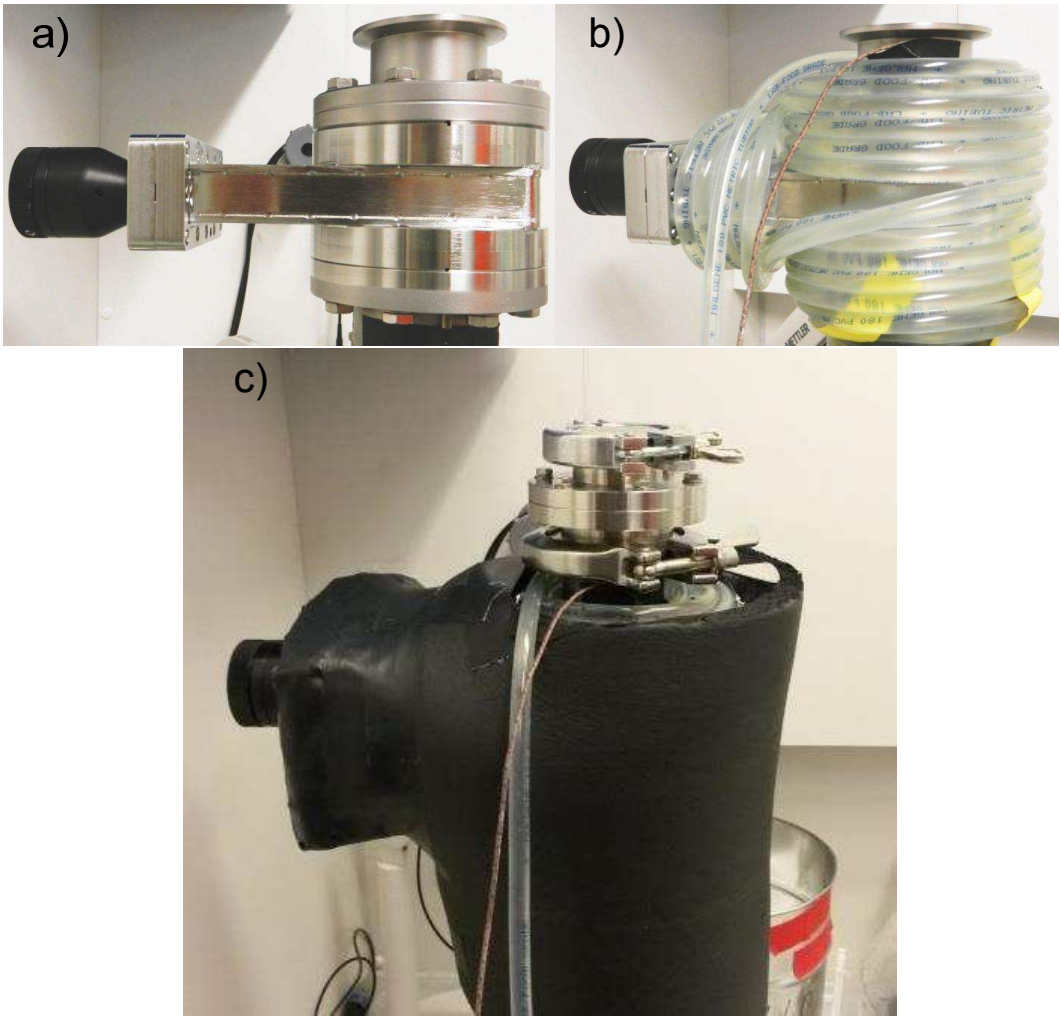

Figure 6.3: **Modifications on the setup.** a) The light-shutter valve on top of the PMT housing. On top is the KF-CF flange of the new sample chamber is visible; b) The cooling tube is wound around the valve and the KF-CF flange of the new sample chamber. A new temperature sensor is mounted onto the under-flange (brown wire); c) The whole setup is surrounded with a heat insulating foam, and the new sample chamber is placed and secured on top of it.

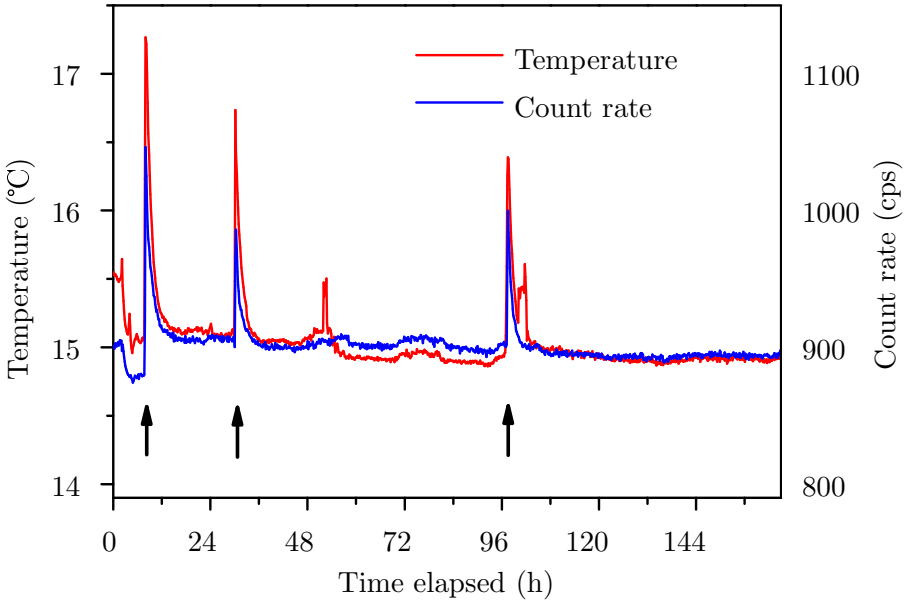

Figure 6.4: **Temperature of the top of the setup and background count rate of the PMT.** The temperature values are averages of 600 individual values during each count rate measurement. The black arrows show the time of opening of the light shutter valve.

6.2 Measurement of long term stability of the background signal

The goal of the first measurement series was to observe the background signal of the detector. Since no change of the SEPP was expected, the total count rates mentioned in this chapter are all calculated by summing up the counts in all ADC channels, and dividing with the livetime of the electronics.

After stabilization of the count rate, to test the behavior of the detector during sample change, the following actions were performed:

- The sliding valve was closed.
- The sample chamber was taken off the setup for 1-5 minutes.
- The sample chamber was remounted.
- The sliding valve was opened.

The above procedure was repeated several times, to check if the background count rate of the detector is stable. The result of these measurements is shown in Fig. 6.4. As is visible in Fig. 6.4, the demounting and mounting of the sample chamber has an effect on the count rate of the detector. The switch-on effects are eliminated by the usage of the

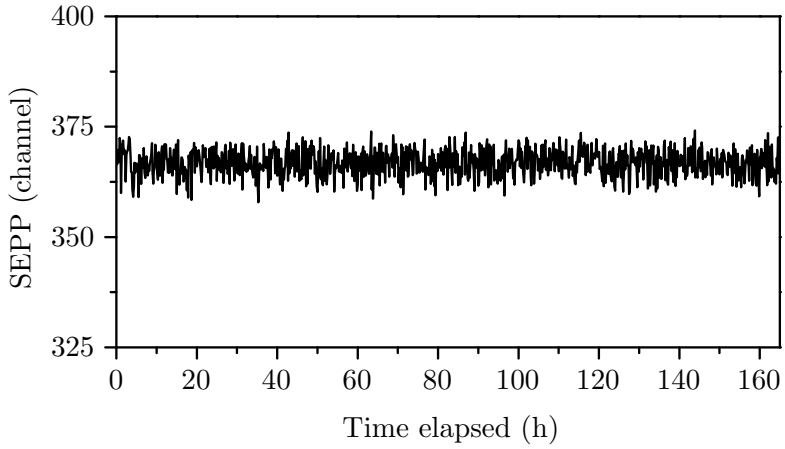

Figure 6.5: **The SEPP during the measurement presented in Fig. 6.4.** The SEPP is determined as described in Section 5.2.3.

sliding valve, and by keeping the PMT supply voltage continuously on. This is evidenced by the stability of the SEPP, as can be seen in Fig. 6.5. The most probable cause of the background increase, is that the temperature of the top of the setup temporarily increased after mounting of the sample chamber. As it is apparent from Fig. 6.4, the count rate increase correlates with the temperature increase. The temperature increase was probably caused by the sample chamber, which was warmed up while it was not mounted onto the setup. This effect is hereinafter referred to as the "opening effect".

The highest value of the background during these measurements was 906.08±0.78 cps, the lowest 894.39±1.00 cps. The difference is attributed to the slight difference between the temperature of the top of the setup (15.1℃ during the measurement of the highest value and 14.9℃ during the measurement of the lowest one). Therefore a value between these two values was considered the normal background of the detector.

6.3 Measurements with the parallel scintillator plate

6.3.1 Measurement procedure and calibration results

The measurement procedure with a water sample of given tritium concentration was the following:

- The detector was operated with a sample (distilled or tritiated water, always 8 ml) until the count rate stabilized (Fig. 6.6).
- The sliding valve was closed, the sample chamber taken off the setup and opened.
- Five samples were taken from the water in the sample chamber, which were measured by means of LSC.

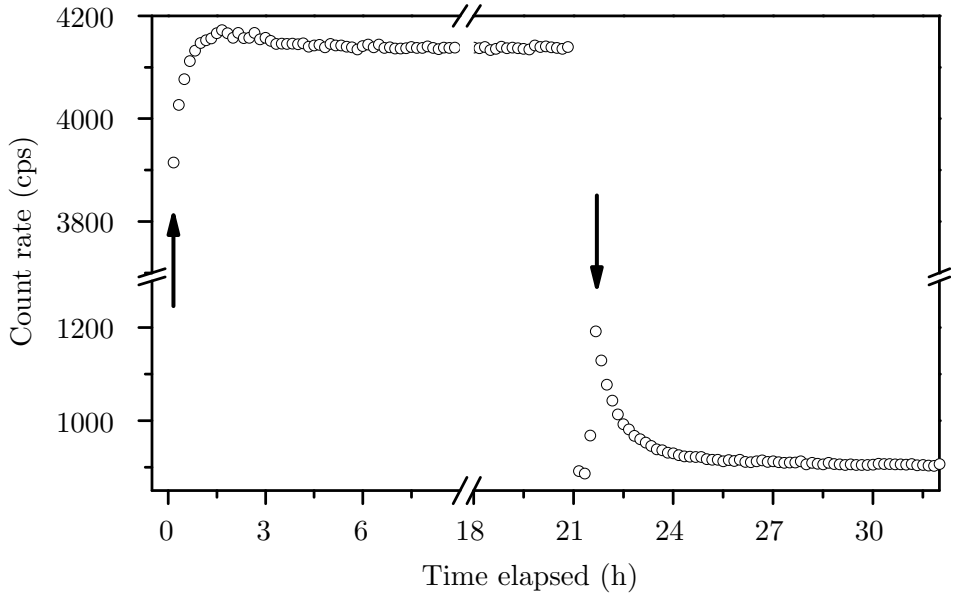

Figure 6.6: **Count rate during a HTO and a background measurement.** The arrows show the times, when the sliding valve was opened. In the beginning of the HTO measurement, there is a distinct overshoot, then the signal stabilizes after about 3 hours. Only the beginning and the end of the HTO measurement is shown.

- The water was taken out, and the sample chamber and the scintillator were flushed with distilled water.
- A new sample was put into the sample chamber, which was then closed and mounted onto the setup.
- The sliding valve was opened.

Five tritiated mixtures were measured one after the other, with distillated water measurements in between two HTO measurements. The list of tritium concentrations of the used water mixtures and the obtained count rates are included in Table 6.2. The count rates belonging to the various concentrations were calculated using the last 10 count rates before exchanging the water.

One interesting observation is that the signal of the detector does not settle immediately after the opening of the sliding valve (see Fig. 6.6). This can be partly the consequence of the "opening effect", but in case of the HTO measurements, the signal first increases, then decreases. This is in contrast with the signal behavior observed in connection with the "opening effect", where the signal first assumes a higher value immediately, then decreases. This phenomenon is further analyzed in Section 6.3.2.

Table 6.2 shows that all the distilled water samples became contaminated after the first tritiated water measurement. The measured concentrations were the same order of

Table 6.2: **HTO concentrations and count rates obtained from the calibration of the improved setup.** Some of the samples were diluted to match the sample activity to the dynamic range of the LSC machine, as it is noted in the remarks.

Measurement code	Activity concentration (c_A, GBq/ℓ)	Sample volume (μl)	Remarks	Count rate (CR, cps)
N-DW 1	$< 10^{-6}$	1000	Under LSC detection limit	894.39±1.00
N-TW 1	3.11 ± 0.05	3		2237.75±1.04
N-DW 2	$(8.80 \pm 0.20) \cdot 10^{-4}$	1000		900.77±0.77
N-TW 2	7.48 ± 0.10	3		4136.93±1.13
N-DW 3	$(1.89 \pm 0.18) \cdot 10^{-3}$	1000		903.28±0.74
N-TW 3	10.2 ± 0.15	3		5371.87±3.95
N-DW 4	$(3.13 \pm 0.12) \cdot 10^{-3}$	100		917.49±0.80
N-TW 4	16.65 ± 0.28	5	Sample diluted: 1:10	8349.71±1.78
N-DW 5	$(5.43 \pm 0.06) \cdot 10^{-3}$	300		923.46±0.59
N-TW 5	27.45 ± 0.31	5	Sample diluted: 1:10	12691.4±2.9
N-DW 6	$(3.04 \pm 0.01) \cdot 10^{-3}$	300		918.36±0.48

magnitude as the ones during the calibration presented in the previous chapter.

The calibration line, resulting from the data in Table 6.2 is presented in Fig. 6.7. The line in the figure is the result of a fitting using X and Y errors, yielding the following equation:

$$CR = (436.5 \pm 4.4) \cdot c_A + (910.2 \pm 0.42) \tag{6.1}$$

This gives a sensitivity value of

$$\eta_{det} = 4.36 \pm 0.03 \cdot 10^{-7} \ \frac{\text{cps}}{\text{Bq}/\ell} \ .$$

The specific sensitivity of the detector is then

$$\epsilon_{det} = 1.88 \pm 0.02 \cdot 10^{-8} \ \frac{\text{cps}}{\text{Bq}/\ell \cdot \text{cm}^2} \ .$$

The measured background count rate did not return to the original value, but showed an increasing tendency. This tendency remains, if the count rate values are corrected using the contamination found in the water, using Eq. 6.1.

The critical limit and detection limit were calculated the same way, as in the previous calibration. Using the value and standard deviation of the intercept of the fitted line one obtains:

$$L_{crit} = 910.57 \text{ cps} \rightarrow c_{A,crit} = 0.00095 \text{ GBq}/\ell,$$

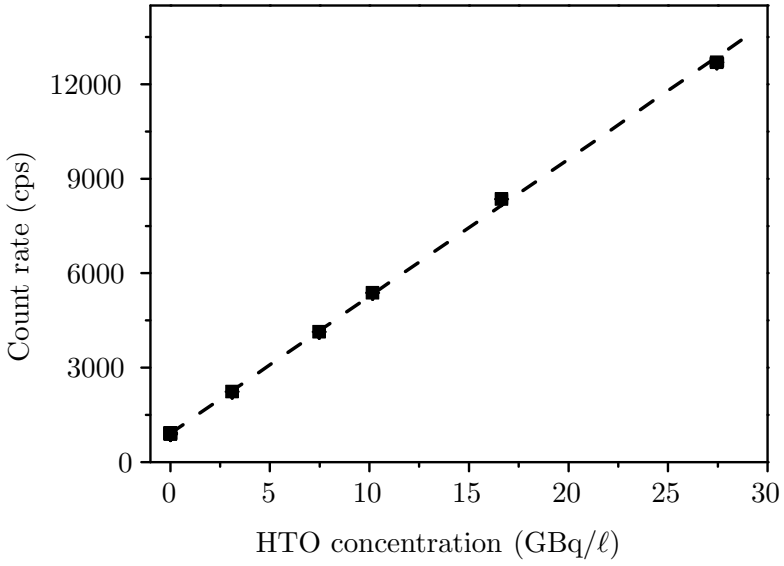

Figure 6.7: **Calibration line of the improved setup.**

and

$$L_{det} = 910.99 \text{ cps} \rightarrow c_{A,det} = 0.00190 \text{ GBq}/\ell.$$

If the highest measured background (corrected to the measured activity by means of the slope of 6.1) and its standard deviation are used, the results are:

$$L_{crit} = 922.06 \text{ cps} \rightarrow c_{A,crit} = 0.0273 \text{ GBq}/\ell,$$

and

$$L_{det} = 923.03 \text{ cps} \rightarrow c_{A,det} = 0.0295 \text{ GBq}/\ell.$$

The N-DW 6 measurement was continued for a week. The count rate of this measurement, after opening the sliding valve is shown in Fig. 6.8. As it is apparent, the background decreased only slowly, reaching 918.36±0.48 cps after one week. The temperature of the top to the setup during this measurements was in the range 14.9 to 15.1℃. After 7 days the distilled water in the sample chamber was exchanged, but the count rate did not change significantly.

The scintillator during these experiments was damaged the same way, as the one in the previous experiments. At the end of the measurement series the contamination in the scintillator was measured using the method described in Section 5.7, and it was found that the scintillator contained 12.62±0.08 Bq tritium.

6.3.2 Analysis of the pulse height spectra

The spectrum of tritiated water was analyzed with a method similar to that in Section 5.4.2. First, in case of the background 80, while in case of the HTO spectrum 69 spectra were summed channel-by-channel, then the counts for 10 minutes were calculated (see

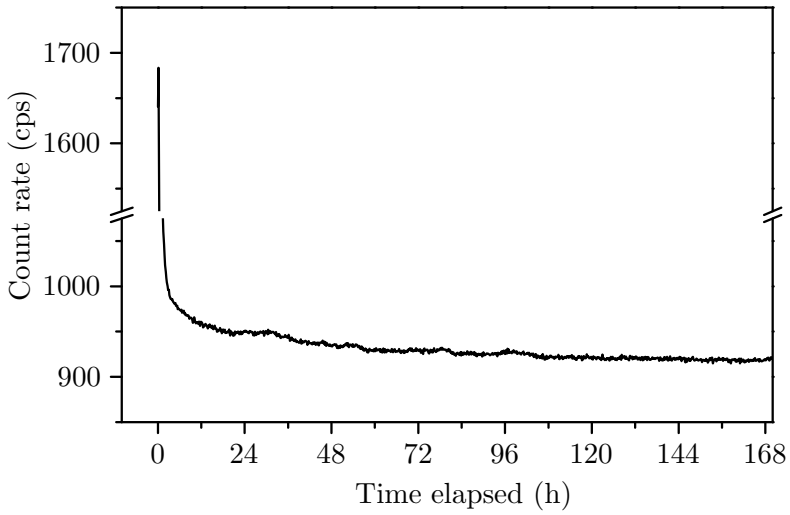

Figure 6.8: **Count rate of the "DW-6" measurement.** The elapsed time starts at the time, when the sliding valve was opened.

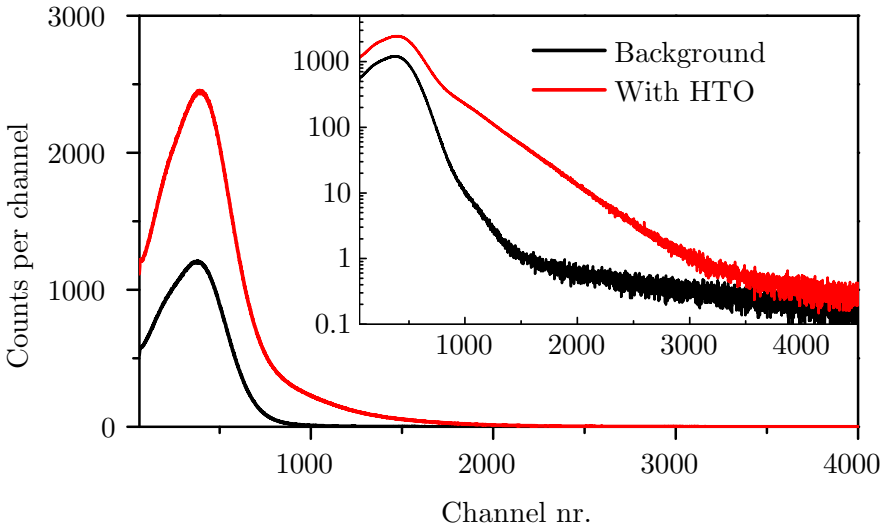

Figure 6.9: **The background and tritiated water spectra of the improved setup.** The counts were summed from 80 and 69 measurements in case of the background and tritiated water measurements, respectively, normalized with the respective livetimes and calculated for 600 s measurement time. The activity concentration of the tritiated water was 3.11 ± 0.05 GBq/ℓ.

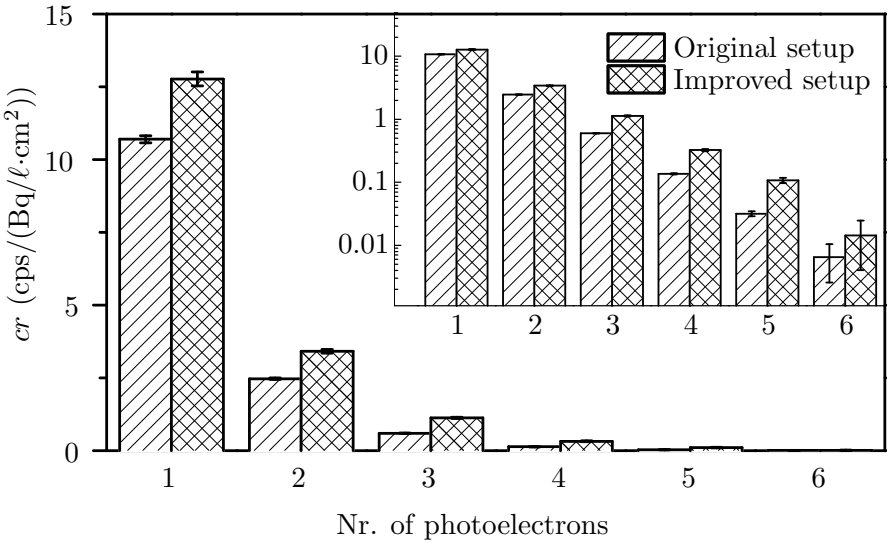

Figure 6.10: **Comparison of the relative spectra of the original and the improved setup.** Both spectra are normalized with the activity concentrations and the surface area of the scintillators.

Fig. 6.9). The spectra in Fig. 6.9 is analogous to the spectra obtained during the previous measurements presented in Section 5.4.2. The SEP dominates the spectrum, and only the DEP and TEP are significant besides.

Equation 5.13 was fitted onto the obtained spectra, yielding the counts of the single- and multiple-electron peaks. Only the spectrum part from channel 350 was used for the fitting, because of the asymmetry of the SEP. The background counts of the SEP, DEP, etc. were subtracted from those of the corresponding counts of the HTO spectrum, yielding the electron number spectrum of the HTO.

The above spectrum was normalized with the HTO concentration and the surface area of the scintillator:

$$cr(n) = \frac{CR(n)}{c_A \cdot F_{sci}} \ , \tag{6.2}$$

where $cr(n)$ means the normalized count rate of the n-electron events, and F_{sci} is the surface area of the scintillator. The resulting normalized spectrum is presented in Fig. 6.10, together with the (also normalized) spectrum obtained in the previous measurement series (Section 5.4.2).

The comparison of the spectra shows that in general, the number of detected events is higher with the improved setup. For further comparison the ratio of the normalized count rates from the same measurements are shown in Fig. 6.11. The figure shows that the number of multiple-electron events has increased, meaning that the spectrum is shifted towards multiple electron events.

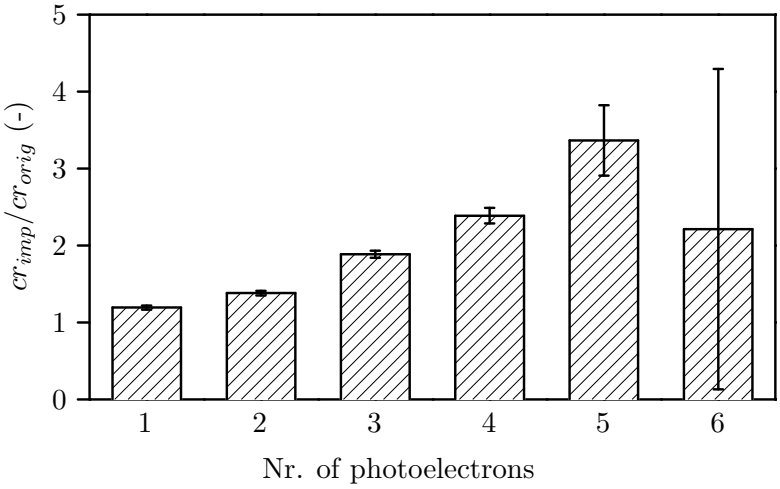

Figure 6.11: **Ratios of the HTO spectra of the original and improved setups.** The high uncertainty of the 6-electron peak ratio results from the already high uncertainties of the 6-electron peaks.

6.3.3 Change of the count rate with time

As it is mentioned in Section 6.3.1, the measured count rate did not change abruptly after changing the HTO concentration and opening the sliding valve, but increased/decreased slightly in case of HTO/background measurements. For further investigation of this phenomenon, the spectra of individual 10-minute measurements were fitted with Eq. 5.13. To characterize the change of the count rate with time, the double-electron peak was used. The reason for this is that the double electron peak is still significant in the spectrum, but the temperature changes due to the "opening effect" do not affect it significantly, as can be seen in Fig. 6.12. The data presented in Fig. 6.12 is obtained from the spectra of the same background measurements as those presented in Section 6.2. The figure here shows the data obtained for the second valve opening. As can be seen in the figure, the maximal count rate change of the DEP is on the order of 4 cps. In case of HTO and later background measurements (for example see Fig. 6.13 and 6.14) the scattering of the data is on the same order, therefore the change due to the "opening effect" is hereafter neglected.

Fig. 6.13 shows the count rate of the DEP during a HTO measurement, beginning at the fist measurement after the opening of the sliding valve. As can be seen, the count rate of the DEP increases gradually after the opening of the valve, not showing any overshoot as the total count rate (see Fig. 6.6). In order to find a characteristic time for this phenomenon, the following function was fitted to the data in Fig. 6.13:

$$CR = CR_{HTO} + K \cdot \exp\left(-t/\tau\right) \ , \tag{6.3}$$

where CR_{HTO} is the count rate to which the measured count rate converges, K is a constant, and τ is the characteristic time of the count rate change. The justification of

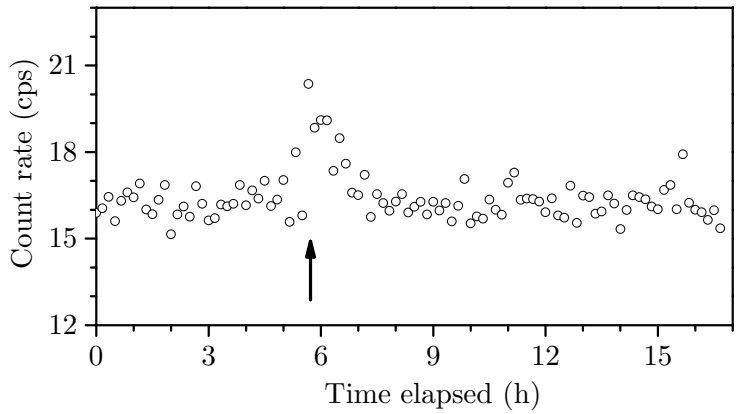

Figure 6.12: **Count rate of the DEP during the first background measurement.** The arrow shows the time of opening the light shutter valve.

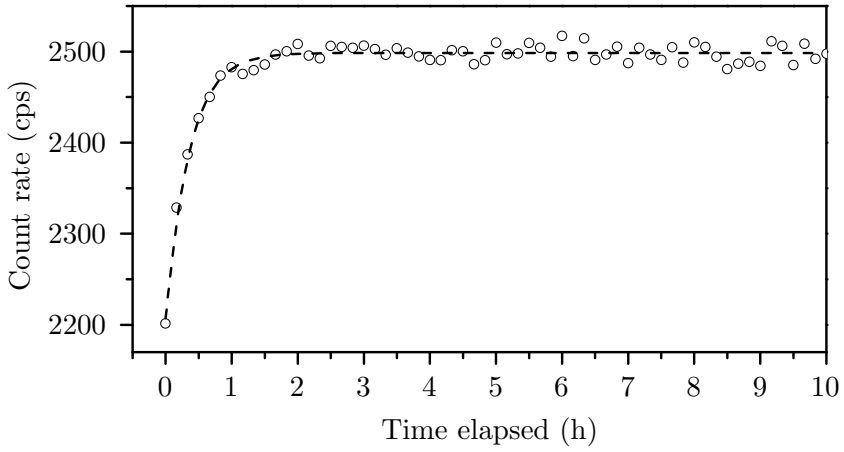

Figure 6.13: **Count rate of the DEP during a tritium measurement.** Tritium concentration: 27.45 ± 0.31 GBq/ℓ. The elapsed time is measured from the beginning of the first measurement after opening the sliding valve. The dashed line shows the fit result with Eq. 6.3.

Table 6.3: **Reaction time and coefficient of the exponential from fitting Eq. 6.3 to the HTO measurement data.**

Measurement code	τ, min	K, cps
N-TW-1	20.1 ± 7.1	26.39 ± 6.18
N-TW-2	19.6 ± 1.6	89.79 ± 4.78
N-TW-3	21.3 ± 2.7	100.2 ± 9.28
N-TW-4	21.9 ± 1.9	246.4 ± 22.3
N-TW-5	21.9 ± 1.3	344.7 ± 13.4
Average	**21.0**	-

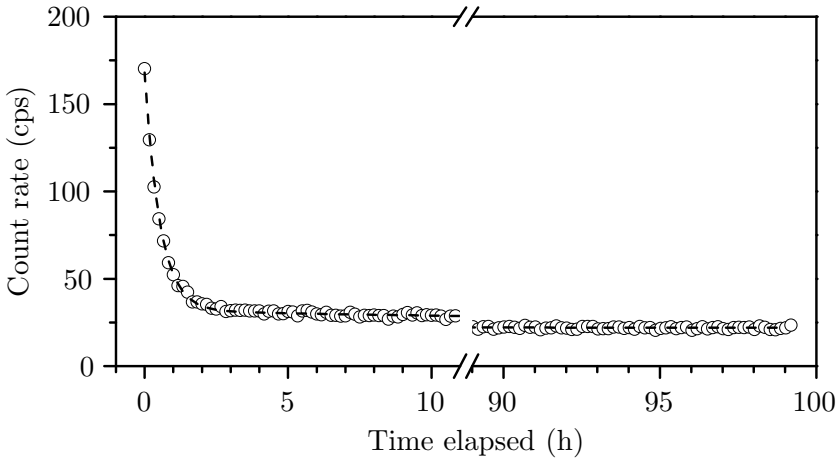

Figure 6.14: **Count rate of the DEP after a HTO measurement.** This measurement followed the one which is shown in Fig. 6.13.

Table 6.4: **Background restoration time constants from fitting Eq. 6.4 to the background measurement data.**

Measurement code	τ_1, min	τ_2, min
N-DW-2	32.2 ± 2.9	255 ± 158
N-DW-3	29.5 ± 1.7	292 ± 191
N-DW-4	27.9 ± 1.8	316 ± 133
N-DW-5	29.3 ± 1.0	352 ± 161
N-DW-6	30.3 ± 0.8	469 ± 136
Average	**29.8**	**337**

the above equation is given in Section 6.3.5.

Equation 6.3 was fitted to the DEP data of all the HTO measurements. The obtained τ values are collected in Table 6.3.

The count rate change during the background measurements showed a different pattern: Besides a relatively quick decrease, another slower decrease was also observable, as can be seen in Fig. 6.14, which shows the data of the DW-6 measurement. The described pattern was observable during all, but the fist (DW-1) measurement.

The data in Fig. 6.14 cannot be described with a single exponential function, but the following equation can be fitted (for justification see section 6.3.5):

$$CR = CR_0 + K_1 \cdot \exp\left(-t/\tau_1\right) + K_2 \cdot \exp\left(-t/\tau_2\right) \ , \tag{6.4}$$

where CR_0 is the background count rate, K_1 and K_2 are constants, and τ_1 and τ_2 are the time constants of the quick and the slow decrease, respectively.

Equation 6.4 was fitted to the data of all, but the first background measurement. The obtained values are summarized in Table 6.4. Analogous processes are observable, if we take the other multiple electron peaks, but the changes are less pronounced.

6.3.4 Modeling the adsorption and desorption of tritiated molecules

To account for the observed gradual count rate change after exchanging the water in the sample chamber, the following simple model is proposed:

1. The count rate of the detector is composed of three parts: The background, the count rate caused by tritium in the water close to the scintillator, and the count rate caused by tritium on the surface of the scintillator:

$$CR = BG + K_{out}c_A + K_{sur}N_{sur} \tag{6.5}$$

   where BG is the background count rate of the PMT, c_A is the tritium concentration in the water, N_{sur} is the number of tritiated molecules on the surface of the scintillator, and K_{out}, K_{sur} are constants.

2. The diffusion in the water is assumed to be fast enough, so that c_A can be approximated to be constant everywhere in the water, during a given measurement.

3. In the beginning of a tritium measurement the scintillator is clean of tritium. This is only an approximation for measurements except the first one, but acceptable, if the coverage of the surface is small compared to the coverage after equilibrium with the tritiated water is reached.

4. The surface coverage with tritiated molecules is negligible compared to a full coverage. Since the concentration in the water is on the ppm level, this assumption is plausible.

5. The change in the number of tritiated molecules on the scintillator (dN_{sur}) is assumed to be the sum of changes due to two processes: adsorption of tritiated molecules onto the scintillator, and desorption of the same molecules.

6. The adsorption probability of one molecule next to the surface is assumed to be constant in time (because of 4, the already adsorbed molecules have negligible effect on the adsorption of others). Therefore the change in the number of molecules on the surface during an infinitesimal time is proportional to the concentration in the water, and the time interval dt:

$$\left.\frac{dN_{sur}}{dt}\right|_{ads} = c_A H \ , \tag{6.6}$$

   where H is a constant.

7. One molecule on the surface is supposed to have a constant probability density in time p_d for desorption, therefore the change in the number of the molecules on the

surface during dt due to desorption is proportional to the number of molecules and the time interval:

$$\left.\frac{dN_{sur}}{dt}\right|_{des} = -p_d N_{sur} \ , \tag{6.7}$$

where the minus sign is because this process decreases the number of molecules.

From points 5, 6, and 7 above it follows that the total change rate of the number of surface molecules is:

$$\frac{dN_{sur}}{dt} = c_A H - p_d N_{sur} \ . \tag{6.8}$$

The solution to the above equation in case of a tritiated water measurement, if $N_{sur}\,(t=0) = 0$ (see point 3 above), is

$$N_{sur} = \frac{c_A H}{p_d}\left(1 - \exp(-p_d t)\right) \ , \tag{6.9}$$

as it can be proven by substituting it into Eq. 6.8. As a consequence of point 2, Eq. 6.9 can be substituted into Eq. 6.5, and we get Eq. 6.3, with

$$CR_{HTO} = BG + K_{out} c_A + K_{sur}\frac{c_A H}{p_d} \ , \tag{6.10}$$

and

$$K = K_{sur}\frac{c_A H}{p_d} \ . \tag{6.11}$$

The time constant in Eq. 6.3 is

$$\tau = \frac{1}{p_d} \ . \tag{6.12}$$

For $t \to \infty$ we get

$$N_{sur} \to \frac{c_A H}{p_d} \ , \tag{6.13}$$

which is equivalent to Henry's law of adsorption: The number of adsorbed molecules is proportional to the concentration of the molecules in the fluid phase.

Equation 6.11 also predicts that the coefficient of the exponential term in 6.3 is directly proportional to the tritium concentration in the water. Fig. 6.15 shows the values of K versus the tritium concentration. Although the data points do not all match the fitted line within errors, the correlation between K and c_A is clearly shown. The differences can be attributed to the imperfectness of the model, which assumes a clean scintillator in the beginning, but this is not strictly true.

If the contaminated scintillator surface is later exposed to distilled water, then $c_A = 0$, $N_{sur}(t=0) = N_0$ (the previously adsorbed molecules), and the solution to Eq. 6.8 is:

$$N_{sur} = N_0 \exp(-p_d t) \ . \tag{6.14}$$

By substituting into Eq. 6.5, we get an equation with an exponential decrease, having the same time constant (p_d), as the increase before. However, this function does not

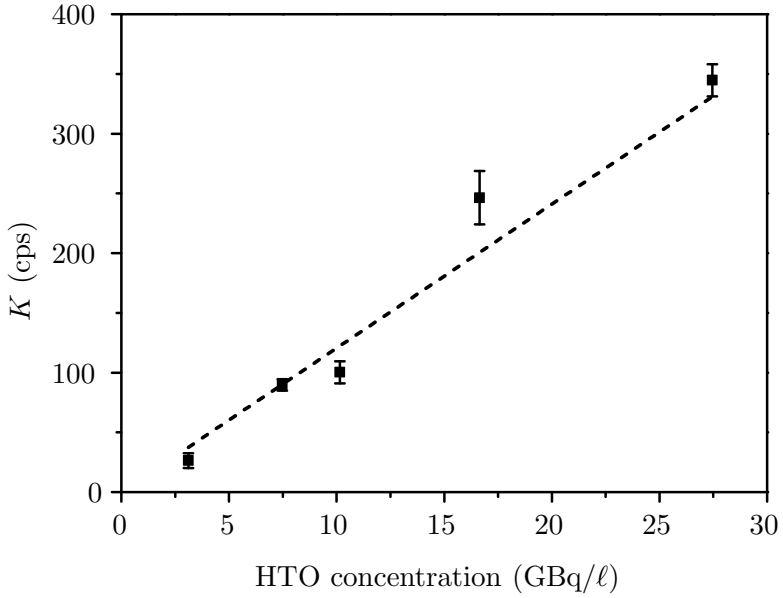

Figure 6.15: **The coefficient of the exponential in Eq. 6.3 versus the tritium concentration in the water.** The dashed line is the result of a fit of the following equation: $K = m \cdot c_A$, yielding $m = 12.05 \pm 0.93\ell$.

match with the experimentally observed one (Eq. 6.4). This discrepancy is probably caused by the simplicity of the model, which does not take into account the possibility of some tritiated molecules being bonded on the surface stronger, than others, due to e.g. influence of radiation (e.g. a HTO molecule breaks up and the tritiated part forms a covalent bond with a scintillator molecule). Another possibility is diffusion of tritiated molecules into the bulk of the scintillator. These molecules then have a much lower probability to be detached from the surface, which means that their detachment process is described by means of an equation analogue to Eq. 6.8, but with a much lower probability, which results in an exponential decrease with a much longer time constant. This can be added to the "quick" exponential (6.14), resulting in Eq. 6.4.

6.3.5 Discussion of the experimental results

The sensitivity of the detector increased by 2.29 times that of the previous setup. The increase in sensitivity partly follows from the increase of scintillator surface, which is 1.7 times higher than the previous one. The remaining improvement is the consequence of the tritiated water spectrum being shifted towards the multiple electron events. Since the used scintillator material was the same, this implies that the light collection of the setup got better, providing the better sensitivity. The better light collection is most probably the consequence of the lack of window between the sample chamber glass and the PMT, because the materials were mostly the same, except the aluminum cup was not present, but this could only increase light absorption.

Table 6.5: **Measurements with perpendicular scintillator.** Some of the samples were diluted to match the sample activity to the dynamic range of the LSC machine, as it is noted in the remarks.

Measurement code	Activity concentration (c_A, GBq/ℓ)	Sample volume (μl)	Remarks	Count rate (cps)
V-DW 1	$(1.60 \pm 0.24) \cdot 10^{-5}$	1000	One sample, stat. uncert.	916.25±0.63
V-TW 1	3.33 ± 0.10	3		1643.31±0.85
V-TW 2	7.89 ± 0.37	3		2633.89±1.01
V-DW 2	$(3.83 \pm 0.14) \cdot 10^{-3}$	100		912.37±0.35
V-TW 3	10.55 ± 0.12	3	Dilution: 1:21	3258.55±1.29
V-TW 4	17.34 ± 0.21	3	Dilution: 1:21	4693.98±1.63
V-TW 5	27.47 ± 0.39	3	Dilution: 1:41	7029.55±2.22
V-DW 3	$(14.9 \pm 0.66) \cdot 10^{-3}$	100		915.67±1.20

The increasing tendency of the background implies a memory effect. Since the background increase is not compensated if we calculate with the contamination of the water, the memory effect includes contamination of the scintillator itself. This contamination leaves the scintillator only partly, if it is in distilled water, which is evidenced by the contamination measured in the scintillator after the calibration measurement series.

The gradual changing of the count rate after sample change in case of a HTO measurement is well described by a simple adsorption-desorption model presented in Section 6.3.4. However, the model is not accurate in describing the gradual decrease of the background signal. As mentioned, the discrepancy is probably due to the neglecting of the possible other processes, which can bond the molecules more strongly to the scintillator. The contamination found in the scintillator after the measurements, in spite of several cleaning attempts with distilled water suggests that such a mechanism indeed exists. This kind of delay in the count rate change after concentration change was also observed by Osborne [18]. This phenomenon limits the usability of such detectors to the observation of such processes, where the characteristic time of the process is much longer than the reaction time of the detector.

6.4 Measurements with a perpendicular scintillator plate

In the course of this measurement series, another scintillator geometry was tested. The previously used sample chamber glass was taken out, and the one presented in Fig. 6.2 b) was inserted, together with a rectangular scintillator plate, perpendicular to the PMT window, with 11.9 cm^2 surface area. The setup, equipped with the new scintillator was tested using the same procedure as during the previous calibration (Section 6.3.1), except that the water volume was 6 ml and the background was only measured 3 times. The data of the measurements is in Table 6.5. The data in Table 6.5 was fitted with a

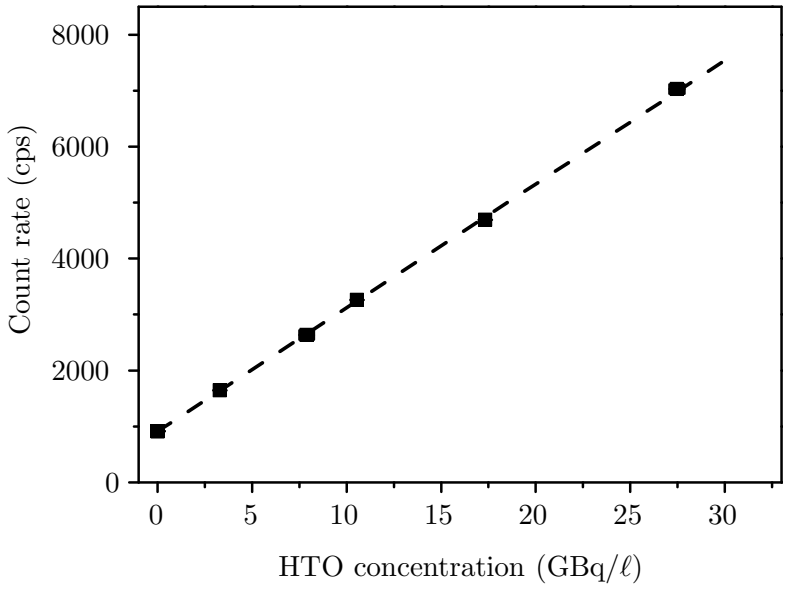

Figure 6.16: **Calibration line of the setup with parallel scintillator.**

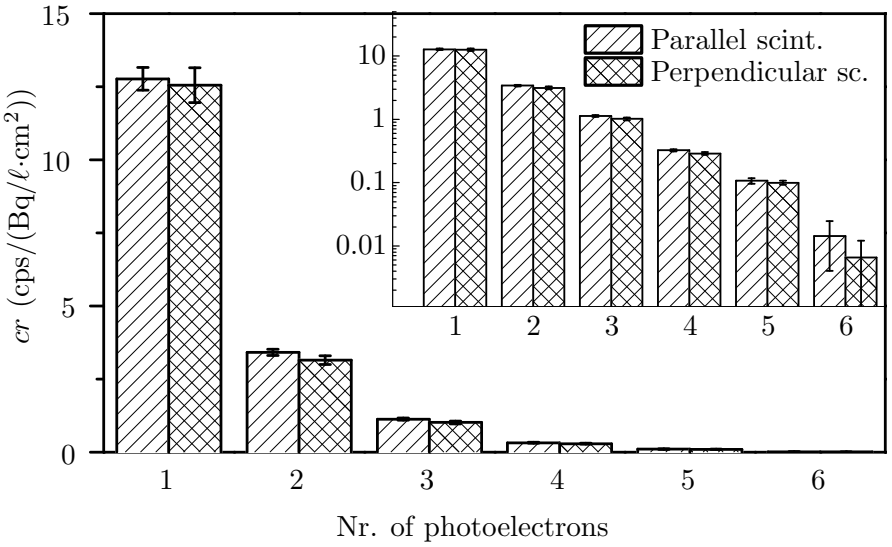

Figure 6.17: **Parallel and perpendicular scintillator HTO spectra.**

line, using X and Y error bars in the fit. The resulting line is plotted in Fig. 6.16. The fitting yielded the following calibration equation:

$$CR = (220.9 \pm 1.5) \cdot c_A + (912.63 \pm 0.30) \tag{6.15}$$

The specific sensitivity of the detector is then

$$\epsilon_{det} = 1.85 \pm 0.02 \cdot 10^{-8} \frac{\text{cps}}{\text{Bq}/\ell \cdot \text{cm}^2} \ , \tag{6.16}$$

which is not significantly different from the one obtained with the parallel scintillator.

The spectrum of the HTO was determined the same way, as for the parallel scintillator in Section 6.3.2. The spectrum was normalized using Eq. 6.2, and it is presented in Fig. 6.17, together with the normalized spectrum of the parallel scintillator. The two spectra are not significantly different, which means that the different geometry did not change the light collection of the setup significantly.

6.5 Summary and conclusions from the results with the improved setup

The experimental setup was modified in order to improve the detection sensitivity and exclude the effects due to the switch-on of the PMT: The sample chamber was redesigned, the new sample chamber glass being exchangeable, but also sealed, rendering an extra window towards the PMT unnecessary. A sliding valve was built in between the sample chamber and the PMT to protect the latter from ambient light, while the sample chamber is opened for sample change. Also, for safer operation, the PMT was exchanged to another type, designed for positive high voltage operation and higher gain.

The improved setup was first tested with a scintillator parallel to the PMT window. The first series of background measurements showed that while the PMT gain did not change after closing and opening the sliding valve (simulating sample change), the temperature of the top of the setup, and the background count rate showed a significant increase after opening the valve. The calibration with tritiated water yielded a sensitivity $4.36 \pm 0.03 \cdot 10^{-7}$ cps/(Bq/ℓ), which is higher, than the recalculated sensitivity ($1.91 \pm 0.03 \cdot 10^{-7}$ cps/(Bq/ℓ) of the previous setup. This is partly the consequence of the bigger scintillator surface, but the spectrum analysis showed that the light collection also improved, which is attributed to the lack of the extra glass window between the sample chamber and the PMT. The sensitivity is still orders of magnitude lower than in previous studies (see Table 3.1), meaning that this difference is more probably due to the lack of light coupling, which is the biggest difference to previous works. The coincidence mode used in those studies (but not in this study) lowers the background of the detector, but does not increase sensitivity.

The measured count rate at the beginning of the measurements shows a gradual increase and gradual decrease during the HTO and background measurements, respectively. The HTO signal increases with a characteristic time of about 21 minutes, the

background decrease has a fast and a slow decreasing component, having characteristic times of 30 minutes and 337 minutes, respectively. This phenomenon is attributed to the adsorption and desorption of tritiated molecules onto and off of the scintillator surface. A simple adsorption-desorption model approximately describes the observed count rate change, however does not account for the slow component of the background decrease. The latter can be attributed to bonding of the already adsorbed molecules, then these have a much lower probability of desorption, yielding the long characteristic time. This phenomenon increases the reaction time of the detector considerably, which limits the usability of plastic scintillator detectors to the monitoring of slow changing processes.

The detector shows a considerable memory effect: The background increases as higher concentration HTO samples are measured, yielding a detection limit on the same order of magnitude as the previous setup. This suggests that the limiting factor concerning detection limit is the memory effect of the detector, and not the sensitivity or the background count rate.

The exchange of the sample chamber glass allowed the testing of a scintillator plate which was perpendicular to the PMT window. The calibration with tritiated water showed that the specific sensitivity of the detector did not change significantly, and the normalized spectrum also did not show any significant improvement. Therefore it seems that the geometry of the scintillator does not play a significant role in the sensitivity.

7 Simulation of the detector behavior

This chapter is dedicated to the Monte Carlo simulations, performed to understand the behavior of the detector, concerning the electron number spectrum of tritiated water. First, the GEANT4 simulation package and the GAMOS framework are briefly introduced, as these were used to perform the first part of the simulations. After this, the geometry, materials and physics of the simulated detector are described. For reasons discussed below, another simulation step was necessary to get the electron number spectrum. This was performed by a custom written *C* program, which is also described here. Finally, the simulated and the experimental spectra are compared, yielding some conclusions regarding the PMT signal and the behavior of the scintillator in tritiated water.

7.1 Brief description of the simulation environment

All technical details discussed here are based on the user documentation of GEANT4 and GAMOS.

The GEANT4 (GEometryANdTracking, [46]) simulation package was developed at CERN, for the purpose of simulating particle detectors. A simulation program, written using this package, consists of three main parts:

- Geometry and material definitions. These contain the data, describing the shapes, sizes and materials of the geometrical objects, which build up the detector. Materials are defined with constants, such as density, atomic/molecular composition, interaction cross sections per atom, mean free path, stopping power for different particles, etc. These are necessary to simulate the behavior of particles within the material. The optical properties of a material are defined as a function of optical photon energy. These are e.g. refractive index, absorption length, etc. Scintillator materials additionally have the following properties: scintillation yield (S_p in photons/MeV), scintillation decay time and emission spectrum.

- Physics definitions. These contain the description of the particles (e.g. electrons, gamma photons, etc.) and physical processes (e.g. bremsstrahlung, scintillation, etc.), which needed to be simulated. The source(s) of the particles to be simulated are defined by means of particle type, geometry and activity.

- User actions during the simulation process. The most important of these are the data saving processes, which save the information about the particles during a simulation run. This way the path of a particle can be followed in detail, e.g. the energy loss during steps.

During a GEANT4 simulation, the particles are simulated one by one. A particle is first initialized, namely its energy, momentum, position, etc. are determined and stored. Then, the movement and interactions of the particle with the detector materials are simulated, during which new particles can be created: e.g. during a scintillation event, an electron can be decelerated in the scintillator, deposits energy in it, and several optical photons are created along its path. These so-called secondary particles are then also simulated one by one, eventually causing new secondary particles, which are then again simulated, until all particles have lost their energy, and the simulation is ended. The path of a particle, together with the initial and final physical parameters of the particle (e.g. energy or position) is called a *track* in GEANT4.

The GEANT4 simulation is a step-based process: The path of a particle is simulated in discrete steps. The word *step* in GEANT4 means a state change, represented by the values of the particle physical parameters at the beginning and at the end of the step. After initialization, based on the attributes of the particle and that of the geometrical object in which it currently is, a step size is determined for each possible physical process which is in the physics definitions. The physical process with the shortest step size is selected, and the particle is moved along the direction of its momentum. The attributes of the particle are changed according to the chosen physical process (e.g. its energy is decreased due to bremsstrahlung). This process is repeated until the energy of the particle decreases to zero.

Developing a simulation in GEANT4 means, that a complex *C* program has to be written. The GAMOS (GEANT4-based Architecture for Medicine Oriented Simulation, [48]) framework makes the development of simulations in GEANT4 easier, by providing an interface to GEANT4. This means, that only two relatively simple text files have to be written, one defining the geometry and materials (.geom file), the other defining the physics and user actions (.in file). No programming is required, because the GAMOS interpreter translates the .geom and .in files into a GEANT4 simulation program.

7.2 Description of the simulation

The simulation was written to simulate the setup used for the measurements in Chapter 5. Consequently, the modeled geometry corresponds to the one in Fig. 4.1.

7.2.1 The chain of processes causing a detected event

The simulated process is schematically illustrated in Fig. 7.1. The GEANT4/GAMOS simulation was written to perform the points in Fig. 7.1, but points 2. and 4. are not modelled accurately due to inherent limitations in GEANT4/GAMOS, as it is detailed below. The simulation process is the following:

1. The energy loss in water is accurately simulated by GEANT4, using the physical properties of water, which are part of the GEANT4 package by default.

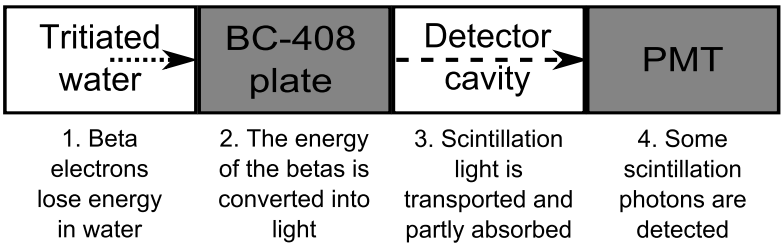

Figure 7.1: **The simulated detection process in the detector.**

2. The Birks quench is not programmable in GAMOS, therefore the number of scintillation photons generated by GEANT4 in one step has a Gaussian distribution[1] with a mean ($\Delta L_{p,lin.}$) directly proportional to the energy lost in the step ($= \Delta E$):

$$\Delta L_{p,lin.} = S_p \cdot \Delta E \ . \tag{7.1}$$

   This equation follows from Eq. 3.12 for one step if $kB = 0$, and the integration is between the two energies of the particle at the beginning and end of the step in which the energy is lost in the scintillator. The corrections due to the Birks quench are detailed in 7.2.3.

3. The behavior of scintillation light is simulated in detail in GEANT4, using the given refractive indices and absorption coefficients.

4. In the GEANT4/GAMOS simulation, the photocathode is modeled by means of a material with the same refractive index as that of the PMT window, but with an absorption coefficient so high, that the probability of absorption of an optical photon in it is practically 100%. The detection of the photons is in reality influenced by the quantum efficiency, which is simulated by means of an additional step in the post processing, see Section 7.2.3.

7.2.2 Geometric and physical model of the detector

By utilizing the rotational symmetry, the model of the detector was constructed using cylinders, cones and tubes, with the application of some simplifications:

- The edges of all objects are sharp, which is not true for the glass cup, but the edges of the cup have small surface compared to the rest of the object.

- The metal housing which surrounds the aluminum cup is not modeled, since only optical photons are expected in this region (the range of the β-electrons is too short to reach it), and therefore makes no difference in the results, but makes the simulation faster.

[1] A Gaussian replaces the Poisson distribution for an average greater, than about 10 [7].

- The rest of the metal housing (the CF flanges) is modeled as one piece, since here only optical photons are expected, therefore only the inner surface of this part follows the real geometry.
- The surface area of the gaskets in the setup is negligible, thus the gaskets are not modeled, i.e. the surfaces are smooth everywhere, where the gaskets would be.
- The relatively complex shape of the window holder flange is modeled with a simple ring. This part also has a small surface compared to the rest of the setup.

The inner part of the detector model is shown in Fig. 7.2. Below the PMT a plate was placed, the optical properties of which are not defined. This is an easy way to provide an absorber body, because the optical photons in GEANT4 are terminated if they arrive into a body with no optical properties. This absorber plate was necessary so that optical photons do not scatter back if they reach the bottom of the PMT somehow, as it might provide false results.

GEANT4 contains the NIST database of materials with properties necessary for the simulation, except optical properties. The sources of optical properties were partly the catalogs of the manufacturing companies ([26], [27]), additionally the following sources were used:

- The refractive index function of borosilicate 3.3 glass was obtained via Ref. [47].
- The refractive index function of fused silica (Spectrosil 2000) was obtained from Ref. [51].
- The complex refractive index of stainless steel was not available, the data of iron was used, since stainless steel contains mostly iron. The data of iron is from Ref. [49].
- The complex refractive index of aluminum is taken from Ref. [50].

All optical surfaces used in the simulation were defined as polished.

The darkening of the aluminum cup (see Fig. 5.24) was modeled with an absorber body (absorbs all optical photons), shaped as a pie slice, inserted into the inner top of the modeled aluminum cup. The pie-slice-shape was chosen, because the detector has rotational symmetry, and the darkening of the aluminum cup is affecting the inner side of the top of the aluminum cup uniformly. The relative area of the grayed spots was estimated by means of the ImageJ (version 1.47v) image processing program, the value is 10%.

The basic electromagnetic physics list was used with the default settings (see also Ref. [53]), which includes the following particles and physical processes:

- gamma photons: photoelectric effect, Compton scattering, gamma conversion, Rayleigh scattering
- electrons: ionization, bremsstrahlung, scattering

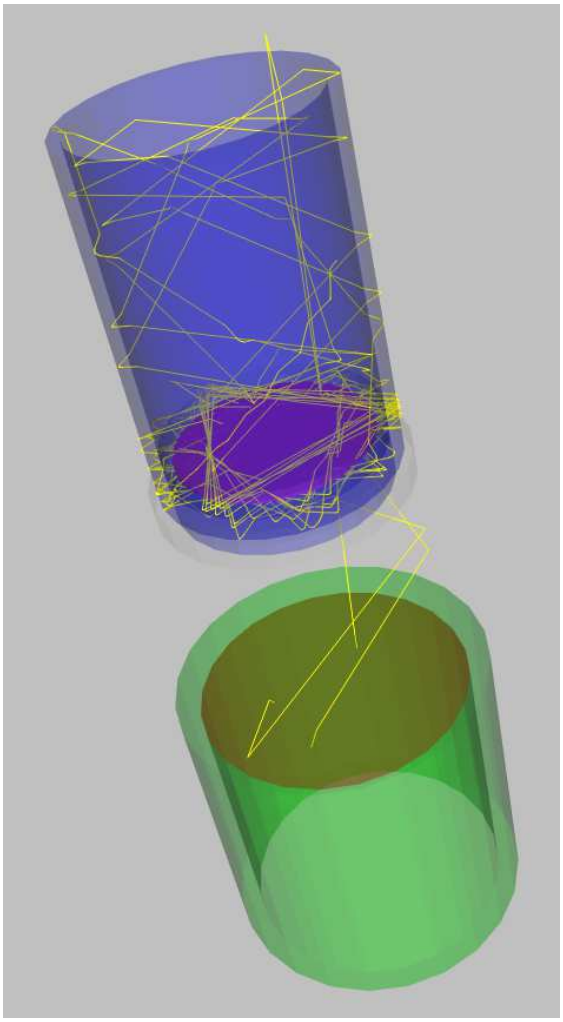

Figure 7.2: **Geometric model of the detector.** The outer metal shell and the aluminum cylinder are not shown. Blue: glass cup and window; purple: scintillator; green: PMT glass envelope; brown: photocathode. The yellow lines show the paths of 10 scintillation photons, tracked until they were absorbed.

- positrons: ionization, bremsstrahlung, scattering
- optical photons: scintillation, optical absorption, Rayleigh scattering, boundary processes (refraction and reflexion)

The tritium source was described to be evenly distributed in the water. The energy probability distribution function of the β-electrons was given as a data-set, containing 18591 energy-probability density pairs. The simulation finds values between these points by linear interpolation.

The particle production cuts[2] were lowered down to 0.1 μm in range, and 100 eV in energy. This was necessary, so that particles very near to the scintillator are not lost, since they can eventually still reach the scintillator.

7.2.3 Post-processing of the simulation data

As mentioned above, GAMOS cannot simulate the Birks quench, therefore an additional simulation step had to be programmed, which also included the effect of the quantum efficiency of the PMT, and an optional scintillation yield reduction (see Section 7.3.2).

The idea behind the post-processing algorithm, is that the "life" of a photon in the detector can be modeled as the series of the following processes:

1. The β-electron deposits energy in the scintillator. A fraction of this energy is stored as excitation energy of the molecules. After Birks, we can call these energy-packets excitons [6]. The average number of excitons produced in a step is (as Eq. 7.1 states):
$$\Delta L_{ex} = S_p \left(E_i - E_f\right) \ , \tag{7.2}$$
where E_i and E_f are the initial and final energies of the β-electron before and after the step.

2. With a certain probability, the exciton energy is transferred into a scintillation photon's energy. To calculate this probability, we first calculate the number of photons which are produced, if the quenching is taken into account. By integrating Eq. 3.11 between E_f and E_i:
$$\Delta L_{ph} = S_p \int_{E_f}^{E_i} \frac{1}{1 + kB\dfrac{dE}{dr}} \, \mathrm{d}E = S_p \left[B(E_i) - B(E_f)\right] \ , \tag{7.3}$$
where $B(E)$ is the function defined by Eq. 3.12. The probability of an exciton becoming a scintillation photon is then:
$$\frac{\Delta L_{ph}}{\Delta L_{ex}} = \frac{B(E_i) - B(E_f)}{E_i - E_f} = \Pr(\text{ex} \to \text{ph}) \tag{7.4}$$

[2] In GEANT4 if a particle is about to be produced by a process, but its range in the material or its energy would be under the production cut, it is not produced, but its energy is deposited in the material. This speeds up the simulation, but a too high cut can cause the loss of low energy particles.

3. The absorption of the photon in the detector cavity (traveling from the scintillator to the PMT) is dependent on its starting point and starting direction. This is modeled in detail by GEANT4.

4. After reaching the photocathode, the photon has a certain probability to produce a photoelectron in the photocathode. This probability is equal to the quantum efficiency:
$$\Pr(\text{ph} \rightarrow \text{phe}) = QE \tag{7.5}$$
This quantum efficiency is calculable from the sensitivity of the PMT (Fig. 4.6) by means of Eq. 3.14.

5. The collection efficiency of a PMT first dynode is around 80% (conservative estimation from [7]). This means, that a photoelectron has an 80% probability to be detected.

The GEANT4/GAMOS simulation models these processes as if: $\Pr(\text{ex} \rightarrow \text{ph}) = \Pr(\text{ph} \rightarrow \text{phe}) = 1$. This was corrected by performing the following procedure for each scintillation photon with a custom-written C program:

- $\Pr(\text{ex} \rightarrow \text{ph})$ and $\Pr(\text{ph} \rightarrow \text{phe})$ are calculated from the data obtained from the simulation, namely E_i and E_f of the step which created the photon, and the energy of the photon E_p, using the photon-energy-dependent quantum efficiency.

- A random number ($0 < RN \leq 1$) is generated from a uniform distribution. The photon is taken into account in the final spectrum if
$$RN \leq \Pr(\text{all}) = \Pr(\text{ex} \rightarrow \text{ph}) \cdot \Pr(\text{ph} \rightarrow \text{phe}) \cdot 0.8 \ , \tag{7.6}$$
where the last term accounts for the collection efficiency. If this condition is not met, the photon is not taken into account in the final spectrum.

The validity of the procedure above can be justified as follows: the listed processes are independent, and the probability that several independent processes all happen, is the product of their individual probabilities [41]. Additionally, the probability of a uniformly distributed random number being $RN \leq \Pr(\text{all})$, is $\Pr(\text{all})$.

In addition, as it is detailed in Section 7.3.2, it was necessary to reduce the photon yield of the scintillator in the simulation. For this, a yield factor Y ($0 < Y \leq 1$) was introduced into Eq. 7.6:
$$RN \leq \Pr(\text{all}) = Y \cdot \Pr(\text{ex} \rightarrow \text{ph}) \cdot \Pr(\text{ph} \rightarrow \text{phe}) \cdot 0.8 \tag{7.7}$$

Y is the ratio of the photon yield in the simulation (S_{sim}) and the yield given in the specification of the scintillator (S_p):
$$Y = \frac{S_{sim}}{S_p} \tag{7.8}$$

The validity of Eq. 7.7 and 7.8 can be argued for as follows: The production of scintillation photons (excluding the quench, because it is accounted for later) is a Poisson process with a probability

$$\Pr(\text{scint}) = \frac{\Delta L_{ph} \cdot \epsilon_{ph}}{E_i - E_f} \tag{7.9}$$

where ϵ_{ph} is the average energy of a scintillation photon. The effect of introducing Y into Eq. 7.6 is that the photon, after its "birth", has to survive another Poisson process with probability Y. In effect this is the same, as the "birth" of the photon in only one Poisson process with probability

$$\Pr(\text{reduced}) = \Pr(\text{scint}) \cdot Y \tag{7.10}$$

which belongs to a scintillation process with a scintillation yield $S_{sim} = S_p \cdot Y$.

7.3 Results of the simulation

7.3.1 Comparison of simulated and measured spectrum of tritiated water

First, the simulation had run with parameters $kB = 9.21 \cdot 10^{-3}$ g/(MeV·cm^2) and $S_{sim} = S_p = 9600$ photons/MeV. The volume of simulated water in the sample chamber was 3 ml. The resulting electron number spectrum together with the experimentally measured one are presented in Fig. 7.3. It is obvious that the two spectra do not match. There are much less single electron events and much more multiple electron events in the simulated spectrum, than in the experimental one. Additionally, the simulated spectrum extends to 14 photoelectrons, which is more than double that of the experimental value. However, the shape of the simulated spectrum is at least similar to the experimentally obtained.

The cause of the discrepancies between the experiment and the simulation could have been the degradation of the scintillator in tritiated water, which is very probable if we take into account the observed cracking of the scintillator surface, discussed in Section 5.7. According to Birks [6], degradation of the scintillator material can cause a decrease in scintillation yield and increase in quench (increase of the kB parameter). In the next section these possibilities are investigated to match the simulation to the experimental results.

7.3.2 Optimization of the simulation parameters

The kB and Y parameters of the simulation were varied in order to find the best fit to the experimentally obtained data. As fit parameter, the reduced chi-square value (χ^2_{red}) was used, which was first calculated using the spectrum points from the one-electron events to the six-electron events. The map of χ^2_{red} values obtained this way is plotted in Fig. 7.4. In an ideal case the χ^2_{red} values should be close to one, meaning a match within experimental errors. However, the lowest obtained χ^2_{red} value was 275.3, not even

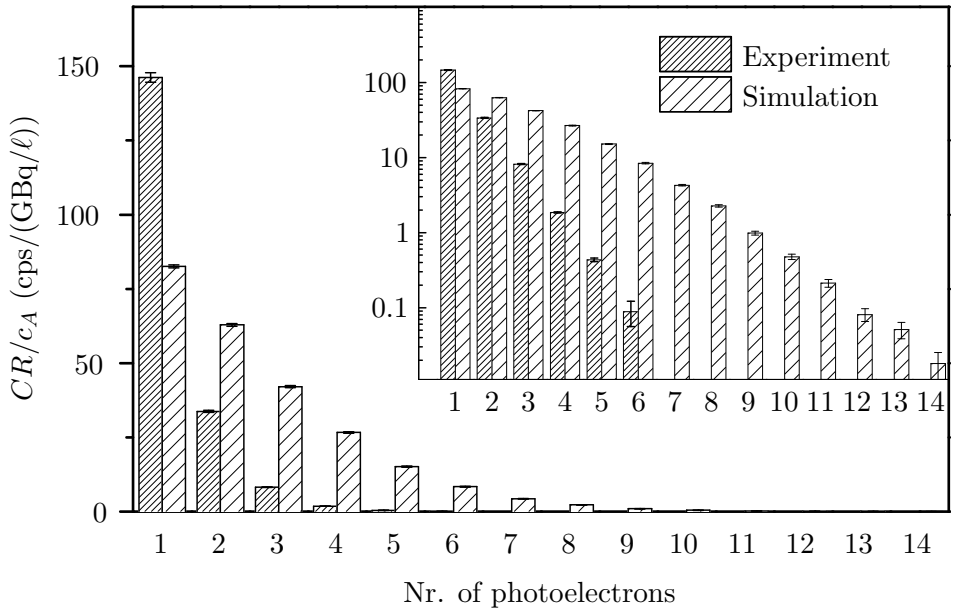

Figure 7.3: **Comparison of the simulation and the experiment.** The main parameters of the simulation: $kB = 9.21 \cdot 10^{-3}$ g/(MeV·cm^2), $S_p =$ 9600 photons/MeV.

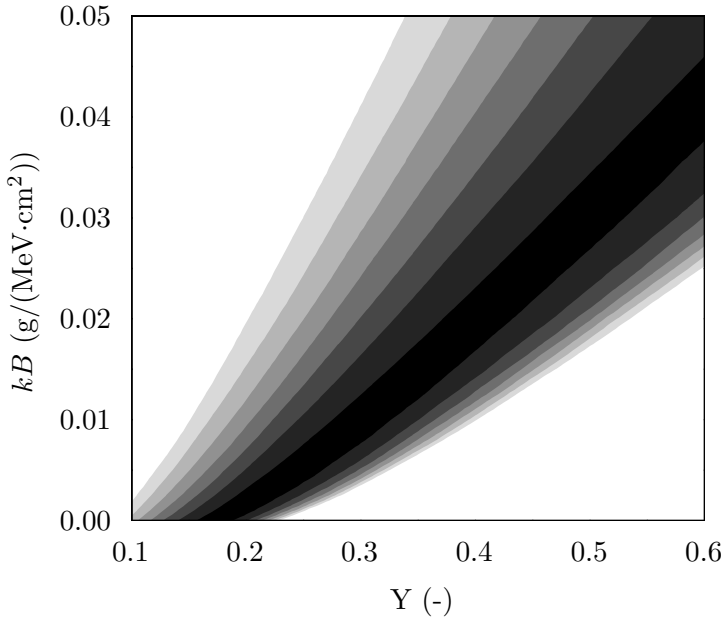

Figure 7.4: **Map of the reduced chi-square values versus the two main parameters of the simulation.** The white areas mark parameter-pairs for which the χ^2_{red} value was over 3500, the black area marks values under 500, while the gray areas differ 500 from each other.

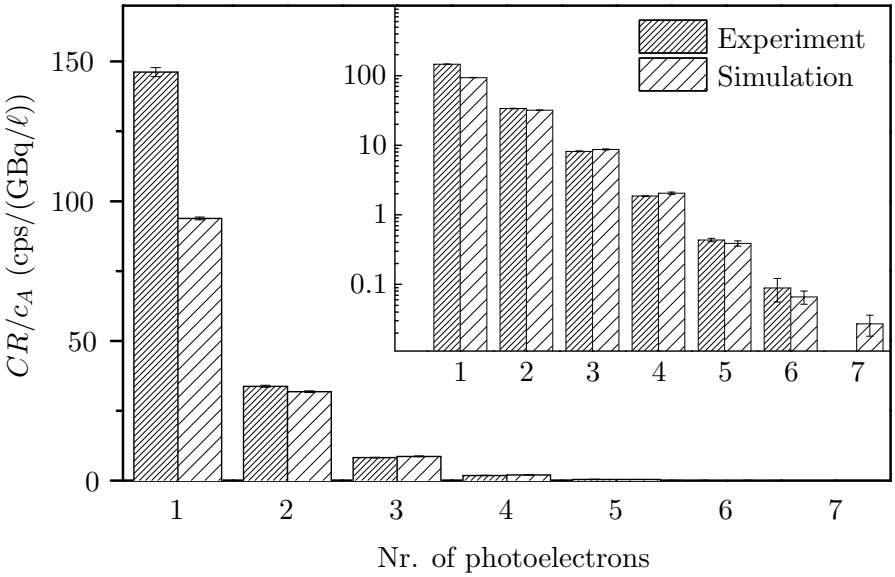

Figure 7.5: **Comparison of the optimized simulated spectrum with the experiment.** The main parameters of the simulation: $kB = 0.0$ g/(MeV·cm^2), $Y = 17.5\%$ ($S_p = 1680$ photons/MeV).

close to one. Interestingly, the kB value associated with this χ^2_{red} value is 0, meaning a perfectly linear scintillator response. The corresponding Y value is 17.5±0.5% (here the uncertainty represents the resolution with which the scan over the Y values was made). The comparison of the optimized simulated spectrum, and the experimental one is presented in Fig. 7.5. From Fig. 7.5 it is clear that the single electron peak is the point most deviating from the experimental data, probably causing most of the deviation of the χ^2_{red} value from one. Indeed, if the χ^2_{red} value is calculated only from the spectrum part above the single electron peak (with the same Y value), the χ^2_{red} value becomes 31.4, which is almost an order of magnitude decrease, meaning that the match between the two spectra is satisfactory above the single electron peak.

The possible cause for the extreme deviation of the single electron peak can be, that the electrons in the photocathode are being constantly excited by scintillation photons, but only part of them leave the photocathode, and becomes detected. If the remaining ones remain in the excited state long enough, they can be ejected from the photocathode by thermionic emission with higher probability, than the not excited ones. Therefore the thermionic emission depends on the amount of scintillation light falling onto the photocathode, causing an excess number of single electron pulses. The proof of this phenomena has to remain the topic of further investigations.

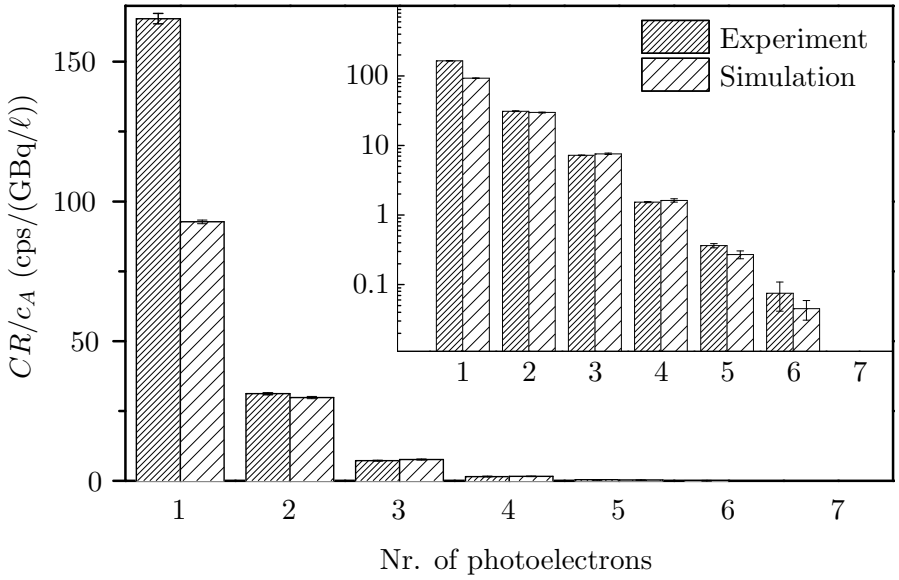

Figure 7.6: **Comparison of simulation and experiment for 9 ml HTO.** The main parameters of the simulation: $kB = 0.0$ g/(MeV·cm^2), $Y = 17.5\%$ ($S_p = 1680$ photons/MeV).

7.3.3 Simulation of the influence of sample volume

To simulate the results from the experiments described in Section 5.5, the simulation was re-parametrized in such a way that it simulated the spectrum of 9 ml tritiated water in the sample chamber. In the post processing the optimized parameters found in the previous section were used ($Y = 17.5\%$ and $kB = 0$). The resulting spectrum, together with the result of the measurement with 9 ml of water is presented in Fig. 7.6. The figure shows qualitatively the same, as Fig. 7.5: the simulated spectrum matches with the experimental one only above the single electron peak. The χ^2_{red} value of this part of the spectrum is 19.2, even better than that of the previous simulation.

The two simulated spectra are compared in Fig. 7.7. The single electron peak decreased in the simulation with increased HTO amount, in strong contrast with the experimental results (see Section 5.5.2). This also suggests that the single electron peak is influenced by some process other than the direct detection of incoming scintillation photons, as mentioned in the previous section. The source of the SEP increase observed in the experiment, according to the simulation cannot be the bremsstrahlung, since this process was included in the simulation, but apparently had no significant effect. The rest of the spectrum decreased, in agreement with the experiment.

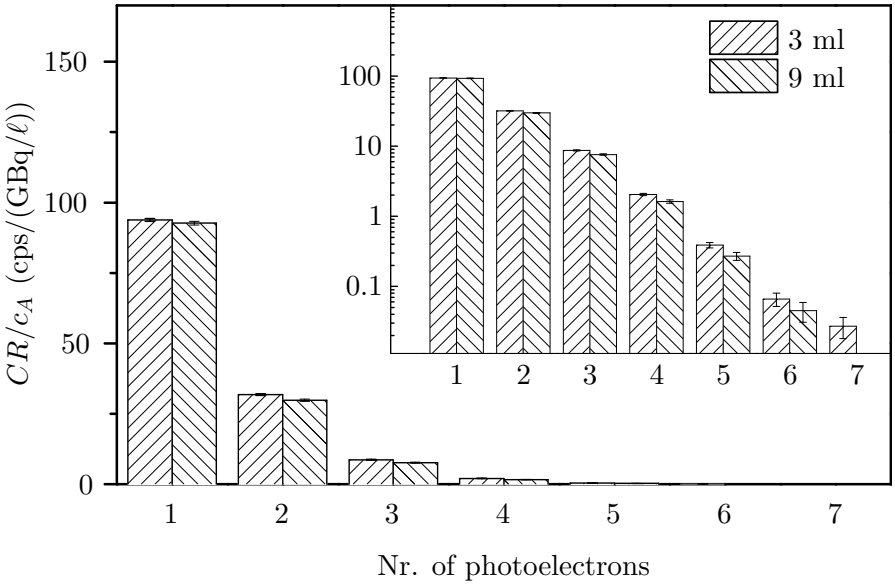

Figure 7.7: **Comparison of the simulations with 3 and 9 ml HTO.** The main parameters of the simulation: $kB = 0.0$ g/(MeV·cm^2), $Y = 17.5\%$ ($S_p = 1680$ photons/MeV).

7.4 Summary and conclusions of the simulation

A simulation program was written using the GEANT4 simulation package and the GAMOS framework to simulate the spectrum obtained with the experimental setup. The geometry of the detector was simplified, but only regarding small details, which do not alter the propagation of scintillation light in the setup significantly. The material parameters were taken either from the description of the components, or from the literature. All parameters were available except the complex refractive index of stainless steel, which is substituted with that of iron.

The simulation was built up in two parts: the GEANT4/GAMOS program simulated the whole process of detection, but had not taken into account the quenching of the scintillator and the quantum efficiency of the PMT. This was corrected by means of a post-processing C program, which also made it possible to simulate a decrease in scintillator yield.

The comparison of the experimental spectrum with the simulation results, obtained with the original scintillator parameters showed great differences. The single electron peak was smaller, and the multiple electron peaks were bigger in the simulated spectrum. The scintillation yield and the quenching parameter were optimized to yield a better fit, using the χ^2_{red} value as an indicator for good fit. The full spectrum could not have been fitted to the experimental data, but the part above the single electron peak gave a satisfactory fit. The optimized scintillation yield was only 17.5% that of the one given by the manufacturer, which suggests that the exposure to tritiated water greatly deteriorated

the performance of the scintillator. The optimized quench parameter turned out to be zero, implying a perfectly linear scintillator response. However, this does not necessarily mean that the scintillator response is linear. The optimized parameters still do not yield a good fit (the χ^2 is well above 1), which indicates that the Birks model of scintillator non-linearity is not adequate in case of damaged scintillator surface.

The analysis of the simulation results for 9 ml water with the optimized parameters showed that again, the simulation matches with the experiment above the single electron peak. Additionally, the simulation showed a decrease in the single electron peak, which contradicts the experimental result, suggesting the existence of a process, which influences the single electron peak besides the detected scintillation photons.

8 Summary and conclusions

The water detritiation system of tritium handling facilities, such as the tritium plants of fusion reactors requires a method to measure the activity of tritiated water inline and real time. This is not possible with the commercially available devices, but previous works have shown that a plastic scintillator-based detector could be used. However, these studies tested the detectors only using tritiated water with tritium concentrations in the kBq/ℓ range, which is well below the range of tritium handling facilities. Hence, in this work a plastic-scintillator based detector was tested in terms of sensitivity and detection limit, with tritiated water samples up to 30 GBq/ℓ. The detector was modified to study various scintillator geometries and to see if it can fulfill requirements specific to the task, from which the most important are a leak tight metal outer housing, simple structure and a detection limit under 1 MBq/ℓ. Since the aim was to test the concept, the detector was not equipped with a flow-chamber.

The test setup was built from a photomultiplier tube (PMT), the PMT electronics (high voltage source and signal analyzer), a quartz window to separate the sample from the PMT, a glass cup for the sample, and a circular disc of plastic scintillator. The housing of the PMT and sample chamber was made of standard industrial flanges and tubes to ensure the necessary leak tightness. As a simplification, aiming easier maintainability, the light coupling between the sample chamber and the PMT was omitted. The background count rate of the detector was stabilized by means of water cooling of the PMT housing.

The first calibration measurement series showed, that the response of the detector is linear. It gave a detection limit of 77 MBq/ℓ, which is too high compared with the specifications. The specific sensitivity (sensitivity per unit scintillator area) of the detector was $1.39 \cdot 10^{-8}$ cps/$\left(\text{Bq}/\ell \cdot \text{cm}^2\right)$, which is orders of magnitude lower, than those of earlier studies (range: 10^{-6} to 10^{-5} cps/$\left(\text{Bq}/\ell \cdot \text{cm}^2\right)$). This sensitivity did not change substantially if the sample amount was varied, but showed a linear relationship with the number of scintillator plates. The analysis of the pulse height spectrum of the PMT showed that almost $^3/_4$ of detected events were single photoelectron events. This was partly attributed to the lack of light coupling in the detector.

Examination of the scintillator after usage showed, that its surface was cracked. This can be caused by the tritiated water, since the plastic scintillator is a very sensitive material, and tritiated water has an increased amount of radicals in it compared to not tritiated water.

The sample chamber of the detector was modified after the above experiments, so that the quartz window became unnecessary. This improved the sensitivity, it became $1.87 \cdot 10^{-8}$ cps/$\left(\text{Bq}/\ell \cdot \text{cm}^2\right)$, the detection limit was also lowered to 29.5 MBq/ℓ. Another scintillator configuration was also tested, in which the scintillator was perpendicular to

the PMT window, but the sensitivity did not change significantly. The spectrum analysis showed, that in the pulse height spectrum of the improved setup more multiple electron events were detected, than in the original setup with a similar scintillator geometry. This proved that the light collection of the setup improved, and this improvement caused the increased sensitivity.

In both detector configurations a considerable memory effect was detected, which increases the detection limit. This memory effect includes the contamination of the scintillator itself, which remains even if the scintillator stays in distilled water for several days. The contamination of the scintillator can be connected to the adsorption/desorption of the tritiated molecules on the scintillator surface. These processes are not instantaneous, and can be approximately described by means of a simple time-dependent adsorption/desorption model. The time constant of the adsorption/desorption is 21 min and 30 min, respectively, as obtained from the analysis of the time-dependent detector signal. The desorption has a "slow" component, with a time constant of several hours, but this contributes only some percent to the overall signal change. In any case, this phenomenon limits the usability of the detector to processes where the concentration changes have a time constant much larger than 30 minutes.

The detection process of the detector was simulated to understand and analyze the experimental results. Using the manufacturer-given coefficients of the scintillator, the simulated spectrum was significantly different from the experimental one. After optimizing the parameters, the two spectra were much closer to each other, yielding a satisfactory agreement for multiple photoelectron events. The best fit was obtained with a scintillator light yield 17.5±0.5% that of the one given by the manufacturer. This dramatic decrease in scintillator yield can be the consequence of the above mentioned damage of the scintillator. Since the agreement of simulation and experiment is not within errors, it is suggested, that the Birks model of scintillation is not exact in case of a surface-damaged scintillator.

In conclusion, a simple structured, scintillator-based tritium detector for tritiated water is feasible. However, the absence of light coupling and the damage of the plastic scintillator by tritiated water deteriorates its sensitivity and detection limit. The performance of the detector cannot be significantly improved by simply changing the geometry of the scintillator, but the surface must be increased, or the light coupling improved. The observed damage of the scintillator material raises the question of signal stability on the long term, in case the damage can worsen with exposure time. Therefore, it is suggested that such a detector is not built using a plastic, but for example a glass scintillator, with a sufficient scintillation yield and shortest possible decay time, e.g. an LSO scintillator. However, a plastic scintillator might be used if it shows long-term stability, i.e. the scintillator material does not change after the initial surface damage. In any case, a scintillator detector, if the scintillator comes in direct contact with the water, detects the tritium in the water directly. Therefore, it can theoretically provide the best detection limit for tritium in water in contrast to other radiation detectors, which use indirect means for measurement.

Acknowledgment

Here I would like to thank for the many people who helped me a lot during the work:

- First and foremost I would like to thank Beate Bornschein, the leader of TLK, and Guido Drexlin, professor of the Nuclear Physics Institute of KIT for the PhD opportunity and the useful discussions.
- I am thankful to Robert Michling and Stefan Welte from TLK for the useful discussions, and their indispensable advices and help in planning and building of the experimental setup and performing the experiments.
- András Bükki-Deme helped me a lot with writing a data extraction system in LabView, we discussed a lot of topics, and he also gave me a lot of encouragement, for which I am truly grateful.
- I want to thank Sebastian Schüler for his work and his ideas during the commissioning of the setup and the first experiments.
- I especially thank Joachim Wolf and Klaus Eitel for the useful discussions about PMT-s, scintillators, and detectors in general.
- Without the help of Bertram Kuntz and the staff at the KIT Main Workshop, also Dieter Adami and many other colleagues from TLK, it would not have been possible to solve the technical problems I encountered.
- My work would not have been so safe without the precise and reliable work of the KIT Radiation Protection Department.
- I am grateful to Rodrigo Antunes, Olga Borisevich, Aleksandra Wagner, Frank Rehlinghaus, Norbert Kernert and all the other colleagues at TLK for the cheerful work atmosphere.
- I would like to thank Magnus Schlösser and Tim James for their help in reading and correcting the manuscript of this thesis.
- Last but not least, I would like to express my gratitude to Éva Katona, who inspired me to start a PhD work in the first place.

Bibliography

[1] *ITER website* `http://www.iter.org` Last visited: 28.07.2014.

[2] E. M. Burbridge et al.: *Synthesis of elements in stars.* Reviews of Modern Phys. 29/4 (1957).

[3] A. Fiege: *Tritium.* Kernforschungszentrum Karlsruhe, 1992.

[4] L. Dörr et al.: *The closed tritium cycle of the Tritium Laboratory Karlsruhe.* Fus. Sci. and Tech. 48 (2005) pp. 262-267.

[5] G. F. Knoll: *Radiation detection and measurement.* John Wiley and Sons, Inc., 4th Edition, 2010.

[6] J. B. Birks: *The theory and practice of scintillation counting.* Pergamon Press, Oxford, (1964).

[7] *Photomultiplier tubes; Principles and applications.* Photonis, Brive, France (2002).

[8] *Primer on tritium safe handling practices.* U.S. Department of Energy FSC-6910, Washington, USA (1994).

[9] C. G. Alecu et al.: *Reachable accuracy and precision for tritium measurements by calorimetry at TLK.* Fusion Sci. and Tech. 60 (2011) pp. 937-940.

[10] A. Bükki-Deme et al.: *First results with the upgraded TLK calorimeter IGC-V0.5.* Article in press, available online. (10.1016/j.fusengdes.2013.05.066)

[11] M. Matsuyama et al.: *New technique for non-destructive measurements of tritium in future fusion reactors.* Nucl. Fusion 47 (2007) pp. 464–468. (doi:10.1088/0029-5515/47/7/S09)

[12] M. Matsuyama: *Development of a new detection system for monitoring high-level tritiated water.* Fusion Eng. and Des. 83 (2008) pp. 1438-1441. (doi:10.1016/j.fusengdes.2008.05.023)

[13] S. Niemes: *Messung des Bremsstrahlungsspektrums von tritiiertem Wasser mit einem Siliziumdriftdetektor am Tritiumlabor Karlsruhe.* (Measurement of the bremsstrahlung-spectrum of tritiated water with a silicon drift detector at the Tritium Laboratory Karlsruhe.) Diploma thesis, Karlsruhe Institute of Technology, Institute of Technical Physics, Tritium Laboratory Karlsruhe, 2013.

[14] *BC-400, BC-404, BC-408, BC-412, BC-416 Premium Plastic Scintillators.* Brochure of the Saint-Gobain Ceramics & Plastics, Inc., (2008).

[15] *Organic scintillation materials* Brochure of the Saint-Gobain Ceramics & Plastics, Inc., (2011).

[16] M. Muramatsu, A Koyano and N. Tokunaga: *A scintillation probe for continuous monitoring of tritiated water.* Nuclear Inst. and Meth. 54 (1967) pp. 325-326.

[17] A. A. Moghissi et al.: *A tritium monitor based on scintillation.* Nuclear Inst. and Meth. 68 (1969) p. 159.

[18] R. V. Osborne: *Detector for tritium in water.* Nuclear Inst. and Meth. 77 (1969) pp. 170-172.

[19] A. N. Singh, M. Ratnakaran and K. G. Vohra: *An on-line tritium-in-water monitor.* Nuclear Inst. and Meth. in Phys. Research A236 (1985) pp. 159-164.

[20] K. J. Hofstetter and H. T. Wilson: *Aqueous effluent tritium monitor development.* Proceedings of the 4. topical meeting on tritium technology in fission, fusion, and isotopic applications, Albuquerque, New Mexico (United States), 30th Sept. - 4th Oct. 1991.

[21] C.H. Skinner et al.: *Tritium experience in large tokamaks: Application to ITER* Report on the IEA Workshop held at Princeton, New Jersey, USA, 16–18 March 1998.

[22] R. Michling et al.: *Modification, enhancement and operation of a water detritiation facility at the Tritium Laboratory Karlsruhe* Fus. Eng. and Des., 84 (2009) pp. 338-343.

[23] R. Michling (responsible person for TRENTA at TLK until 2013), personal communication.

[24] *Technische Liefer- und Abnahmebedingungen für Anlagen zur Prozessierung von HTO (z.B. TRENTA)* $< 5 \cdot 10^{12}$ *Bq/l (TLA-Nr. 08).* (Technical delivery and acceptance requirements for devices processing HTO (e.g. TRENTA) $< 5 \cdot 10^{12}$ Bq/l) Regulatory document of the Tritium Laboratory Karlsruhe, 7th edition, 2012.

[25] *VACOM Product Catalog.* VACOM GmbH. From: `http://www.vacom.de/en/downloads/vacom-product-catalogue`, last visited: 18.09.2013.

[26] *Spectrosil 2000.* Brochure of the Heraeus Holding GmbH. From: `http://heraeus-quarzglas.com/media/webmedia_local/downloads/broschren_mo/Spectrosil_syntheticfusedsilica.pdf`, last visited: 18.09.2013.

[27] *Tubing, Capillary and Rod of Borosilicate Glass 3.3* Brochure of the Schott AG. From: `http://www.schott.com/tubing/english/download/schott-tubing_brochure_duran_english.pdf`, last visited: 23.09.2013.

[28] *Model 4006 Minibin and Power Supply.* Advanced Measurement Technology, Inc. (2002).

[29] *Model 556 High Voltage Power Supply Operating and Service Manual.* Advanced Measurement Technology, Inc. (2009).

[30] *Photomultiplier XP2262* Technical information sheet. Photonis, Brive, France (2006).

[31] *Model 113 Scintillation Preamplifier Operating and Service Manual.* Advanced Measurement Technology, Inc. (2009).

[32] *Model 575A Amplifier Operating and Service Manual.* Advanced Measurement Technology, Inc. (2002).

[33] *Easy-MCA-8k Hardware User's Manual.* Advanced Measurement Technology, Inc. (2009).

[34] *Evaluation of measurement data — Guide to the expression of uncertainty in measurement.* Joint Committee for Guides in Metrology, (2008).

[35] Sebastian Schüler: *Design, construction and characterization of a detector solid scintillator combination for determination of tritium in water.* Diploma thesis (in German), Karlsruhe Institute of Technology (2012).

[36] *"Oasis Three"* Operating manual (2011).

[37] *PID controller.* Wikipedia, `http://en.wikipedia.org/wiki/PID_controller`

[38] *QuantaSmart™For The TriCarb®Liquid Scintillation Analyzer* Software Reference Manual, Perkin Elmer, Inc. (2004).

[39] S. Heinze et al.: *Self-radiolysis of tritiated water: Experimental study and simulation.* Fus. Sci. and Tech. 48 (2005) pp. 673-679.

[40] M. Oyaidzu et al.: *Effects of tritiated water on corrosion behavior of SUS304* Fus. Sci. and Tech. 60 (2011) pp. 1515-1518.

[41] R. V. Hogg, J. W. McKean and A. T. Craig: *Introduction to mathematical statistics.* (6th ed.) Upper Saddle River, New Jersey: Prentice Hall. (2004). ISBN 978-0-13-008507-8. MR 467974

[42] *ESTAR database* `http://physics.nist.gov/PhysRefData/Star/Text/ESTAR.html` Last visited: 25.11.2013.

[43] J. C. Ashley: *Stopping power of liquid water for low-energy electrons.* Radiation Research 89 No. 1 (1982) pp. 25-31. `http://www.jstor.org/stable/3575681`

[44] M. Hirschberg et al.: *Precise measurement of Birks kB parameter in plastic scintillators* Transactions on Nucl. Sci. 39 No. 4 (1992).

[45] *51 mm (2") photomultiplier; 9813B series data sheet* ET Enterprises Ltd, 2012.

[46] S. Agostinelli et al.: *GEANT4—a simulation toolkit.* Nuclear Instruments and Methods in Physics Research, Vol. A 506 (2003) pp. 250–303. (doi:10.1016/S0168-9002(03)01368-8)

[47] E-mail communication with Hans-Joachim Fiedler from the Schott AG., Germany.

[48] P. Arce et al.: *GAMOS: A framework to do GEANT4 simulations in different physics fields with an user-friendly interface.* Nuclear Instruments and Methods in Physics Research, Vol. A 735 (2014) pp. 304–313. (doi:10.1016/j.nima.2013.09.036)

[49] E.D. Palik: *Handbook of optical constants of solids II.* Academic Press, Inc. 1991.

[50] A. D. Rakić: *Algorithm for the determination of intrinsic optical constants of metal films: application to aluminum.* Appl. Opt. 34, (1995) 4755-4767. (doi:10.1364/AO.34.004755)

[51] I. H. Malitson: *Interspecimen Comparison of the Refractive Index of Fused Silica* J. Opt. Soc. Am. 55, (1965) 1205-1208. (doi:10.1364/JOSA.55.001205)

[52] *ImageJ Webpage.* `http://imagej.nih.gov/ij/`

[53] *GAMOS 5.0.0 User's Guide.* GAMOS Collaboration 2013.